University of Genoa

Doctoral School

Sciences and Technologies of Chemistry and Materials

Doctoral Course

Materials Sciences and Technologies

XXXVIII cycle

Mechanical Characterization of Biomaterials

Candidate: Andrea Lagomarsino

Supervisors:
Prof. Claudio Canale
Prof. Ornella Cavalleri

Academic Year 2025–2026

“Not in my name”

Abstract

Mechanobiology is an interdisciplinary field that investigates how living cells and tissues sense, transduce, and respond to mechanical forces and physical cues from their environment, and how these signals regulate biological processes.

The increasing recognition of the role of physical forces in shaping cellular responses has challenged the classical biochemical paradigm of cell signaling, which describes cellular behavior as the result of ligand–receptor interactions and downstream molecular cascades. It is now evident that mechanical forces are integral components of these pathways, leading to the so-called *mechanochemical paradigm*, in which cells integrate chemical and mechanical cues to regulate their function.

Within this framework, this thesis applies different biophysical approaches to characterize the mechanical behavior of biological samples, with a particular focus on Atomic Force Microscopy (AFM). AFM was not only used as a measurement tool but also explored as a versatile platform for methodological development, enabling the design of new experimental strategies and correlative approaches with complementary techniques.

The common aim of the projects presented in this thesis is to explore new perspectives in the investigation of neurodegenerative diseases. AFM-based Force Clamp Spectroscopy was employed to study the mechanical destabilization induced by the interaction of α-synuclein oligomers, related to Parkinson's disease, with a biomimetic cytoplasmic membrane model.

To investigate cellular mechanotransduction -specifically Piezo1 channel- activity in the presence of pathological oligomers associated with Parkinson's and Alzheimer's diseases, a correlative AFM-epifluorescence microscopy setup was developed, allowing calcium fluxes driven by Piezo1 activation to be monitored under pathological conditions.

In addition, AFM was used as a rheological tool and combined with Brillouin spectroscopy to investigate altered mechanical pathways in laminopathies, a group of rare neurodegenerative diseases.

Finally, AFM force spectroscopy was applied to mechanically characterize different nanocarrier systems for drug delivery, correlating their mechanical properties with their cellular internalization and homing efficiency.

Contents

1

Neurodegenerative Diseases

1.1 Introduction

Neurodegenerative disorders (NDs) are chronic conditions that progressively damage and destroy parts of the nervous system, usually leading to death. They are characterized by their pathogenesis and by specific symptoms that depend on the location of neuronal loss in the brain. Although several drugs are currently approved for managing neurodegenerative disorders, most of them only alleviate the associated symptoms.

Neurodegeneration is associated with dysfunction of the synapse and neural network, as well as with the deposition of physiochemically altered protein variants in the brain [1]. The most common NDs include Alzheimer's disease and Parkinson's disease, both related to the accumulation of misfolded protein material in the extracellular environment of neurons.

Another, rarer category of NDs involves pathologies associated with genetic dysregulation, which induces over- or under-expression of a gene, altering normal cell metabolism. In this Thesis, we will focus in particular on a disorder of the laminopathies group called Autosomal Dominant Leukodystrophy (ADLD), related to the overexpression of the *LMNB1* gene and the consequent overproduction of Lamin B1 [2].

New insights and experimental tools derived from biophysics and material science can help investigate unexplored aspects of this topic, improving our understanding and enabling the identification of new biomarkers and diagnostic methods.

1.2 Protein Misfolding Diseases

Proteins represent a fundamental class of biomolecules, distinguished by their remarkable abundance (approximately 100,000 different species in the human proteome) and their central role in regulating virtually all biochemical processes within the cell. The defining feature of a protein is its amino acid sequence, organized in a linear polypeptide chain. Although more than 500 amino acids have been identified, only 20 are proteinogenic. The limited size of this "alphabet" is compensated by the considerable length of protein chains, which typically consist of about 300 amino acid residues. The primary sequence dictates the emergence of a highly complex three-dimensional conformation, whose precise folding constitutes a striking example of evolutionary optimization.

Proper protein folding is ensured by several factors including catalysts, chaperones, and proteolytic systems, which collectively facilitate physiological folding/unfolding events and mediate the recovery or degradation of misfolded conformers. Failure of these control mechanisms leads to the accumulation of aberrant protein species or to cellular dysfunctions, ultimately resulting in pathological conditions.

Experimental results show that aggregation occurs when misfolded proteins expose hydrophobic residues or segments of the main chain that are buried in the native state and are generally aggregation-prone [3,4].

Protein misfolding diseases are a class of pathologies characterized by the the misfolding, aggregation, and deposition of proteins into insoluble fibrillar assemblies, either intra- or extracellularly. To date, more than 20 human amyloid-related disorders have been identified [5,6]. These proteins exhibit an intrinsic propensity to misfold due to the presence of local minima in the energy landscape model that are only slightly less favourable than the native state. This predisposition can be enhanced under certain conditions, such as aging or high serum concentration, leading to disease onset. Alternatively, amyloid precursors may arise from point mutations in the amino acid sequence or from proteolytic cleavage of non-amyloidogenic proteins.

Among the large class of protein misfolding diseases, the pathologies characterized by extracellular accumulation are also called amyloidosis. Two main types of amyloidosis can be distinguished: localized and systemic. The former affects only a limited area of the body, whereas the latter involves tissues throughout the body. The most impactful protein misfolding diseases are neurodegenerative diseases affecting the central nervous system, such as Alzheimer's and Parkinson's disease [6].

1.3 The Structure of Amyloid Aggregates

Amyloids are characterized by a fibrillar morphology, typically several micrometers in length and 6–12 nm in diameter. They share a highly ordered structure called **cross-β**, in which β-strands run perpendicularly to the fibril axis and β-sheets stack parallel to it [7].

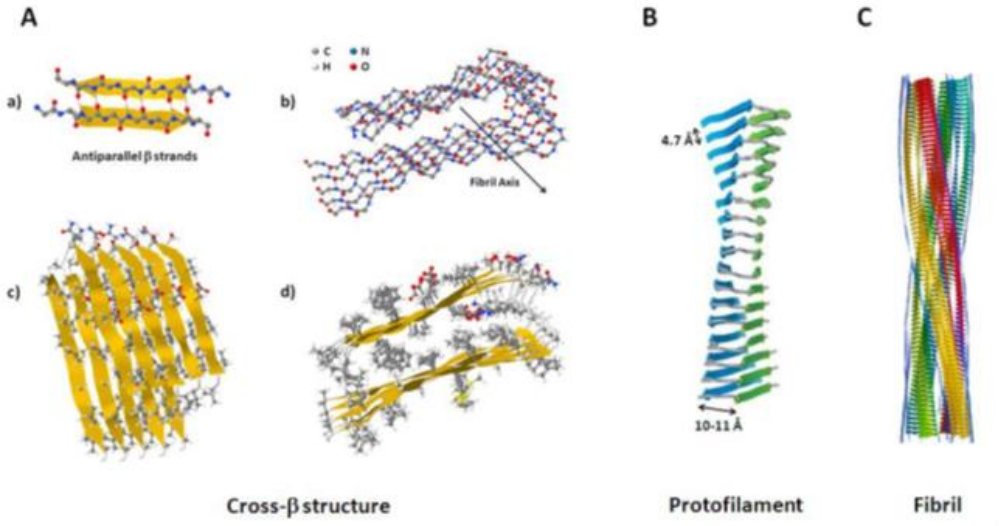

Figure 1-1: A: Exemplifying cross- structure of amyloid filaments. a) -strands can be represented by ribbons ending with an arrow, pointing towards the C-terminus; hydrogen bonds form between consecutive strands. The example in b), c) and d) refers to A(1-42) fibril (PDB ID: 2BEG). In b) only the main chains are shown. c) and d) are different orientation of the structure in b), showing the side chains. B: Example of amyloid protofilament. C: Insulin quadruplet fibril structure obtained by cryo-electron microscopy with a cross-β structure modeled into the electron density map. From the Ph.D. thesis of Silvia Seghezza.

Each β-strand is formed by hydrogen bonds between adjacent peptide backbones, whereas β-sheet stacking is stabilized by side-chain interactions, primarily hydrophobic and aromatic. The resulting structure is extraordinarily stable, resistant to proteolysis, detergents, and heat [8].

Depending on the peptide sequence, amyloid fibrils can assemble into distinct polymorphs with different cross-β arrangements. This structural diversity correlates with differences in biological activity, including cytotoxicity and seeding potential [9].

A key feature of amyloids is their ability to bind specific dyes, such as Congo Red and Thioflavin T (ThT), which are widely used for diagnostic and research purposes. Amyloid fibrils exhibit a characteristic green birefringence under polarized light when stained with Congo Red, and a marked fluorescence enhancement in the presence of ThT [10].

Advanced techniques such as cryo-electron microscopy (cryo-EM), solid-state NMR spectroscopy, and atomic force microscopy (AFM) have been instrumental in elucidating the fine molecular organization of amyloid fibrils. These studies have revealed that the

fundamental repeating unit of the fibril is the protofilament, which may assemble laterally or helically to form mature fibres [11,12].

1.4 Amyloid Pathogenicity

The pathogenicity of amyloids is a multifactorial process that involves both toxic gain of function and loss of native protein function [13]. While mature amyloid fibrils were initially thought to be the main toxic species, increasing evidence suggests that soluble oligomeric intermediates represent the primary culprits of cytotoxicity [14,15].

These oligomers can interact with cellular membranes, perturbing their integrity, forming pores, or disrupting ion homeostasis. Such interactions often trigger oxidative stress, calcium imbalance, and activation of apoptotic pathways [16]. Moreover, amyloidogenic proteins may propagate their misfolded state in a prion-like manner, acting as seeds that induce further misfolding and aggregation of native proteins [17].

Amyloid deposits can also affect the extracellular matrix (ECM), altering its mechanical properties and impairing cellular communication. This phenomenon links amyloidosis not only to biochemical dysregulation but also to biophysical alterations in the tissue microenvironment [18].

Recent studies highlight that amyloid formation is influenced by mechanical stress and surface forces, revealing a strong interplay between biophysical cues and aggregation kinetics [19]. For instance, shear stress or confinement at interfaces can accelerate fibril nucleation and growth, suggesting that the mechanical context within tissues may modulate amyloidogenesis.

Finally, the innate immune system contributes to amyloid toxicity. Microglia and astrocytes, when activated by amyloid deposits, release pro-inflammatory cytokines and reactive oxygen species, amplifying neuronal damage [20].

1.5 The neurodegenerative diseases investigated

α-Synucleinopathies

α-Synucleinopathies are a heterogeneous group of neurodegenerative disorders related to the intracellular accumulation of α-synuclein (α-syn) inclusions in neurons and glia. They are associated with several diseases, including movement disorders such as Parkinson's disease (PD), Parkinson's disease dementia (PDD), and dementia with Lewy

bodies (DLB), as well as autonomic dysfunction diseases like pure autonomic failure (PAF) and multiple system atrophy (MSA) [21].

The protein α-syn is intrinsically disordered, composed of 140 amino acid residues, and highly abundant, representing up to 1% of the total protein mass in the human brain. It consists of three main regions:

- C-terminal region (residues 96–140): negatively charged, adopts a random coil fold.
- Non-amyloid-β component (NAC) region (residues 61–95): capable of forming β-sheet structures, involved in fibrillization.
- N-terminal region (residues 1–60): positively charged, forms α-helices upon binding to phospholipid bilayers.

α-Syn is abundant at nerve terminals, and its association with lipid membranes is key to its synaptic function, although the precise role at cellular membranes remains partially unclear. Its interaction with neuronal lipid bilayers induces conformational changes: the N-terminus can form extended or broken α-helices depending on phospholipid/protein ratio and membrane curvature. In PD, α-syn misfolding generates aggregates known as Lewy bodies and Lewy neurites.

The aberrant interaction of α-syn oligomers with neuronal membranes destabilizes membrane mechanics, altering lipid packing and mobility [22,23]. Additionally, massive rises in intracellular Ca^{2+} levels have been observed, leading to ionic dyshomeostasis and mitochondrial dysfunction due to opening of the mitochondrial permeability transition pore [24].

Amyloid β and Alzheimer's Disease

Amyloid β (Aβ) peptide aggregation is a key event in the neurodegenerative process of Alzheimer's disease (AD). The Aβ family includes peptides of 37–49 amino acids derived from the amyloid precursor protein (APP). APP can undergo processing via two pathways [25,26]:

- Non-amyloidogenic pathway: cleavage by α-secretase, occurring mainly in cholesterol-poor membrane regions.
- Amyloidogenic pathway: subsequent intramembrane cleavage by γ-secretase produces Aβ peptides, predominantly Aβ1–40 and Aβ1–42, the latter being more prone to amyloid formation.

Early NMR-based models of the Aβ(1–28) fragment revealed two α-helical domains separated by a kink. These regions can transition to β-sheet structures in membrane-like environments, initiating amyloid formation. Residues 31–34 and 38–41 form a β-hairpin that restricts C-terminal flexibility, contributing to the higher amyloidogenicity of Aβ1–42.
The most neurotoxic species are prefibrillar oligomers, which trigger oxidative stress, apoptosis, and calcium homeostasis disruption [27–29]. These oligomers interact with the plasma membrane, altering microviscosity, molecular order, membrane potential, and permeability [28,30,31]. Intracellular calcium signaling is also observed, though the pathways remain unclear [32,33].

ADLD (Autosomal Dominant Leukodystrophy)

Autosomal Dominant adult-onset Leukodystrophy (ADLD) is a rare and fatal neurodegenerative disorder affecting central nervous system. It belongs to the laminopathies group and is characterized by duplications or noncoding deletions at the LMNB1 locus, resulting in excessive Lamin B1 (LB1) production [34,35].
LB1 is a key component of the nuclear lamina and, together with other lamins such as lamin A/C, contributes to maintaining nuclear structure and function [36]. Over the last few decades, it has become clear that mutations in lamin A (LA) and lamin-associated proteins can lead to a range of human disorders. These conditions, collectively known as laminopathies, include Emery-Dreifuss and limb-girdle muscular dystrophies, dilated cardiomyopathy, Dunnigan-type familial partial lipodystrophy, Charcot-Marie-Tooth disease type 2, and Hutchinson-Gilford progeria syndrome [37,38].
Dysregulation of nuclear lamina metabolism leads to white matter loss due to demyelination. ADLD onset typically occurs in the 4th–5th decade of life with autonomic symptoms, preceding cerebellar and pyramidal abnormalities, resulting in spasticity, ataxia, and tremor [39]. No therapy currently exists to cure or slow disease progression, and many aspects, such as nuclear mechanics alterations and potential physico-chemical biomarkers, remain unexplored.

The nuclear lamina is a dense network of fibrous proteins along the inner nuclear membrane and is essential for nuclear structure and integrity [40]. Composed of A- and B-type lamins, it is increasingly recognized as crucial for chromatin organization, DNA replication, cell proliferation, senescence, and aging [41,42].

Alterations in other lamins modify the nuclear lamina, impacting both the structural integrity of the nucleus and its response to mechanical stress. For instance, lamins A and C (LA/C) are crucial in determining the elastic properties of the nuclear lamina: cells lacking LA/C exhibit a higher frequency of abnormally shaped nuclei and decreased nuclear stiffness [43]. Moreover, the alteration of nuclear organization may produce secondary effects on the entire cell mechanics, which strictly depend on the genetic expression of cytoskeletal proteins at the nuclear level and on the connection between lamins and the cytoskeleton through the LINC (Linker of Nucleoskeleton and Cytoskeleton) complex. This protein complex translocates across the nuclear membrane and tethers it to cytoskeletal filaments, allowing nuclear relocation and orientation, as well as the transmission of mechanical stresses.

1.6 Bibliography

[1] Kovacs GG. *Molecular pathology of neurodegenerative diseases: principles and practice*. Journal of Clinical Pathology. 2019;72:725–735.

[2] Neri I, Ramazzotti G, Mongiorgi S, Rusciano I, Bugiani M, Conti L, Cousin M, Giorgio E, Padiath QS, Vaula G, Cortelli P, Manzoli L, Ratti S. *Understanding the Ultra-Rare Disease Autosomal Dominant Leukodystrophy: an Updated Review on Morpho-Functional Alterations Found in Experimental Models*. Mol Neurobiol. 2023;60(11):6362–6372.

[3] Chi EY, Krishnan S, Randolph TW, Carpenter JF. *Physical stability of proteins in aqueous solution: mechanism and driving forces in nonnative protein aggregation*. Pharm Res. 2003;20(9):1325–1336.

[4] Newberry RW, Leong JT, Chow ED, Kampmann M, DeGrado WF. *Deep mutational scanning reveals the structural basis for α-synuclein activity*. Nat Chem Biol. 2020;16:653–659.

[5] Willbold D, Strodel B, Schröder GF, Hoyer W, Baldus M. *Amyloid-type protein aggregation and prion-like properties of amyloids*. Chem Rev. 2021;121(13):8285–8307.

[6] Chiti F, Dobson CM. *Protein misfolding, amyloid formation, and human disease: a summary of progress over the last decade*. Annu Rev Biochem. 2017;86:27–68.

[7] Eisenberg DS, Sawaya MR. *Structural studies of amyloid proteins at the molecular level*. Annu Rev Biochem. 2017;86:69–95.

[8] Tycko R. *Molecular structure of amyloid fibrils: insights from solid-state NMR*. Q Rev Biophys. 2006;39(1):1–55.

[9] Bousset L, Pieri L, Ruiz-Arlandis G, et al. *Structural polymorphism of aggregated α-synuclein leading to distinct synucleinopathies*. PNAS. 2013;110(30):12349–12354.

[10] Groenning M. *Binding mode of Thioflavin T and other molecular probes in the context of amyloid fibrils*. Int J Mol Sci. 2010;11(2):376–397.

[11] Fitzpatrick AWP, Falcon B, He S, et al. *Cryo-EM structures of tau filaments from Alzheimer's disease*. Nature. 2017;547:185–190.

[12] Fändrich M, Meinhardt J, Grigorieff N. *Structural polymorphism of Alzheimer Aβ and other amyloid fibrils*. Prion. 2009;3(2):89–93.

[13] Soto C, Pritzkow S. *Protein misfolding, aggregation, and conformational strains in neurodegenerative diseases*. Nat Neurosci. 2018;21:1332–1340.

[14] Lambert MP, Barlow AK, Chromy BA, et al. *Diffusible, nonfibrillar ligands derived from Aβ1–42 are potent central nervous system neurotoxins*. PNAS. 1998;95:6448–6453.

[15] Haass C, Selkoe DJ. *Soluble protein oligomers in neurodegeneration: lessons from the Alzheimer's amyloid β-peptide*. Nat Rev Mol Cell Biol. 2007;8:101–112.

[16] Kayed R, Head E, Thompson JL, et al. *Common structure of soluble amyloid oligomers implies common mechanism of pathogenesis*. Science. 2003;300:486–489.

[17] Prusiner SB. *Prions*. PNAS. 1998;95:13363–13383.

[18] Knowles TPJ, Vendruscolo M, Dobson CM. *The amyloid state and its association with protein misfolding diseases*. Nat Rev Mol Cell Biol. 2014;15:384–396.

[19] Buell AK. *The physical chemistry of the amyloid phenomenon: thermodynamics and kinetics of filamentous protein aggregation*. Biochim Biophys Acta. 2019;1867(2):140–148.

[20] Heneka MT, Carson MJ, Khoury JE, et al. *Neuroinflammation in Alzheimer's disease*. Lancet Neurol. 2015;14:388–405.

[21] McCann H, Stevens CH, Cartwright H, Halliday GM. *α-Synucleinopathy phenotypes*. Parkinsonism Relat Disord. 2014;20(Suppl 1):S62–S67.

[22] Shi Z, Sachs JN, Rhoades E, Baumgart T. *Biophysics of α-synuclein-induced membrane remodelling*. Phys Chem Chem Phys. 2015;17:15561–15568.

[23] Jadavi S, Seddighi M, et al. *α-Synuclein interacts differently with membranes mimicking inner and outer leaflets of neuronal membranes*. Biochim Biophys Acta Biomembr. 2022;1864:183814.

[24] Angelova PR, Ludtmann MH, Horrocks MH, et al. *Ca2+ is a key factor in α-synuclein-induced neurotoxicity*. J Cell Sci. 2016;129:1792–1801.

[25] Lazarov O, Morfini GA, Lee EB, et al. *Axonal transport, amyloid precursor protein, kinesin-1, and the processing apparatus: revisited*. J Neurosci. 2005;25:2386–2395.

[26] Hicks DA, Nalivaeva NN, Turner AJ. *Lipid rafts and Alzheimer's disease: protein-lipid interactions and perturbation of signaling*. Front Physiol. 2012;3:189.

[27] Hermes M, Eichhoff G, Garaschuk O. *Intracellular calcium signalling in Alzheimer's disease*. J Cell Mol Med. 2010;14:30–41.

[28] Kubánková M, et al. *Molecular rotors report on changes in live cell plasma membrane microviscosity upon interaction with beta-amyloid aggregates*. Soft Matter. 2018;14:9466–9474.

[29] Terrell K, Choi S, Choi S. *Calcium's role and signaling in aging muscle, cellular senescence, and mineral interactions*. Int J Mol Sci. 2023;24:17034.

[30] Seghezza S, Diaspro A, Canale C, et al. *Cholesterol drives Aβ(1−42) interaction with lipid rafts in model membranes*. Langmuir. 2014;30:13934–13941.

[31] Sasahara K, Morigaki K, Shinya K. *Effects of membrane interaction and aggregation of amyloid β-peptide on lipid mobility and membrane domain structure*. Phys Chem Chem Phys. 2013;15:8929–8939.

[32] Tatli M, Medalia O. *Insight into the functional organization of nuclear lamins in health and disease*. Curr Opin Cell Biol. 2018;54:72–79.

[33] Gruenbaum Y, Foisner R. *Lamins: nuclear intermediate filament proteins with fundamental functions in nuclear mechanics and genome regulation*. Annu Rev Biochem. 2015;84:131–164.

[34] van Steensel B, Belmont AS. *Lamina-associated domains: links with chromosome architecture, heterochromatin, and gene repression*. Cell. 2017;169:780–791.

[35] Padiath QS. *Autosomal dominant leukodystrophy: a disease of the nuclear lamina*. Front Cell Dev Biol. 2019;7:41.

2

Methodologies

2.1 Atomic Force Microscopy

Atomic Force Microscopy (AFM) is a technique that belongs to the family of scanning probe microscopy methods, developed in the 1980s [1]. Since its inception, this instrument has experienced rapid development and widespread use in various research fields, form the Condensed Matter and Materials Physics up to Nanotechnologies and Biophysics. Scanning probe microscopy is based on the interaction between a sample and a probe that scans its surface (*figure 2-1*).

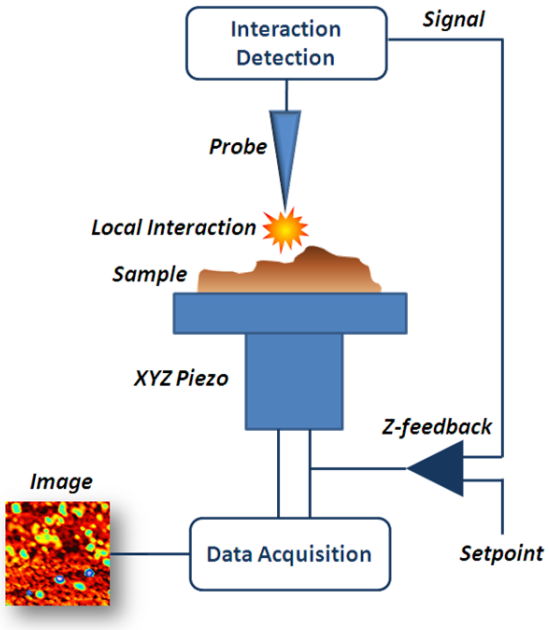

Figure 2-1: Schematic description of the AFM working mechanism.

In particular, AFM uses as a probe a micrometer-scale cantilever with a sharp tip at its end. By studying the interaction forces between the tip and the sample, it is possible to obtain information about several properties of the sample, such as the morphology of its surface or its mechanical characteristics.

At the atomic level, the interaction between the tip and the sample can be described by the Lennard-Jones potential (*figure 2-2*), which accounts for the interaction force between two atoms.

$$U(r) = 4\varepsilon\left[\left(\frac{\sigma}{r}\right)^{12} - \left(\frac{\sigma}{r}\right)^{6}\right]$$

where ε is the depth of the potential well and σ is the distance between two particles at which the potential changes sign.

The term $\left(\frac{1}{r}\right)^6$ represents the attractive dipole–dipole (Van der Waals) interaction, while the term accounts for the short-range repulsive force arising from the Pauli exclusion principle, which becomes significant when the atoms are close enough for their electron clouds or orbitals to overlap.

At short distances between the atoms that make up the tip and those on the sample surface, the repulsive forces dominate, due to the overlap of the atomic electron clouds, whereas at larger distances, the attractive Van der Waals forces become predominant.

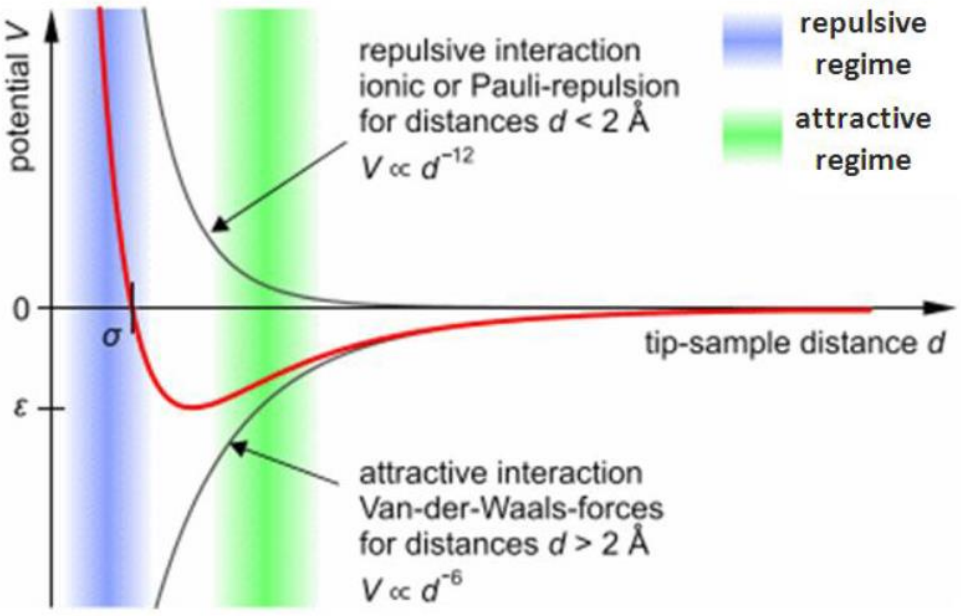

Figure 2-2: Lennard-Jones potential (red curve), describes interactions between atoms depending on their distance d. It results from the sum of two contributions, related to attractive and repulsive interactions. (from ***http://www.uni-leipzig.de/*** *- image by Steve Pawlizak, 2009).*

The term $\left(\frac{1}{r}\right)^6$ represents the attractive dipole–dipole (Van der Waals) interaction, whereas the term $\left(\frac{1}{r}\right)^{12}$ describes the short-range repulsive force arising from the Pauli exclusion principle, which becomes significant when the atoms are sufficiently close for their electron clouds or orbitals to overlap.

At very short distances between the atoms constituting the tip and those on the sample surface, the repulsive interactions dominate due to electron cloud overlap, while at larger separations, the attractive Van der Waals forces prevail.

The operating modes of AFM are distinguished based on the type of interaction between the tip and the material under analysis, as will be discussed in the following sections. It is possible to determine the interaction between the tip and the sample by measuring the deflection of the cantilever.

Its behavior can be approximated to that of a spring, and the interaction force with the sample can be described by Hooke's law:

$$F = -K\,\Delta x$$

where K is the spring constant of the cantilever and Δz is its deflection. To measure the deflection, a method based on the optical lever principle is commonly used. The back side of the cantilever is coated with a reflective material, onto which a laser beam is focused near its free end. The reflected beam is then directed onto a four-quadrant photodiode(*figure 2-3*).

The presence of four quadrants makes it possible to detect not only vertical deflections, providing information about the sample's morphology, but also torsional motions in the horizontal plane, from which the tribological properties of the sample can be inferred. Each quadrant of the photodiode receives a specific light intensity, denoted as $I_1, I_2, I_3\ and\ I_4$. The vertical deflection can be calculated from the following ratio:

$$\text{Vertical deflection:} \quad \frac{(I_1 + I_2) - (I_3 + I_4)}{I_{\text{tot}}}$$

$$\text{Lateral deflection:} \quad \frac{(I_1 + I_4) - (I_2 + I_3)}{I_{\text{tot}}}$$

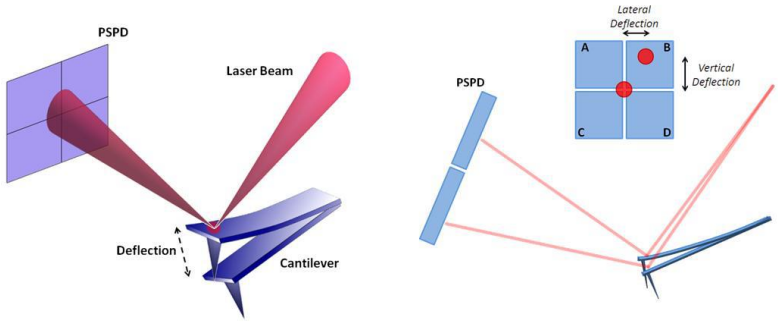

Figure 2-3: Simplified scheme of AFM photodetection system (optical path elements are not shown). Cantilever deflection results in a shift in laser spot position on PSPD. AFM main signal (vertical deflection) is calculated from (A+B)-(C+D), while frictional torsion (lateral deflection) is (A+C)-(B+D).

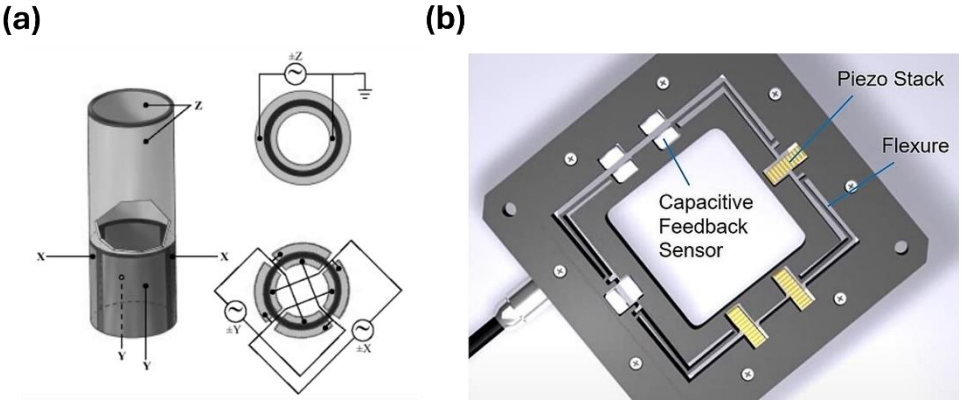

Figure 2-4:(a) Schematic representation of a piezoelectric tube.

The scanning process is commonly performed using piezoelectric tubes [2], which are materials capable of undergoing extremely precise deformations when subjected to potential differences.

To enable movement in the three spatial directions, two pairs of electrodes are typically used for displacements along the *x* and *y* axes, and a third pair of electrodes for motion along the *z* axis.

Alternatively, some instruments employ stacks of piezoelectric actuators [3], which allow for a significant increase in the scanning area while minimizing issues of nonlinearity and hysteresis that may occur during large-area scans when using piezoelectric tubes (*figure 2-4*).

The polarization applied to the piezoelectric actuator to produce movement along the *x*, *y*, and *z* directions is controlled by an appropriate feedback network.

As previously discussed, the operating modes of the microscope are distinguished by the type of interaction between the tip and the sample, as illustrated in *figure 2-5*.

Contact Mode:

In this regime, the tip remains in constant contact with the sample during scanning. Within this mode, two possible acquisition methods can be employed: constant height and constant force.

In the first case, the distance between the rear end of the cantilever and the sample is kept constant, and the deflection of the free end of the cantilever is measured during scanning, resulting from the interaction between the tip and the sample. In the second case, a feedback system maintains a constant deflection of the cantilever (and therefore a constant interaction force between the tip and the sample) by continuously adjusting the vertical position of the piezo.

By recording the cantilever deflection data (in the constant-height method) or the vertical piezo voltage at each point (in the constant-force method), it is possible to obtain an image of the sample's morphology. Conversely, by acquiring data related to the cantilever torsion, information about the tribological properties of the sample can be obtained.

This operating mode is characterized by a repulsive interaction between the probe and the surface. For this reason, it may be excessively invasive for soft samples, such as many biological specimens, posing a risk of damaging the sample or producing image artifacts caused by drag effects.

Intermittent Contact or Tapping Mode:

In this regime, the cantilever is made to oscillate near the sample at a frequency close to its resonance frequency. In this way, the interaction alternates between the contact region, dominated by repulsive forces, and the non-contact region, where Van der Waals attractive forces prevail.

The feedback system adjusts the *z*-axis piezo polarization to maintain a constant oscillation amplitude. The topographic image is reconstructed from the data corresponding to variations in the *z*-piezo polarization.

Operating in tapping mode also provides additional information about the surface properties under investigation by analyzing the phase signal of the cantilever oscillation.

This signal is particularly useful, for example, in the study of polymeric samples, as it can provide insights into the viscoelastic properties of the material.

Since the tip is in contact with the sample only for a fraction of each oscillation, the tapping mode is less invasive than the contact mode, making it more suitable for the study of soft samples.

Non-Contact Mode:

An even less invasive approach than tapping mode can be achieved by oscillating the cantilever at a distance such that the tip never comes into contact with the sample. However, this mode is rarely used, as it provides lower resolution compared to the previous methods. This limitation arises because only attractive forces are involved, which have a weaker dependence on distance than repulsive forces.

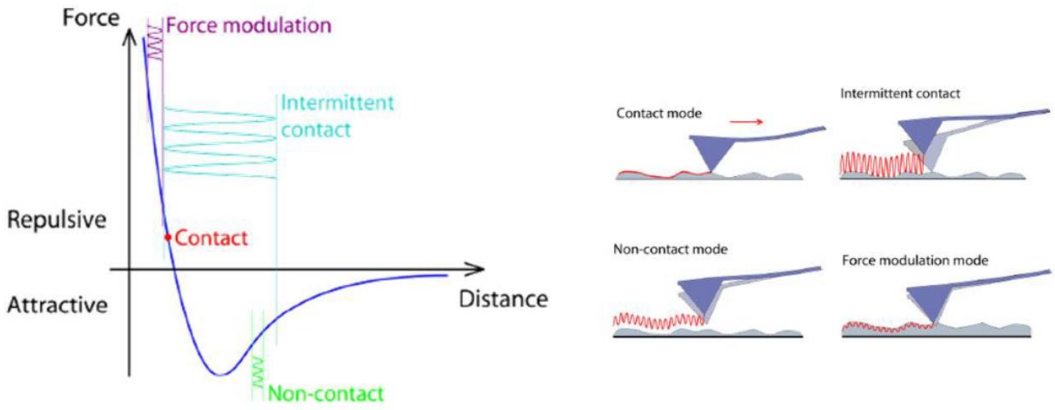

Figure 2-5: Left: Different AFM operating modes corresponding to regions of the Lennard-Jones potential. Right: Schematic illustration of the various AFM working modes.

Quantitative Imaging:

This imaging mode enables the simultaneous acquisition of topographical maps and mechanical property maps of the sample by recording a complete force–distance curve at every pixel. Unlike conventional tapping or contact modes, QI mode controls the tip–sample interaction through a precise approach–retract cycle, minimizing lateral forces and reducing the risk of sample deformation or damage. Each indentation event provides local information on height, stiffness, adhesion and other mechanical parameters, resulting in high-resolution nanoscale maps, which will be introduced in the following section (*figure 2-6*).

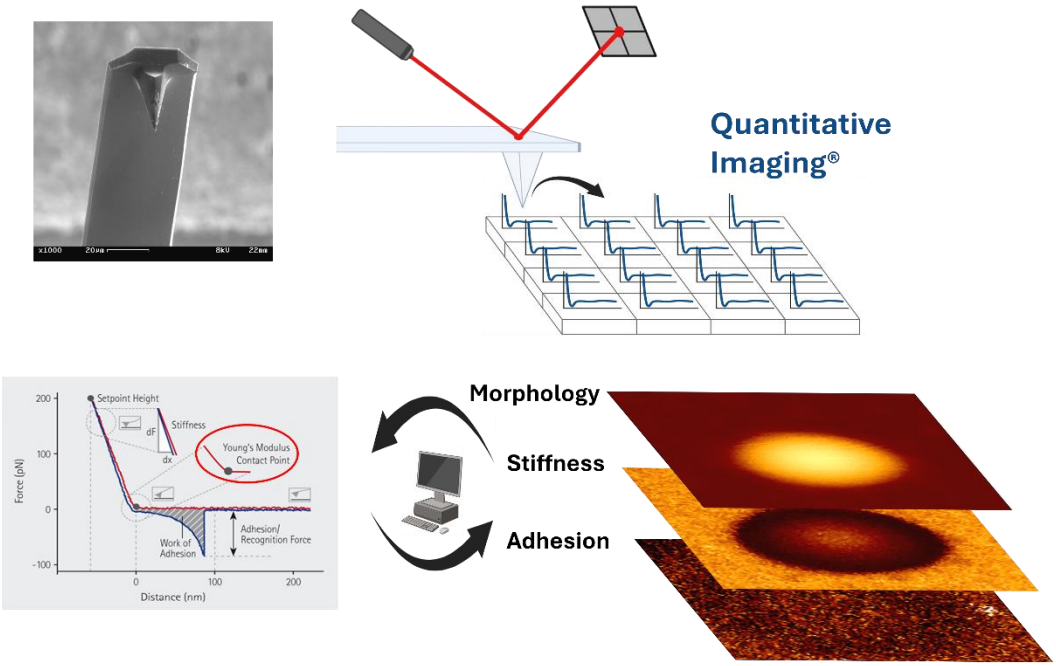

Figure 2-6: Cartoon illustrating the AFM experimental procedure using the Quantitative Imaging (QI) mode, highlighting the generation of various maps through the analysis of individual force–distance curves.

The Force-Distance Curve

The high spatial resolution (below one nanometer) and the ability to measure forces on the order of piconewtons (pN) make AFM a tool capable of locally applying and recording extremely small forces with great precision [4].

Thanks to these characteristics, AFM is extremely valuable not only as an imaging technique, but also as a force sensor, through the acquisition of the so-called force–distance curves.

In this case, with the tip position fixed in the *(x, y)* plane, the tip performs a cycle of approach and retraction relative to the sample surface, while the cantilever deflection is recorded as a function of the vertical displacement of the piezo. From the deflection signal, knowing the spring constant of the cantilever, the corresponding force signal can be obtained.

figure 2-7 shows the general features of the force–piezo displacement curve obtained on an infinitely rigid sample.

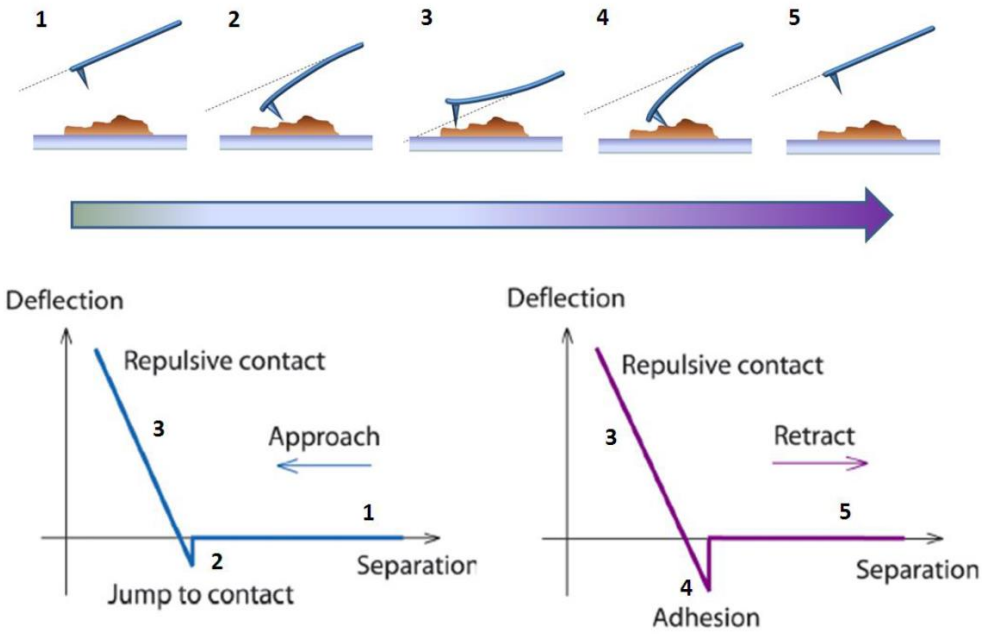

Figure 2-7: Schematic representation of a force vs distance curve. Tip approaching (left) and retracting (right) are represented separately.

During the approach phase, the initial portion of the curve corresponds to the movement of the tip toward the sample surface, where no significant interaction forces are present. When the distance decreases to the point where the gradient of the attractive Van der Waals forces exceeds the cantilever's spring constant, the tip is suddenly pulled into contact with the surface, causing a negative deflection of the cantilever. This phenomenon is known as the "jump to contact."

Once contact is established, the cantilever is progressively deflected upward, following a linear trend until it reaches the desired force setpoint defined by the user.

The approach phase is followed by the retraction phase, during which the tip moves away from the sample and returns to its initial position. Initially, there is a gradual decrease in deflection, following the same trend as the approach curve.

To achieve tip disengagement from the sample (the so-called "jump-off contact"), the tip must be retracted to a distance greater than that at which the jump to contact occurred during the approach phase, reaching larger negative deflections than those measured during approach.

This behavior is due to the adhesion forces established during the contact phase, which keep the tip anchored to the sample. Finally, a sudden detachment of the tip from the

contact region occurs, followed by its separation from the sample, at which point the cantilever deflection returns to zero.

The AFM Calibration

To convert the signal related to the cantilever's vertical deflection (expressed in volts) into a signal corresponding to the interaction force between the tip and the sample, two main steps must be followed.

The first step consists of determining the sensitivity of the optical lever. This is done by acquiring a force–distance (F–D) curve on a rigid substrate. Since a rigid substrate does not deform, the cantilever deflection upon contact with the sample is directly proportional to the distance it travels. The optical lever sensitivity (OLS) is then obtained by dividing the photodiode voltage by the corresponding displacement.

In AFM, the relevant parameter is the distance, so the inverse of this ratio, referred to as the invOLS (inverse optical lever sensitivity), is typically used. It is expressed in nanometers per volt (nm/V).

The second step involves determining the spring constant of the cantilever. As previously discussed, the AFM cantilever behaves like a spring and therefore follows Hooke's law. To measure the cantilever spring constant, two common methods are employed: the Sader method [5] and the thermal noise method [6]. In this study, the thermal noise technique was used.

In the thermal noise method, the cantilever is modeled as a simple harmonic oscillator (SHO) that undergoes oscillations due to thermal motion. By analyzing its thermal spectrum, it is possible to determine the mean square displacement of the cantilever $\langle d^2 \rangle$ and subsequently calculate the spring constant using the equipartition theorem [7, 8]:

$$\text{statistical thermodynamic energy: } E = \frac{1}{2} k_B T$$

Where k_B is Boltzmann constant, and T is temperature.

$$\text{Energy of resonance frequency: } E = \frac{1}{2} k d^2$$

K is the spring constant, and d is the displacement of the tip,

$$\frac{1}{2}\langle kd^2\rangle = \frac{1}{2}k_B T$$

Therefore:

$$k = \frac{k_B T}{d^2}$$

The applied force (N) can be determined by multiplying the spring constant (N/m) by the sensitivity (nm/V) and the measured cantilever deflection (V).

After completing the calibration procedure, the signal shown in Figure 2-8 represents the relationship between the applied force and the indentation of the sample. The Young's modulus of elasticity describes the correlation between these two parameters. Therefore, it is essential to extract the Young's modulus (E) from this curve.

To do so, it is necessary to identify the contact point and apply an appropriate contact model. Several contact models have been developed, each considering factors such as the geometry of the indenter (probe) and specific assumptions regarding the forces involved in the tip–sample interaction. The most relevant of these models are discussed below.

AFM as Force Spectroscopy Technique

The analysis of force–distance curves can provide valuable information about various properties of the system under investigation, ranging from the study of inter- and intramolecular interactions to the examination of the mechanical properties of the sample.

By functionalizing both the tip and the surface with appropriate molecules, AFM can be exploited to study specific molecular interactions. In the case of intermolecular interactions between two partner molecules (for example, a ligand–receptor interaction, as illustrated in Figure 2-8a, suitable molecular cross-linkers are used to anchor the molecules of interest to the tip and the surface.

Upon approaching the tip to the surface, a bond forms between the paired molecules.

During the subsequent retraction phase, the microscope applies a mechanical stress to the bond, eventually causing its rupture [9].

By analyzing the evolution of the interaction force during the retraction phase, it is possible to obtain information on the physicochemical properties of the interaction between the two molecules.

Using a similar approach, it is possible to investigate the intramolecular forces that stabilize the three-dimensional structure of complex biological macromolecules composed of structural subunits, such as proteins. An example of this is the study of the unfolding process of a macromolecule made up of multiple subunits [10].

As shown in Figure 2-8b, the force curve obtained during the retraction phase exhibits a sawtooth pattern, where each peak corresponds to the unfolding of an individual subunit.

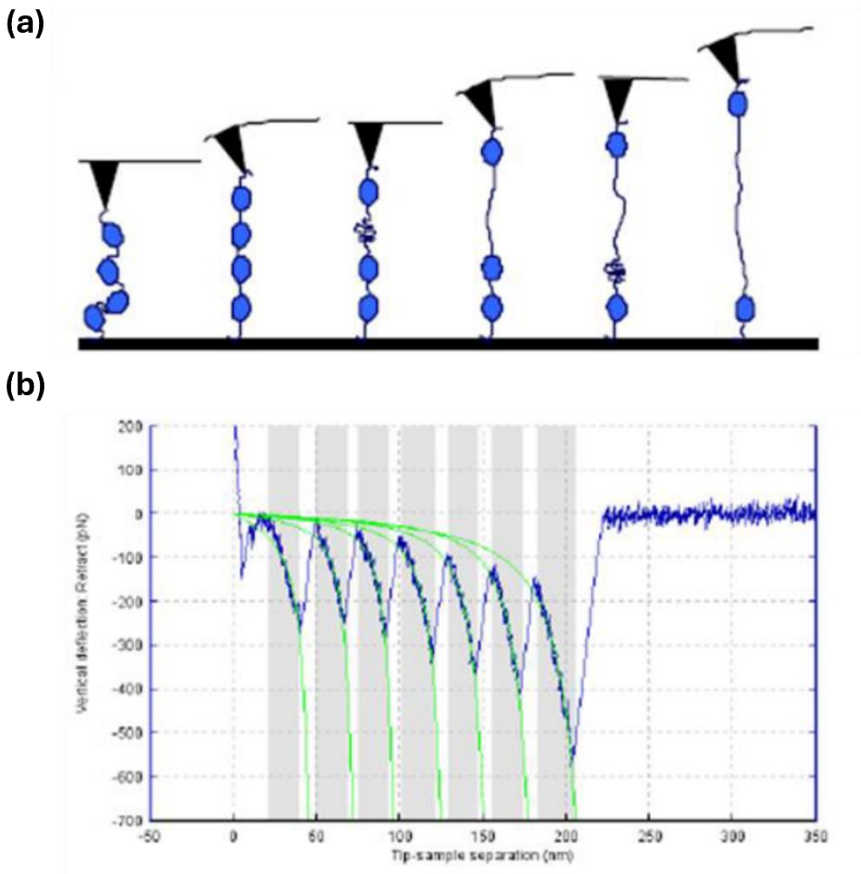

Figure 2-8: (a) Determination of Elastic Modulus with AFM. Considering tip geometry, force vs tip-sample separation curve can be fitted with Hertz model to determine Young's Modulus (b) Schematic diagram of titin stretching, as successive globular domains unfold (top); force curve of titin stretching, showing sequential unfolding of globular domains, fitted with worm-like-chain model. From Hoffmann, Toni, and Lorna Dougan. Chemical Society Reviews 41.14 (2012): 4781-4796.

By applying models such as the Worm-Like Chain (WLC) model [11], it is possible to analyze the structural properties of the different subunits and the intramolecular interactions that stabilize them.

These techniques, in which the inter- and intramolecular interactions are investigated, are collectively referred to as Single-Molecule Force Spectroscopy (SMFS) [12].

Another type of information that can be extracted from the analysis of force–distance curves concern the local mechanical properties of deformable samples.

In the case of soft samples, the force–distance curves exhibit a different behavior compared to rigid samples, as illustrated in *figure 2-9*.

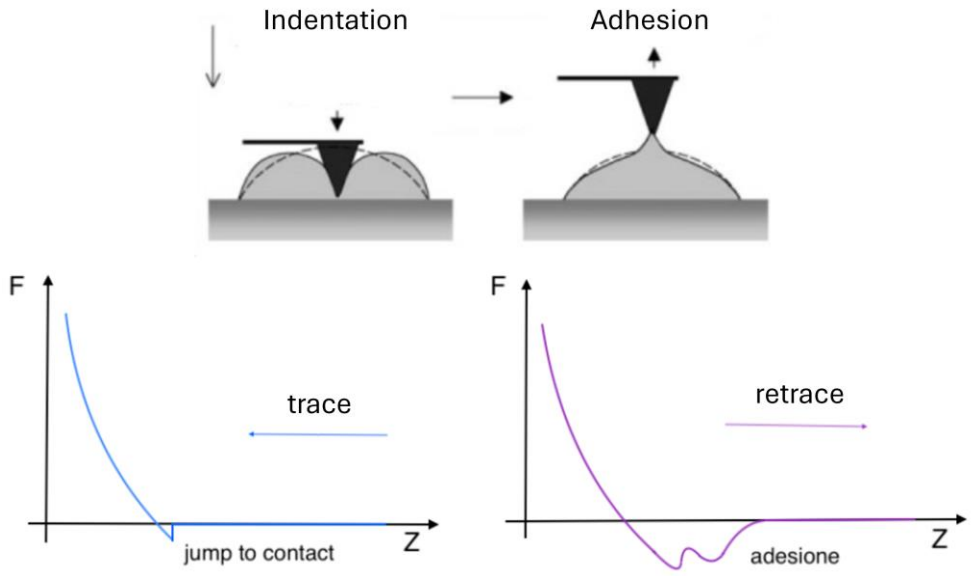

Figure 2-9: Illustration of the force–distance curve behavior on a deformable sample. From: Ebeling, D., et al. ACS nano 7.11 (2013): 10387-10396.

In this situation, the tip deforms the sample, and the cantilever deflection in the contact region no longer follows a linear trend. This occurs because the piezo displacement results partly in cantilever deflection and partly in sample indentation. The indentation δ of the sample can be calculated as the difference between the piezo displacement and the cantilever deflection (Figure 2.6):

$$\delta = z_p - d - \Big(z_p(CP) - d(CP)\Big),$$

where z_p is the piezo displacement, d is the cantilever displacement and CP is the contact point.

Furthermore, for deformable samples, the adhesion forces that develop during the contact phase and oppose the detachment of the tip from the sample are manifold and can lead to a more irregular shape of the force–distance curve compared to that of a rigid sample.

From the analysis of the force–distance curves of deformable materials, it is possible to evaluate the mechanical properties of the sample. The quantities most commonly used

to quantitatively describe these properties are the stiffness and the elastic (Young's) modulus.

The sample stiffness can be estimated from the force–distance curve as the incremental slope of the curve in the contact region (figure *2-10*). This provides a preliminary assessment of the sample's elastic properties without the need to apply a specific tip–sample interaction model.

For a more accurate evaluation of the mechanical properties, the elastic modulus of the sample can be determined using an appropriate contact model. Several models have been developed to relate the elastic modulus of a material to the indentation caused by the tip as a function of the applied force, such as the Hertz–Sneddon model for axisymmetric indenters [13].

$$F_{cyl} = \frac{2E}{1-\nu^2} R\delta$$

$$F_{sph} = \frac{4E}{3(1-\nu^2)} R^{1/2}\delta^{3/2}$$

$$F_{pyr} = \frac{3E\tan\theta}{4(1-\nu^2)}\delta^2$$

$$F_{cone} = \frac{2E\tan\theta}{\pi(1-\nu^2)}\delta^2$$

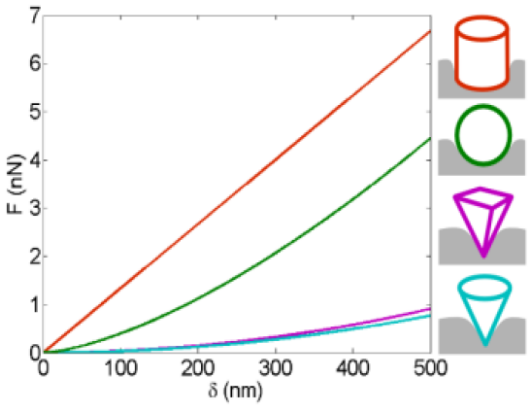

Figure 2-10: The relationship between force and indentation according to different tip shapes. It becomes evident that sharper tips require less force to achieve the same level of indentation in the sample. From Rigato, Annafrancesca, Diss. Aix-Marseille, 2015.

From the value of δ and assuming, for biological samples, a Poisson's ratio $\nu = 0.5$, it is possible to determine the local Young's modulus of the material. This type of analysis is performed by considering the portion of the force–distance curve near the contact point. This model is based on the assumption that the sample behaves as a perfectly elastic and isotropic material.

In cases where the analyzed sample exhibits plastic behavior, resulting in an irreversible deformation, this manifests in the force–distance curves as a hysteresis between the approach and retraction curves.

As previously mentioned, each force–distance curve is acquired at a single point on the sample, allowing for the determination of the mechanical properties at that specific location.

To characterize a larger area, it is possible to construct a map of force–distance curves.

In this case, the cantilever performs a series of measurements over a grid of points, changing its position along the horizontal plane. This technique is known as Force Volume [14].

From these sets of curves, it is possible to extract maps that represent various quantities as functions of spatial coordinates, such as height, Young's modulus, and tip–sample adhesion [15].

However, the Force Volume technique has the drawback of requiring a long acquisition time to complete a single map. This limitation makes it suitable only for maps with a relatively small number of points, resulting in low spatial resolution.

A technique based on the same principle as Force Volume, but capable of overcoming the issue of long acquisition times, is Quantitative Imaging (QI) [16].

The higher acquisition speed typical of QI is achieved through improved electronics, which allow for faster and more precise horizontal movement of the cantilever by means of a closed-loop feedback system on the *xy*-plane. All the AFM images presented in this thesis were acquired using the QI mode.

2.2 Brillouin Microscopy

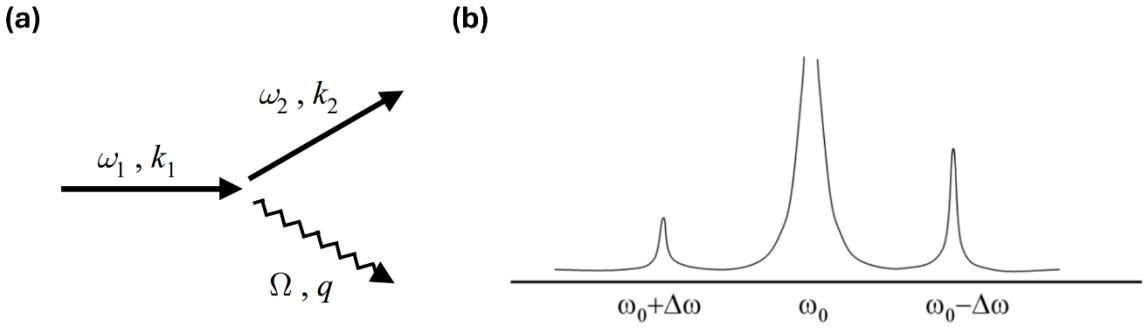

Figure 2-11: (a) Feynman diagram of Brillouin inelastic scattering. (b)Illustration of a spectrum where the central big peak represents the elastic Rayleigh scattering, and the peripheral peaks of Brillouin and Raman on the left and right shows the smaller portion of light that undergoes the inelastic scattering with frequency shift of Stoke and anti-Stoke respectively.

Brillouin Light Scattering (BLS) is a type of inelastic light scattering in which photons interact with the acoustic phonons of a material (*figure 2-11*). The optical field induces acoustic waves in the medium, leading to a periodic modulation of its density and, consequently, of its refractive index. This modulation causes the light to scatter at shifted frequencies [17]. Conversely, the incident optical field can also generate acoustic waves in the material through spatial and temporal variations in elastic strain [18].

These two coupled mechanisms result in two types of scattered light: one that gains energy from existing acoustic waves, corresponding to a frequency upshift (anti-Stokes scattering), and one that loses energy by generating acoustic waves in the medium, corresponding to a frequency downshift (Stokes scattering).

The physical principle of BLS is closely related to Raman Light Scattering (RLS). The key difference is that RLS involves interactions between photons and optical phonons, and so with vibrational or rotational modes of neighboring atoms; while BLS involves acoustic phonons, which correspond to collective low frequency vibrational modes of the lattice. Consequently, Raman spectroscop**y** provides information about molecular bonding and chemical composition at the microscopic level, whereas Brillouin spectroscopy probes macroscopic elastic properties such as the longitudinal modulus and viscosity.

The frequency shift observed in BLS is typically very small, on the order of 10^{-1} cm^{-1}, compared with 10^{2}–10^{4} cm^{-1} in RLS, and the corresponding signal intensity is about 10^{3} times weaker. These characteristics make BLS experimentally challenging: interferometric methods are required to filter the weak Brillouin peaks from the intense Rayleigh scattering, and advanced post-processing is necessary to isolate the BLS contribution.

From a Brillouin spectrum, the two key parameters are the Brillouin frequency shift (ω_B) and the linewidth (Γ_B), defined as the Full Width at Half Maximum (FWHM) of the intensity peak. These spectral quantities can be used to derive the longitudinal elastic modulus of the material, directly linking optical measurements to its mechanical properties.

Longitudinal Modulus

Considering a biological sample, we can assume that it behaves as a viscoelastic material, characterized by a frequency-dependent complex elastic modulus.
In this framework, the Brillouin peak can be modeled using a Damped Harmonic Oscillator (DHO) function [19], which describes the response of an acoustic mode with characteristic frequency ω_B and linewidth Γ_B:

$$I_B(\omega) = I_0 \frac{\Gamma_B \omega_B^2}{\pi(\omega^2 - \omega_B^2)^2 + (\Gamma_B \omega_B)^2}$$

Were I_0 is the intensity of the incident light beam.

From ω_B and Γ_B derived from fit analysis of Brillouin peaks we can define the longitudinal modulus, defined as the ratio of axial stress to axial strain when strains in all other directions are equal to zero.

$$M^* = M' + iM''$$

$$M' = \rho\omega_B^2/q^2$$

$$M'' = \rho\omega_B\Gamma_B/q^2$$

Where ρ is the density of the material and q is momentum exchanged in the scattering process.

It is complex quantity where the real part is associated to the storage modulus and the imaginary part to the loss modulus: the conservative term M' is related to the elasticity of the sample, while the dissipative term M'' is related to the viscosity.

The typical values of the Longitudinal modulus for biological sample is reported in *figure 2-12 [29]*.

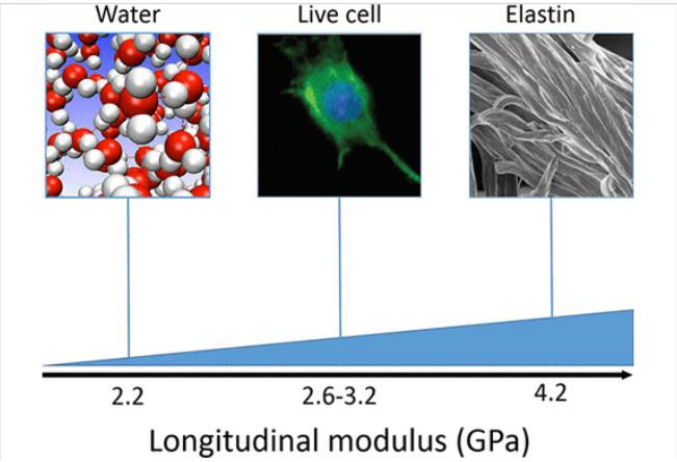

Figure 2-12:The longitudinal modulus of three representative samples: pure water, a living cell, and elastin fibers.

By integrating the Brillouin spectroscopic setup with a scanning optical microscope, such as a confocal microscope, it is possible to acquire Brillouin maps of the sample. This approach enables the investigation of the mechanical properties of complex and heterogeneous materials with micrometer-scale spatial resolution, providing insight into local variations in elasticity and viscosity across the specimen.

Experimental Setup

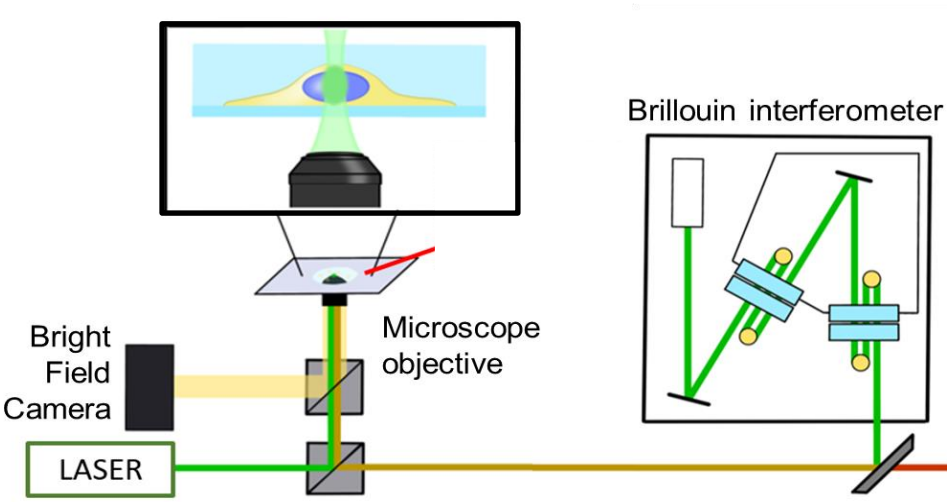

Figure 2-13:Brillouin experimental setup .

Due to the weak scattering interaction of light with the sample, it is essential to employ powerful illumination sources, such as lasers. However, the use of high-power lasers may induce phototoxic effects in biological specimens. To achieve an optimal balance, the total light dose delivered to the sample must be carefully evaluated by considering the product of illumination intensity and exposure time. Therefore, a trade-off arises between enhancing Brillouin scattering and minimizing the risk of photodamage.

In our configuration (*figure 2-13*), a green diode-pumped solid-state laser (Spectra-Physics Excelsior, 532 nm) is employed. The laser beam passes through a temperature-controlled etalon (TCF-1, JRS Scientific Instruments, Tablestable Ltd., Mettmenstetten, Switzerland), which is specifically designed to suppress unwanted secondary laser modes within the spectral range relevant to Brillouin measurements. The filtered beam is then directed onto the sample via a confocal arrangement (JRS Scientific Instruments). Subsequently, the light reaches a corner cube/beam splitter.

The beam splitter diverts a fraction of the light to the reference input of the Brillouin interferometer (TFP2) for self-tuning and stabilization. This feature is particularly crucial in backscattering configurations, where a strong elastic component could otherwise saturate or damage the photon-counting system. To mitigate this, the elastic peak is blocked during inelastic peak scanning, while the reference beam is used to maintain spectrometer stability. This functionality is achieved through a shutter subsystem integrated with the control unit.

The remaining portion of the light is directed through a confocal microscope, illuminating the sample with a water-immersion objective (NA = 1.2). The sample is mounted on a piezoelectric translation stage operating at high voltage, offering a travel range of 100 µm per axis and a positioning resolution of 1 nm. After interaction with the sample, the same objective collects the backscattered light. The scattered light is then gathered and spectrally separated using a tunable ultrasteep short-pass filter (TEF, Semrock SP01-561RU). This filter transmits the quasi-elastic scattered component to the Fabry–Pérot tandem interferometer (TFP-2 HC, JRS Scientific Instruments) while reflecting the inelastically scattered light toward the Raman spectrometer (Horiba iHR320 Triax).

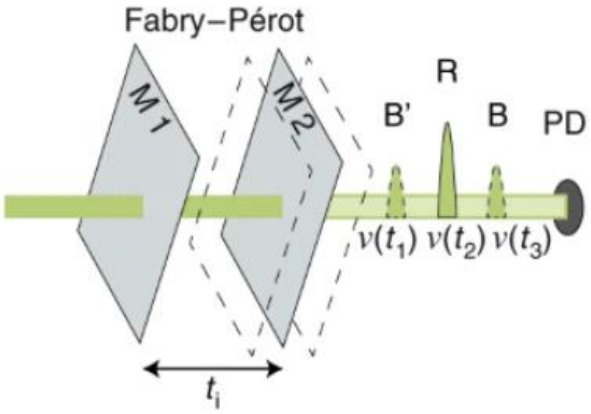

Figure 2-14: A Fabry-Pérot interferometer is comprised of two partially transparent mirrors and depending on the distance between them (ti), they only allow a specific light frequency to pass through. By adjusting the separation between the mirrors, it becomes possible to capture a complete spectrum encompassing both Rayleigh and Brillouin peaks.

In our Brillouin setup, a Fabry–Pérot (FP) interferometer is employed (*figure 2-14 [30]*).
A Fabry–Pérot interferometer consists of an optical cavity formed by two highly reflective surfaces positioned parallel to each other and separated by a distance *d*. For a given spacing *d*, the interferometer transmits only specific wavelengths (*λ*) according to the following condition:

$$T = \frac{\tau_0}{1 + \left(\frac{2F}{\pi}\right)^2 sin^2\left(\frac{2\pi d}{\lambda}\right)}$$

Where τ_0 is the maximum transmit of the system considering the losses, F is the Finess of the mirror which depends on the mirror reflectivity and flatness.

$$F = \frac{\pi\sqrt{R}}{1-R} = \frac{\Delta\lambda}{\delta\lambda}$$

Where R is the mirror reflectivity. Finess is also defined as the free spectral range divided by the bandwidth (full width at half-maximum). It gives the relative separation between nearest transmission peaks.

Therefore, only wavelength satisfying the flowing equation are transmitted:

$$d = n\frac{\lambda}{2}$$

The distance between successive wavelength that can pass through the mirrors is called free spectral range (FSR). The FSR defines the frequency range that can be analyzed, and it is given by:

$$\Delta\theta = \Delta\lambda = \frac{c}{2d}$$

To scan different wavelengths the space between the mirrors needs to be changed. In order to increase the FSR at fixed resolution, two FP in series, placed one after the other, can be used. Therefore, the transmitted wavelength should satisfy both of the following equations:

$$d_1 = n\frac{\lambda}{2}, \;\; d_2 = m\frac{\lambda}{2}$$

In the configuration where the spacing between the mirrors of the second interferometer (d_2) is kept close to that of the first one (d_1), the light successively passes through both FP1 and FP2, as illustrated in *figure 2-14*. This arrangement ensures that adjacent transmission peaks do not overlap; however, small residual contributions from intermediate transmission peaks remain, since the transmission of each interferometer never reaches absolute zero.

A practical ratio of $L_2 / L_1 \approx 0.95$ provides optimal performance. Under these conditions, the tandem configuration substantially increases the measurable range of frequency shifts compared to a single interferometer, while maintaining a comparable spectral resolution. An illustration of the tandem setup is shown in Figure 2-18.

After passing six times through the tandem interferometer—three passes in each FP—the light is finally detected by a single-photon avalanche diode (SPAD) detector (Laser Components COUNT-10 SPAD).

This Tandem configuration proves highly efficient in suppressing the occurrence of duplicated inelastic signals stemming from consecutive orders.

2.3 Optical Microscopy and Calcium Imaging

Optical microscopy is the most common light microscopy technique and allows the magnification of objects using optical lenses and a light source. A traditional optical microscope consists of a light source, a condenser, an objective lens, an eyepiece, and a stage. The light source illuminates the specimen, and the condenser focuses the light onto it. The objective lens then magnifies the image of the specimen, while the eyepiece provides additional magnification so that the image can be observed by the user.

As with all microscopy techniques, the resolution of the instrument is a key factor to consider when determining the length scale of the sample that can be analyzed. The resolving power of a microscope is fundamentally limited by diffraction, which is the spreading of light waves as they pass through apertures or around obstacles.

In 1873 [20], Ernst Abbe described the resolution limit of an optical microscope as follows:

$$d = \frac{\lambda}{2nsin\alpha}$$

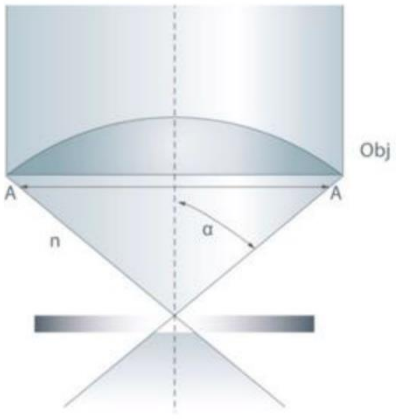

Where d is the smallest distance resolved, λ is the wavelength of the light, n is the refractive index and α is the half-opening angle of the objective lens.

Considering the best conditions of low wavelength, and maximizing the denominator using large angle objectives and oils with high refractive index (≈ 1.5) we obtain a maximal resolution of circa 250 nm.

Another key point of this technique is the contrast: the possibility to distinguish the object of interest from the background. There are different techniques to increase the optical contrast of biological samples. A very common and powerful method is the use of fluorescent molecules to label specific regions of the sample and increase their contrast form the bachground.

Where d is the smallest resolvable distance, λ is the wavelength of the light, n is the refractive index of the medium, and α is the half-opening angle of the objective lens. Under optimal conditions—using a short wavelength, maximizing the numerical aperture with large-angle objectives, and employing immersion oils with a high refractive index (≈1.5), the maximal resolution achievable with a conventional optical microscope is approximately 250 nm.

Another key aspect of optical microscopy is contrast, which is the ability to distinguish the object of interest from the background. Several techniques exist to enhance the optical contrast of biological samples. One of the most common and powerful methods is the use of fluorescent molecules to specifically label regions of the specimen, thereby increasing their contrast relative to the surrounding background.

The fluorescence process involves the interaction of light ($h\nu$) with fluorochromes, promoting them from their singlet electronic ground state to an unstable excited state. In this excited state, the fluorochromes undergo nonradiative relaxation, dissipating energy until they reach the lowest vibrational level of the excited state. Subsequently, the fluorochromes return to the ground state by emitting a photon ($h\nu'$), which has lower energy than the excitation photon ($\nu' < \nu$). This difference in energy between absorption and emission is known as the Stokes shift, and it is critical for fluorescence imaging because it allows the emitted light to be separated from the excitation light, improving the signal-to-background ratio. The energy states and transitions of fluorescent molecules are commonly illustrated using a Jablonski–Perrin diagram reported in *figure 2-15*.

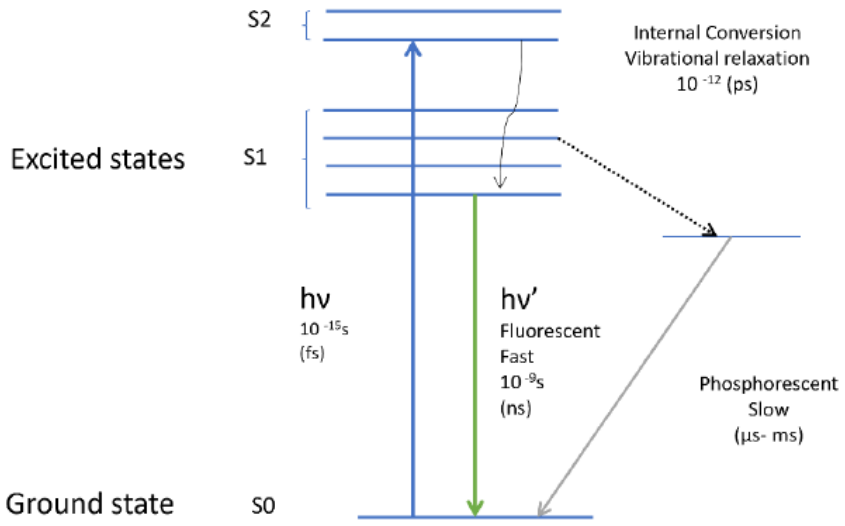

Figure 2-15:The Jablonski-Perrin diagram. From PhD Thesis of Sajedeh Kerdegari.

Fluorescent molecules can be conjugated to antibodies that specifically recognize antigens on cellular organelles, enabling the selective labelling of defined regions within biological samples.

However, the use of fluorescent dyes is not limited to marking the location of specific structures. There is a category of fluorescent probes that are sensitive to various features of the intracellular environment, such as pH, temperature, ion concentration, or membrane potential, allowing dynamic monitoring of cellular physiology in real time.

The focus of this thesis is about the calcium homeostasis and the activity of calcium channels mechanosensitive.

Calcium indicators allow simultaneous detection of neural activity and visualization of intracellular Ca^{2+} levels [21,22]. Scientists have attempted to measure intracellular Ca^{2+} levels since the 1920s, but technical challenges have persistently hindered progress [23]. In the 1960s, Ridgway and Ashley were the first to accurately measure calcium levels through the injection of aequorin, a photosensitive protein, into barnacle muscle cells [24].

The Intracellular Calcium Indicators

Today, a wide range of synthetic calcium-sensitive fluorescent molecules is available to monitor cytosolic calcium dynamics at the neuronal level. Cells can be stained with calcium indicators using different approaches: one option is the use of genetically encoded fluorescent indicators (GEFIs), which are expressed by the cells following DNA

transfection; another common method is the use of synthetic membrane-permeable fluorescent dyes, which are rendered cell-permeant through esterification with acetoxymethyl (AM) groups and are therefore referred to as AM dyes. The genetic modification of cellular DNA to express calcium indicators provides a reliable and long-term strategy, enabling repeated measurements on the same cells or tissue samples without the need to replace the specimen or expose it to additional external agents before each experiment. Furthermore, GEFIs make it possible to label specific cell subpopulations with high selectivity.

Nevertheless, GEFIs also present several limitations: viral delivery or transfection procedures may alter cellular physiology, expression levels often vary between cells, and the indicators themselves may buffer intracellular calcium or exhibit unwanted pH sensitivity.

The use of AM dyes represents a more invasive approach and does not allow multiple stainings of the same sample. However, synthetic dyes generally provide higher brightness, improved signal-to-noise ratio, and excellent temporal resolution. This second category of calcium indicators is therefore particularly suitable for in vitro experiments, where spatial and temporal resolution are crucial experimental requirements.

In the work presented in this thesis, the genetic approach was not used for cell staining, instead AM dyes were employed.

These dyes can be grouped into two main operational classes: single-wavelength (SW) intensity-modulating indicators and dual-wavelength ratiometric (WR) indicators.

SW dyes, such as Fluo-4 and Oregon Green BAPTA-1, are characterized by a single excitation wavelength. Their fluorescence intensity increases proportionally with the intracellular calcium concentration, without significant shifts in excitation or emission spectra. These indicators are generally bright and capable of exhibiting large fluorescence changes (often 30-fold or more) upon Ca^{2+} binding, making them highly suitable for detecting rapid fluctuations in calcium levels with excellent temporal resolution.

WR dyes, such as Fura-2 and Indo-1, possess two distinct excitation wavelengths: one corresponding to the Ca^{2+}-free state and the other to the Ca^{2+}-bound state of the molecule. When imaging with a WR dye, the sample is sequentially excited at these two wavelengths, yielding two fluorescence signals. The ratio between these signals provides

quantitative information on the intracellular calcium concentration, offering a significant advantage over SW dyes, which only report relative changes in fluorescence intensity.
However, the use of WR dyes comes with certain limitations. The need for dual-wavelength excitation reduces the achievable frame rate and increases the risk of photobleaching and phototoxicity, particularly when excitation wavelengths fall within or near the UV range [25]. Conversely, SW dyes do not allow for absolute quantification of calcium levels, but they permit higher temporal resolution and reduced photodamage during imaging [26].

The Fluorescence Detectors

Another important aspect to consider in fluorescence microscopy experiments is the detector used to acquire information from the sample. While the eyepiece and the human eye can provide valuable qualitative insights, the use of an artificial detector is essential for recording quantitative data and accurately characterizing the observed phenomenon.
The ideal detector for fluorescence signal acquisition should exhibit high sensitivity to capture the weak photon emissions produced by fluorophores and a very high signal-to-noise ratio, enabling reliable extraction of fluorescence events from the background[27]. Moreover, an optimal detector should offer high temporal resolution in order to accurately track the dynamic evolution of the system under investigation.
These features responds to technical parameters: the quantum efficiency, which determines how effectively incoming photons are converted into detectable electrons; the readout noise, which sets a lower limit on the smallest measurable signal; the frame rate which constrains the temporal resolution; and dynamic range, which influences the detector's ability to simultaneously capture dim and bright features within the same image.
The light signal produced by fluorescence emission is converted by each pixel of the sensor into an electrical charge proportional to the intensity of the incoming light. The charge accumulated in the pixels is then amplified and converted into a digital signal by an analog-to-digital converter (ADC).
The most common detectors used in fluorescence imaging are Charge-Coupled Device (CCD) and Complementary Metal-Oxide-Semiconductor (CMOS) sensors [28].
In CCD detectors, each pixel acts as a potential well, and the stored charge is transferred pixel by pixel toward a readout register in a synchronized manner. In contrast, CMOS

detectors use a photodiode for each pixel, with individual amplifiers and readout circuitry, enabling parallel readout of many pixels simultaneously.

CCD sensors are characterized by extremely low readout noise due to their amplification process, but they are limited in terms of frame rate and dynamic range. Modern CMOS sensors, while having slightly higher readout noise compared to CCDs, offer much faster frame rates, larger dynamic range, and wider fields of view, making them particularly suitable for fast, high-resolution fluorescence imaging.

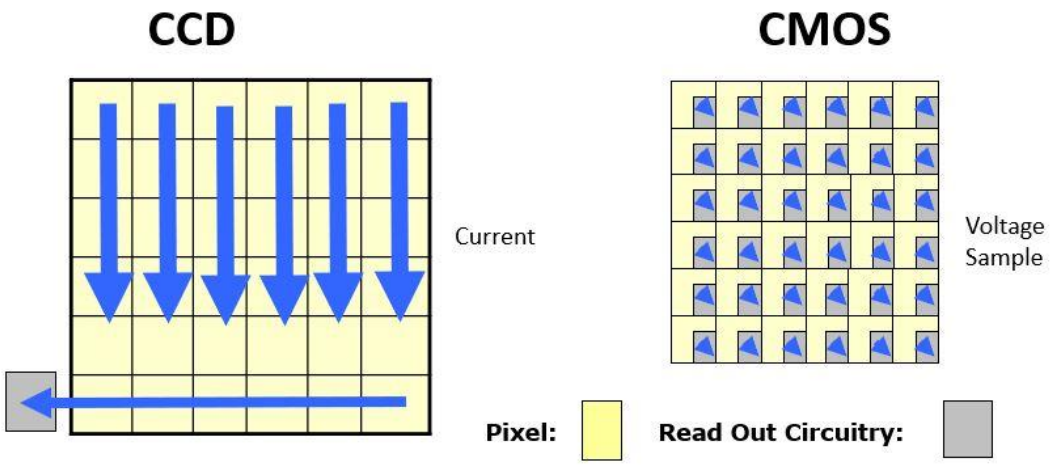

Figure 2-16:Illustration of the readout mechanism of a CCD camera and a CMOS camera. From https://astropills.it/il-binning-in-astrofotografia/

2.4 Bibliography

[1] Gerd Binnig. *Atomic force microscopy*. **Physical Review Letters**, 56:930–933, 1986.

[2] ME Taylor. *Dynamics of piezoelectric tube scanners for scanning probe microscopy*. **Review of Scientific Instruments**, 64(1):154–158, 1993.

[3] Georg Schitter, Karl J. Åström, Barry E. DeMartini, Philipp J. Thurner, Kimberly L. Turner, and Paul K. Hansma. *Design and modeling of a high-speed AFM-scanner*. **IEEE Transactions on Control Systems Technology**, 15(5):906–915, 2007.

[4] Allison B. Churnside, Ruby May A. Sullan, Duc M. Nguyen, Sara O. Case, Matthew S. Bull, Gavin M. King, and Thomas T. Perkins. *Routine and timely sub-piconewton force stability and precision for biological applications of atomic force microscopy*. **Nano Letters**, 12(7):3557–3561, 2012.

[5] Sader, J.E., J.W. Chon, and P. Mulvaney, Calibration of rectangular atomic force microscope cantilevers. Review of scientific instruments, 1999. **70**(10): p. 3967-3969.

[6] Hutter, J.L. and J. Bechhoefer, Calibration of atomic-force microscope tips. Review of scientific instruments, 1993. **64**(7): p. 1868-1873.

[7] Bhushan, B., Springer handbook of nanotechnology. 2017: Springer.

[8] Rigato, A., Characterization of cell mechanics with atomic force microscopy: Mechanical mapping and high-speed microrheology. 2015, Aix-Marseille.

[9] Xiangying Deng, Fang Xiong, Xiayu Li, Bo Xiang, Zheng Li, Xu Wu, Can Guo, Xiaoling Li, Yong Li, Guiyuan Li, et al. Application of atomic force microscopy in cancer research. *Journal of nanobiotechnology*, 16(1):1–15,2018.

[10] Andres F Oberhauser, Paul K Hansma, Mariano Carrion-Vazquez, andJulio M Fernandez. Stepwise unfolding of titin under force-clamp atomicforce microscopy. *Proceedings of the National Academy of Sciences*, 98(2):468–472, 2001.

[11] Yue Chan, Richard G Haverkamp, and James M Hill. Force-extension formula for the worm-like chain model from a variational principle. *Journalof theoretical biology*, 262(3):498–504, 2010.

[12] Madeleine B Borgia, Alessandro Borgia, Robert B Best, Annette Steward,Daniel Nettels, Bengt Wunderlich, Benjamin Schuler, and Jane Clarke.Single-molecule fluorescence reveals sequence-specific misfolding inmultidomain proteins. *Nature*, 474(7353):662–665, 2011.

[13] Hans-J¨urgen Butt, Brunero Cappella, and Michael Kappl. Force measurements with the atomic force microscope: Technique, interpretation and applications. *Surface science reports*, 59(1-6):1–152, 2005.

[14] Hans-J¨urgen Butt, Brunero Cappella, and Michael Kappl. Force measurements with the atomic force microscope: Technique, interpretation and applications. *Surface science reports*, 59(1-6):1–152, 2005.

[15] Joanna Zem la, Joanna Danilkiewicz, Barbara Orzechowska, Joanna Pabijan, Sara Seweryn, and Ma lgorzata Lekka. Atomic force microscopy as a tool for assessing the cellular elasticity and adhesiveness to identify cancer cells and tissues. In *Seminars in cell & developmental biology*, volume 73, pages 115–124. Elsevier, 2018.

[16] Gerd Binnig. Atomic force microscopye. *Phys. Rev. Lett.*, 12:930, 1986.

[17] Besner, Sebastien, et al. "In vivo Brillouin analysis of the aging crystalline lens." *Investigative ophthalmology & visual science* 57.13 (2016): 5093-5100.

[18] Bailey, Michelle, et al. "Viscoelastic properties of biopolymer hydrogels determined by Brillouin spectroscopy: A probe of tissue micromechanics." *Science advances* 6.44 (2020): eabc1937.

[19] Bottani, Carlo E., and Daniele Fioretto. "Brillouin scattering of phonons in complex materials." *Advances in Physics: X* 3.1 (2018): 1467281.

[20] Abbe, E., Beiträge zur Theorie des Mikroskops und der mikroskopischen Wahrnehmung. Archiv für mikroskopische Anatomie, 1873. **9**(1): p. 413-468.

[21] Sabatini, Bernardo L., Thomas G. Oertner, and Karel Svoboda. "The life cycle of Ca2+ ions in dendritic spines." *Neuron* 33.3 (2002): 439-452.

[22] Lai, Yinzhi, Ke Cheng, and William Kisaalita. "Three dimensional neuronal cell cultures more accurately model voltage gated calcium channel functionality in freshly dissected nerve tissue." (2012): e45074.

[23] Takahashi, Akiyuki, et al. "Measurement of intracellular calcium." *Physiological reviews* 79.4 (1999): 1089-1125.

[24] Ridgway, E. B., and C. C. Ashley. "Calcium transients in single muscle fibers." *Biochemical and biophysical research communications* 29.2 (1967): 229-234.

[25] McMillan, T. J., et al. "Cellular effects of long wavelength UV light (UVA) in mammalian cells." Journal of Pharmacy and Pharmacology 60.8 (2008): 969-976.

[26] Paredes, R. Madelaine, et al. "Chemical calcium indicators." Methods 46.3 (2008): 143-151.

[27] Pawley, James, ed. *Handbook of biological confocal microscopy*. Vol. 236. Springer Science & Business Media, 2006.

[28] Lambert, Talley J., and Jennifer C. Waters. "Assessing camera performance for quantitative microscopy." *Methods in cell biology* 123 (2014): 35-53.

[29] Palombo, Francesca, and Daniele Fioretto. "Brillouin light scattering: applications in biomedical sciences." *Chemical reviews* 119.13 (2019): 7833-7847.

[30] Palombo, Francesca, and Daniele Fioretto. "Brillouin light scattering: applications in biomedical sciences." *Chemical reviews* 119.13 (2019): 7833-7847.

3

Interaction of α-synuclein with a Biomimetic Membrane

3.1 Introduction

The plasma membrane is a dynamic and essential cellular structure composed primarily of lipids and proteins. It functions as a barrier between the intracellular and extracellular environments, regulating nutrient transport and biomolecular interactions [1].

Together with the cytoskeleton, plasma membrane plays a fundamental in cell mechanics regulating cell morphology and preserving its integrity under mechanical stresses. Indeed, lipids form the structural scaffold of the membrane, assembling into a bilayer interspersed with proteins, sterols, and other biomolecules.

The lipidic component of the membrane is organized in a double layer of lipid molecules organized in two different leaflets called “lipid bilayer”. In each leaflet, lipids are oriented such that their polar head groups face the aqueous environment, while their hydrophobic tails are directed toward the bilayer interior.

In 1972, Singer and Nicolson [2] proposed the first modern model describing the composition, properties, and organization of the cell membrane based on the physicochemical nature of its constituents. According to their hypothesis, the lipid component, arranged in a bilayer, is characterized by substantial homogeneity and fluidity, within which proteins are free to diffuse as if embedded in a fluid.

For this reason, this description became known as the 'fluid mosaic model.' In the early 21st century, however, several studies highlighted the greater structural complexity of the membrane [3, 4, 5]. The membrane contains lipid and protein aggregates that make

the diffusive dynamics of membrane proteins more complex. Moreover, its components interact with the cell interior through the cytoskeleton and with the extracellular environment via specific membrane proteins, such as glycoproteins.

The diffusion of proteins across the membrane is often guided by the biological processes in which they are involved, many of which do not occur through a single isolated molecule but require the formation of macromolecular assemblies composed of multiple proteins. For this reason, such molecules tend to form clusters within the membrane, enabling interactions that may be mediated by linker molecules or by the cytoskeleton [6]. In addition, certain lipid species can segregate into microdomains a few hundred nanometers in size, called 'lipid rafts'. These structures differ from the surrounding regions in composition, morphology, and mechanical properties [7, 8]. Lipid rafts can stabilize and form extended membrane regions that participate in protein–protein or protein–lipid interactions [9].

The lipid composition is diverse and depends to the cell type, environmental factors and cellular needs. In general, it is dominated by glycerophospholipids, sphingolipids, and sterols [10-12]

Membrane Lipids

Phospholipids

Phospholipids represent the predominant lipid component of eukaryotic cell membranes. Their chemical structure is characterized by a glycerol backbone esterified with two long fatty acid chains and a phosphate group, which is further esterified through an alcohol forming the polar head. The most abundant species in this family is phosphatidylcholine (PC), followed by phosphatidylethanolamine (PE) and phosphatidylserine (PS). These phospholipids exhibit variability in their fatty acid chains, which may be saturated or unsaturated and of different lengths (typically between 14 and 24 carbon atoms).

Sphingolipids

Sphingolipids are based on a sphingosine backbone and are generally composed of ceramide fatty acids, most often saturated. This family includes both phosphosphingolipids and glycosphingolipids. Phosphosphingolipids are characterized by a phosphate group esterified with an alcohol, the most abundant being sphingomyelin

(SM), whose polar head is formed by phosphocholine. Glycosphingolipids, instead, exhibit a more complex structure, in which the ceramide is linked to an oligosaccharide. The carbohydrate moiety, being hydrophilic, protrudes from the membrane and may act as a receptor. In some cases, the head group also contains sialic acid residues. Gangliosides are a representative subgroup of glycosphingolipids, predominantly found in the nervous system, with GM1 being a well-known example.

Sterols

Sterols are characterized by a smaller size compared to the before mentioned lipid families and by a pronounced hydrophobicity. Their structure is composed of a sterol nucleus, terminated on one side by an alkyl chain and on the other by a hydroxyl group. Cholesterol is the most common sterol in biological membranes, and its length approximately matches the thickness of a single membrane leaflet. In membranes, cholesterol is typically present in its non-esterified form, where it plays a fundamental role in modulating membrane fluidity and mechanical stability [13].

The cell membrane exhibits an asymmetric structure, with the lipid composition of the inner leaflet differing from that of the outer leaflet [14]. This asymmetry allows the cytosolic and extracellular sides to perform distinct functions depending on the biological processes in which they are involved. Moreover, it enables modulation of membrane curvature.

Phosphatidylcholine and sphingolipids are more abundant in the outer leaflet, whereas phosphatidylserine and phosphatidylethanolamine are primarily enriched in the inner leaflet. Cholesterol, although more than 70% is localized in the cytosolic side, plays a crucial role in the lateral organization of lipids in the extracellular leaflet.

Membrane asymmetry between the inner and outer leaflets is maintained by the amphiphilic nature of lipid molecules, which makes the translocation of lipids from one leaflet to the other -known as 'flip-flop'-energetically unfavorable [*15*].

Lipids Lateral Organization

Lipids in the membrane can laterally organize into different thermotropic phases, each characterized by distinct structural properties such as thickness, rigidity, and mobility [*16*]. The phase adopted by a lipid species within the membrane depends on several parameters, including the degree of unsaturation of the hydrocarbon chains, their length,

and temperature. Lipids with long, saturated acyl chains can laterally pack in a way that maximizes chain–chain interactions, thereby forming a more ordered intermolecular structure. Their mobility is reduced, with a measured diffusion coefficient (D) on the order of 10^{-3} $\mu m^2/s$. This configuration is referred to as the "solid-ordered phase" (S_o) or "gel phase". Conversely, lipids with shorter and/or unsaturated chains exhibit less efficient chain–chain interactions, leading to a more disordered arrangement known as the "liquid-disordered phase" (L_d) or "fluid phase", in which lipids are freer to diffuse. In this case, the diffusion coefficient (D) is on the order of 1 $\mu m^2/s$. The gel phase can only form below a certain temperature, known as the transition or melting temperature (T_m); above this temperature, the lipids are found in the fluid phase. The T_m value depends on both the chain length and the degree of unsaturation.

Lipid species with short and highly unsaturated chains display a transition temperature (T_m) well below physiological temperature. Conversely, lipids with long and saturated chains have a T_m close to or above physiological temperature. Cholesterol plays a crucial role as a fluidity regulator in cellular membranes. According to the Huang and Feigenson 'umbrella model [17], cholesterol -whose length is comparable to the thickness of a single membrane leaflet- intercalates between the lipid tails. As schematically illustrated in *figure 3-1 [47]*, in the case of lipids in the So phase, cholesterol disrupts the tight packing of acyl chains, thereby increasing membrane fluidity. In contrast, in the case of lipids in the Ld phase, cholesterol promotes conformational ordering and decreases fluidity due to enhanced crowding within the hydrophobic matrix. Overall, the presence of cholesterol gives rise to a hybrid phase between So and Ld, termed the 'liquid-ordered phase' (Lo). By doing so, cholesterol modulates the mechanical properties of the membrane, even under temperature variations, preventing membrane fluidity from reaching excessively low or high levels that could compromise the biological functionality of the membrane.

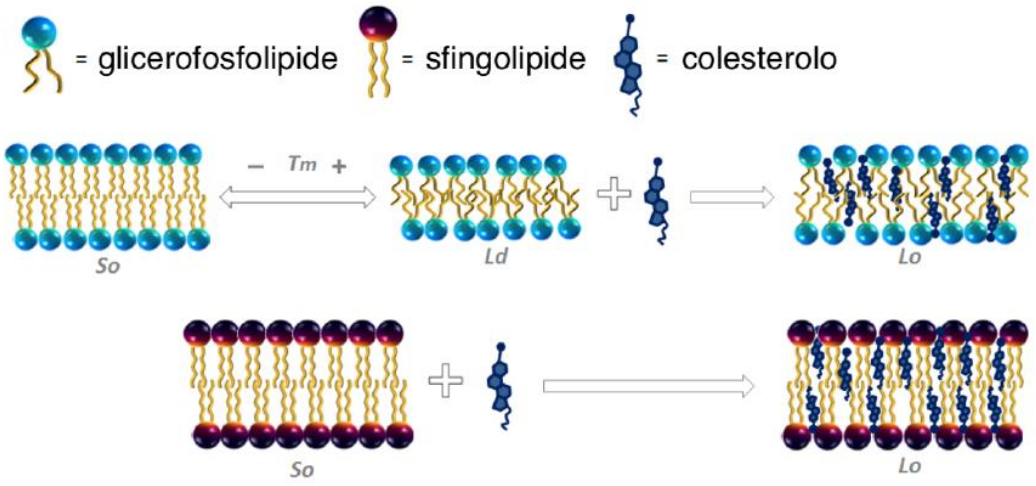

Figure 3-1: Schematic illustration showing the different thermotropic phases of membrane lipids and the role of cholesterol in the formation of the liquid-ordered hybrid phase, according to the 'umbrella model'.

Biomimetic Systems

Investigating the properties of the cellular membrane at the nanoscale, together with the biological processes in which it participates, represents an exceptional challenge. Even when focusing solely on its lipid component, the membrane exhibits a remarkably rich and temporally dynamic composition.

This complexity underlies their functional versatility in modulating cellular processes [18]. For this reason, it is essential to develop simplified model systems that reproduce selected characteristics of biogenic membranes, allowing these features to be isolated and investigated.

Several synthetic lipid systems have been developed to investigate the physicochemical properties of the cells lipid structures. In this thesis, only lipid systems such as liposomes and supported lipid bilayers (SLBs) formed via vesicle fusion will be discussed.

These systems are widely used to mimic biological membranes in research and biotechnological applications [19,20].

The assembly of a lipid bilayer via vesicle fusion is achieved using liposomes, which are lipid vesicles generated by sonication or extrusion of large lipid aggregates, referred to as multilamellar vesicles (MLVs) [24]. A liposome suspension is deposited onto a hydrophilic substrate, where vesicle adsorption triggers progressive deformation until rupture, ultimately resulting in fusion and bilayer formation on the supporting surface.

The formation of a lipid bilayer through vesicle fusion originates from liposomes, which are lipid vesicles obtained by sonicating or extruding large lipid aggregates known as

multilamellar vesicles (MLVs) [24]. A suspension of liposomes is deposited onto a hydrophilic surface. The adsorption of the vesicles onto the surface induces their progressive deformation until rupture, leading to their fusion and the subsequent formation of a bilayer on the substrate.

Incubation time, substrate type, and solvent are selected to promote vesicle adsorption and fusion, and their choice depends on the specific lipid mixture under investigation. Compared to the cellular membrane, the reduced complexity of the lipid bilayer promotes much more pronounced phase separation among lipid species.

This approach allows for a thermodynamic characterization of the system through the construction of phase diagrams, which describe the type and number of phases present as a function of both composition and temperature.

From Gibbs' phase rule for thermodynamic systems [21], we know that the number of independent thermodynamic variables (such as temperature, pressure, and lipid composition) is given by the number of components multiplied by two, minus the number of phases present: $F = C - P + 2$. Consequently, for a binary system with variable temperature and pressure but fixed composition, $F = 2$, and at most two coexisting phases can occur. In contrast, for a ternary system, up to three phases may coexist. If the system pressure is also fixed, then $F = 1$, and in the case of a binary system, three phases can coexist simultaneously at a single temperature, the so-called 'triple point.'

A system composed of two lipid species is typically represented by a diagram plotting temperature as a function of the mole fraction of the lipids, as shown in *figure 3-2a [48]*. Considering species A with a high T_m and species B with a low T_m, at low temperatures and for compositions not heavily biased toward one lipid, two coexisting gel phases are observed. Upon increasing the temperature, a coexistence of the gel phase of species A with the fluid phase of species B appears. At temperatures above the melting temperature of species A, the system becomes a uniform lipid mixture.

In contrast, a ternary system is represented by a triangular phase diagram (*figure 3-2b [48]*), where each side corresponds to the mole fraction of one species. The lines within the triangle represent phase transition boundaries at a fixed temperature. Thus, the composition and temperature together define the thermodynamic phase of the system.

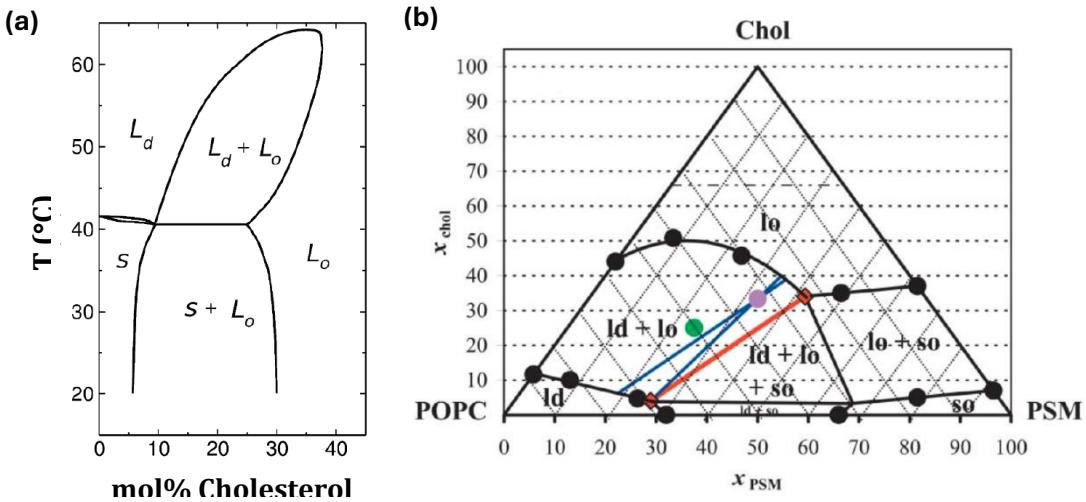

Figure 3-2: (a) Phase diagram of a binary DPPC–cholesterol system.(b) Phase diagram of a ternary lipid mixture composed of PC, SM, and cholesterol.

SLBs enable investigation of membrane-associated phenomena including protein–lipid interactions, drug permeability, and nanoparticle binding [22,23]. The physical phase of the membrane (gel, fluid, or liquid-ordered) critically influences these processes and is often tuned to match specific experimental goals [24–26].

In this thesis, we present the characterization of a SLB that mimics the composition of the outer leaflet of the neuronal membrane, with the aim of investigating the effects of α-synuclein on its mechanical stability.

Mechanical Properties of Cytoplasmatic Membrane

Membrane mechanics play a key role in modulating interactions with extracellular molecules and in numerous physiological and pathological processes [27]. However, the complexity of native membranes necessitates simplified model systems to isolate specific lipid behaviours. Among these, SLBs offer a robust and reproducible platform, often prepared via vesicle fusion [28-29]. When combined with Atomic Force Microscopy (AFM), SLBs enable nanoscale characterization of membrane structure and mechanics.

Many cellular metabolic processes occur through remodelling of the plasma membrane. Membrane deformations are at the basis of endocytosis, exocytosis, and cell division. Moreover, this structure regulates interactions with molecules and other extracellular complexes such as proteins, nanoparticles, and vesicles. The lipid environment of the membrane is in fact crucial for the proper activity and organization of membrane

proteins. For this reason, the membrane is a highly complex and dynamic structure, capable of adjusting its properties according to cellular needs.

During these processes, membrane mechanics play a fundamental role. Furthermore, several pathologies are associated with dysregulation of the mechanical properties of the membrane. In particular, in this thesis we focus on how peptides involved in neurodegenerative diseases — such as Alzheimer's and Parkinson's — interact with the cell membrane and how they affect its mechanical properties. Correlating these properties with membrane composition and topology is therefore essential to understand cellular processes and related pathologies.

The study of model membranes, such as Supported Lipid Bilayers (SLBs), allows one to isolate the lipid component and obtain a planar system, easier to analyze with techniques such as Atomic Force Microscopy (AFM).

AFM, thanks to its versatility in switching from imaging to force spectroscopy, provides high-resolution information on the sample topography and allows correlating this information with the mechanical properties of the membrane.

Mechanical properties are typically assessed using Dynamic Force Spectroscopy (DFS), which measures the force required to rupture the bilayer (breakthrough force) [30]. However, this method depends on the loading rate and operates far from equilibrium, requiring measurements at varying rates for reliable interpretation, including very low ones, difficult to achieve with AFM.

An alternative is Force Clamp Spectroscopy (FCS), which probes bilayer mechanics under equilibrium by determining the average energy required to separate lipid molecules, an intrinsic, rate-independent parameter. FCS was proposed by Butt and Franz [31] and has since been applied to monophasic bilayers [32-33], but not yet to multicomponent systems. Advances in AFM technology, particularly closed-loop feedback, allow high spatial resolution and stable force control, enabling combined imaging and mechanical probing of specific submembrane regions [34].

Mechanical Characterization through The Dynamic Force Spectroscopy

The more consolidated AFM-based method to mechanically characterize a SLB is the Dynamic Force Spectroscopy (DFS) [30]. The DFS method is based on the analysis of a force-distance curve.

Figure 3-3 shows a typical force–distance curve of the piezo during indentation of a supported lipid bilayer. In the approach curve, after the contact point is reached, the force increases monotonically until a critical value is attained, at which a sudden drop in

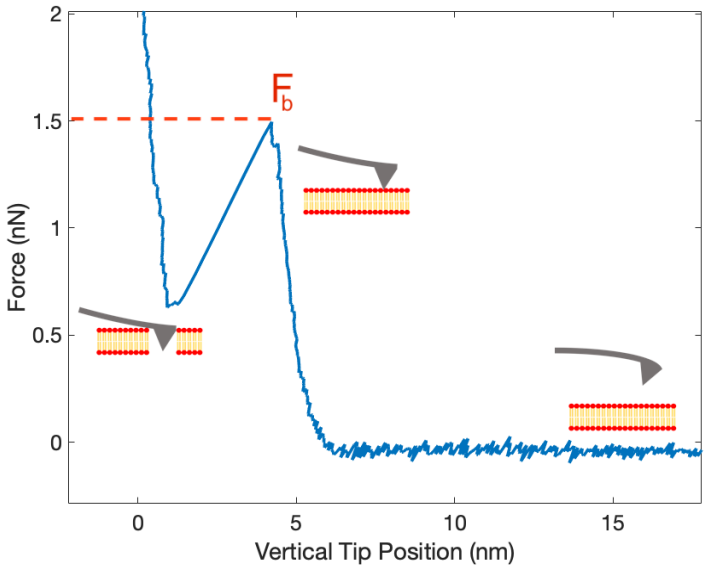

Figure 3-3: Experimental force–distance curve acquired on a lipid bilayer, showing the characteristic breakthrough event.

force is

observed. This event is followed by a resumption of the monotonic increase. The force at which this discontinuity occurs is referred to as the breakthrough force (Fb), corresponding to the force required to rupture the membrane and allow the tip to penetrate into the bilayer. Once inside the bilayer, the tip interacts with the rigid substrate, as reflected in the subsequent portion of the curve.

This mode of force spectroscopy is referred to as 'force ramp' or Dynamic Force Spectroscopy (DFS) [35]. The breakthrough force is related to the chemical composition of the membrane lipids [36] and is strongly dependent on the physicochemical environment, including temperature, pH, and ionic strength [37, 38].

For this reason, this quantity is particularly useful for investigating the mechanical stability of the membrane. The bilayer rupture phenomenon is statistical in nature, resulting from thermal energy fluctuations within the system. Such fluctuations can locally lead to the dissociation of adjacent lipid molecules composing the bilayer. For this

to occur, it is necessary to overcome an energy barrier associated with the interaction energy between lipids, which separates the energetic states of associated and dissociated lipids. Therefore, bilayer rupture can be considered as a two-state activation phenomenon described by the Arrhenius law:

$$k(t) = Aexp\left(-\frac{\Delta E(t)}{k_B T}\right) \quad (1)$$

The dissociation rate between adjacent lipids, k(t) is therefore proportional to an exponential term that depends on the ratio between the height of the potential barrier $\Delta \mathrm{E(t)}$ and the system's thermal energy at equilibrium, $\mathrm{k_B T}$. The proportionality constant A is defined as the resonance frequency of the AFM cantilever. When an external force is applied, the potential barrier is lowered, consequently increasing the dissociation rate, i.e., decreasing the average lifetime of the lipid-lipid association [40, 5].

In the case of DFS, the rate at which the external force varies (the loading rate) changes linearly with the cantilever velocity:

$$\frac{dF}{dt} = k_s v \quad (2)$$

where $\mathrm{k_s}$ is the spring constant of the AFM cantilever. From these observations, it is possible to demonstrate that $\mathrm{F_b}$ depends on the loading rate.

If we consider N_0 identical experiments, in which N_0 AFM cantilevers are in contact with intact membranes, after a time interval dt, the number of membranes in which a rupture event has occurred is d. Meanwhile, N will be the number of intact membranes. Considering that dN will be proportional to the dissociation rate k(t), we have the following relation: $\mathrm{dN = -k(t)Ndt}$. Dividing by $\mathrm{N_0}$, we obtain an equation for the probability of the rupture event occurring:

$$\frac{dP(t)}{dt} = -k(t)P(t) \quad (3)$$

From equation (3) we have:

$$\ln\big(P(t)\big) = -A\int_{t_s}^{t} \exp\left(-\frac{\Delta E(\tau)}{k_B T}\right) d\,\tau \quad (4)$$

where ts is the instant when the tip comes into contact with the sample. From relation (2.8), assuming a constant v, we can express the force as $F = k_s v t$ and perform the change of variable within the integral equation:

$$\ln\big(P(t)\big) = -\frac{A}{k_s v}\int_{F_s}^{F} \exp\left(-\frac{\Delta E(F')}{k_B T}\right) dF' \quad (5)$$

DFS experiments show that the distribution of breakthrough forces is rather narrow; consequently, $\Delta F_b/F_b \ll 1$. Therefore, there is little discrepancy between the mean of the distribution and the force $\tilde{F}$ such that $\mathrm{P}\big(\tilde{\mathrm{F}}\big) = 1/2$. We can then $\ln P(F_b) = \ln 0.5 = -0.693$ and write:

$$v = \frac{A}{0.693 k_s}\int_{F_s}^{F_b} \exp\left(-\frac{\Delta E(F')}{k_B T}\right) dF' \quad (6)$$

From equation (6), we can immediately observe the dependence of $\mathrm{F_b}$ on the loading rate: the integral function is monotonically increasing, so v is a monotonic function of $\mathrm{F_b}$ and vice versa; that is, the higher the loading rate, the higher the average breakthrough force. This is due to the fact that, if the intensity of the external force varies slowly, there is a greater probability per unit time that the rupture will occur at a given force value.
By differentiating equation (6), we obtain:

$$\Delta E(F_b) = -k_B T \ln\left(\frac{0.693 k_s}{A}\frac{dv}{dF_b}\right) \quad (7)$$

From this, the dependence of the potential barrier on $\mathrm{F_b}$ as a function of v is obtained. Assuming a logarithmic behavior of F_b with respect to the loading rate [44]:

$$F_b = a + b\log(v) \quad (8)$$

Combining (7) with (8), we obtain:

$$\Delta E(F_b) = -k_B T \ln\left(\frac{1.6 k_s}{Ab} v\right) = k_B T\left[2.3\left(\frac{a - F_b}{b}\right) ln\left(\frac{1.6 k_s}{Ab}\right)\right] \quad (9)$$

By extrapolation, we can calculate ΔE at equilibrium, that is, in the absence of external forces:

$$\Delta E_0 = k_B T\left[\left(\frac{2.3a}{b}\right) - ln\left\{\left(\frac{1.6 k_s}{Ab}\right\}\right)\right] \quad (10).$$

By studying the variation of $\mathrm{F_b}$ as a function of the loading rate, it is therefore possible to experimentally determine the energy barrier of the process at equilibrium. However, the range of loading rates that can be applied using AFM is limited, particularly at low loading rates. For this reason, the extrapolation of the equilibrium value is affected by a non-negligible uncertainty. To have access to a wider range of loading rates, it would be

necessary to use instruments such as Optical Tweezers [40, 41], which allow the application of mechanical stimuli with intensities even on the order of pN in an extremely gradual and controlled manner.

Mechanical Properties through the Force Clamp Spectroscopy

An alternative method for measuring the interaction energy between membrane lipids using AFM is the Force Clamp Spectroscopy (FCS) introduced for the first time by Prof. Julio Fernandez's group (Columbia University, USA) for studying protein unfolding [42]. In this thesis work, we aimed to extend this approach to the study of supported lipid bilayers, a system still scarcely explored through the Force Clamp technique [43, 44].

This force-spectroscopy method focuses on investigating the bilayer rupture process following the application of a constant force -the clamp force **Fc**- whose magnitude is lower than the breakthrough force.

The time trace of the piezo's vertical position *z* (figure 3-4) shows an initial phase in which the vertical position rapidly decreases in order to make contact with the membrane and reach the desired value of **Fc**. In the subsequent portion of the curve, a plateau is observed, interrupted by a sudden step. This step corresponds to the breakthrough event, and its height is related to the depth to which the tip penetrates into the membrane.

The following plateau reflects the new equilibrium state that is established. Finally, the upward movement of the tip is observed, marking the moment when contact with the membrane is released.

After a certain period of time, the membrane may yield under the action of the tip; a spike will indicate a sudden, transient drop in the cantilever deflection and therefore in the interaction force associated with the tip's penetration through the membrane.

The feedback system then restores the set conditions. As mentioned earlier, in the absence of external forces the dissociation between lipids can be described as an activation process that follows the Arrhenius law (2.7). In the presence of an external force, the potential barrier ΔE_0 decreases and, with it, the average lifetime of the lipid–lipid association.

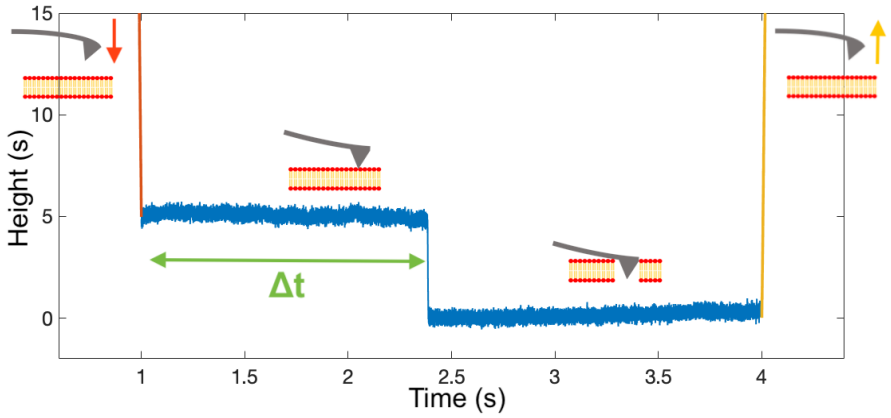

Figure 3-4: Experimental force-clamp curve plotted as height versus time.

For a constant applied force, the energetic contribution of that force can be written as $E_{\text{ext}} = -\Delta x\, F_c$.

$\Delta x$is a length-scale parameter that can be interpreted as the minimum average distance required to separate two lipid molecules enough to eliminate their mutual interaction. By analogy with chemical transition-state theory, $\Delta x$is called the reaction coordinate.

E_{ext} therefore corresponds to the work that the AFM cantilever must perform to pull the lipids apart to a distance where they no longer interact, thus causing membrane rupture.

We can therefore replace the Arrhenius law with the Arrhenius–Bell law:

$$\alpha(F_c) = Aexp\left(-\frac{\Delta E_0 - \Delta x F_c}{k_B T}\right) \quad (11)$$

From which we obtain a linear relationship for ln α:

$$ln(\alpha) = ln\left(\alpha_0 + \frac{\Delta x F_c}{k_B T}\right),\ \alpha_0 = Ae^{-\frac{\Delta E_0}{k_B T}} \quad (12)$$

Where α_0 lipid dissociation rate at the equilibrium.

Experimentally, α is measured as a function of $F_c < F_b$. By fitting equation (12) to the experimental data, both ΔE_0 and Δx can be determined. Through the Force Clamp technique, it is therefore possible not only to determine the activation energy of the process, but also to estimate the maximum of the energy barrier along the reaction coordinate.

Furthermore, compared to DFS, it is not necessary to study the breakthrough force as a function of the loading rate, thus avoiding the experimental limitations involved in determining F_b, especially at low velocities. In this case, it is sufficient to determine the value of F_b at a single loading rate and use that value as the upper limit for the clamp forces employed to study the dissociation rate.

3.2 Materials and methods

The following materials were used for film preparation:

- Ethanol (≥ 99.5%) and methanol (≥ 99.9%) of analytical grade, purchased from Sigma Aldrich, and used without further purification.
- 1,2-Dioleoyl-sn-glycero-3-phosphatidylcholine (DOPC, 18:1), purchased from Avanti Polar Lipids.
- Sphingomyelin (SM, from porcine brain) was purchased from Avanti Polar Lipids.
- Ganglioside GM1 (from ovine brain) from Avanti Polar Lipids.
- Cholesterol (Chol) were obtained from Avanti Polar Lipids.
- Ultrapure water (Milli-Q®), deionized and purified with a Millipore purification system to a resistivity of 18.2 MΩ·cm, was used in all experiments.

FCS Analysis Software

The rupture event of the bilayer during a clamp measurement appears in the plot of the piezo position versus time as a step-like signal. The program developed for the analysis of Force Clamp curves makes it possible to detect the time at which this step occurs and to quantify its amplitude, which is related to the penetration depth Δz of the tip into the sample.The software reads the curve data and applies a smoothing procedure using a Savitzky–Golay filter. It then determines the maximum value of the derivative over a set of points belonging to the initial plateau of the curve; this value is used as a reference to identify the set of points that constitute the descending step. Consecutive points whose derivative exceeds, in absolute value, the reference threshold are included in the series

of points forming the step. The time coordinate of the first point in this series indicates the moment at which the rupture event occurs, while the difference between the vertical coordinates of the first and last point in the series yields the amplitude of the step.
The program allows control over several parameters, such as the size of the window used to compute the maximum derivative on the plateau, the minimum number of points whose derivative must exceed the threshold in order to be classified as part of the step, and a multiplicative factor applied to the derivative threshold to adjust it according to the noise level in the signal. By tuning these parameters, it is possible to optimize the identification of the step.

Liposome Preparation

As a first step, each lipid species, initially provided in lyophilized form, was dissolved in a volatile organic solvent mixture of chloroform/methanol (2:1, v/v). The lipid mixture employed mimics the composition of the outer leaflet of the neuronal membrane, characterized by the presence of ganglioside GM1. The other components are 1,2-dioleoyl-sn-glycero-3-phosphocholine (DOPC), sphingomyelin (SM, $T_m \approx 38$ °C), and cholesterol. The molar ratio of the lipids is DOPC:SM:GM1:Chol = 63:31:5:1.
The individual lipid stock solutions were mixed in a glass cuvette in proportions chosen to obtain the desired lipid composition. The solvent was then evaporated, first under a gentle nitrogen stream to accelerate the process and subsequently under vacuum for twelve hours to remove any residual traces of solvent. After this step, a homogeneous lipid film adhered to the walls of the cuvette.

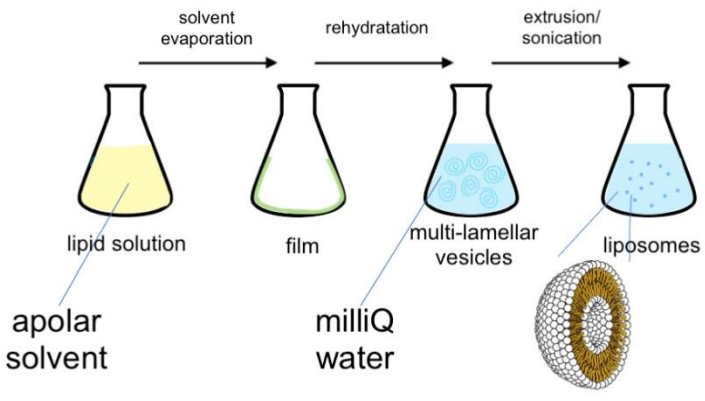

Figure 3-5: Schematic illustration of the liposome preparation process.

The film was rehydrated with Milli-Q® water. After hydration, the suspension was incubated for 15 minutes, during which the lipids self-assembled into large multilamellar aggregates ranging in size from hundreds of nanometers to several micrometers.

To obtain liposomes, i.e., unilamellar vesicles with diameters of ~100 nm or smaller, the lipid suspension was extruded twenty-five times through a polycarbonate membrane filter with 100 nm pore size (*figure 3-5*).
For lipid mixtures containing components with phase transition temperatures (T_m) above room temperature, both the film preparation and extrusion steps were carried out at 60 °C. In this case, the cuvette was immersed in pre-heated Milli-Q® water during lipid mixing, and the extruder was placed on a heating plate set at 60 °C during extrusion.

SLB preparation

The extruded lipid solution was diluted to a final concentration of 0.1 mg/mL, which was experimentally determined to be optimal for bilayer formation. The mica substrate was glued to a 1 cm metal disc using epoxy adhesive, enabling its placement on the microscope sample holder. Prior to use, the mica was freshly cleaved to produce a clean, hydrophilic surface exposing OH^- groups (figure 3-6).

At this stage, a 40 µL droplet of the lipid solution was deposited onto the substrate, followed by the addition of 10 µL of $CaCl_2$ to promote vesicle fusion. The sample was then incubated in a humid chamber for 10 minutes at room temperature.
For lipid mixtures containing species with a T_m higher than room temperature, after the 10-minute incubation the humid chamber containing the sample was transferred to an oven at 60 °C for 15 minutes. The sample was then cooled and further incubated for two hours. To remove unfused liposomes and excess Ca^{2+} ions, the droplet was rinsed with Milli-Q® water after incubation. Following rinsing, the sample was left for an additional 1.5 hours before analysis.

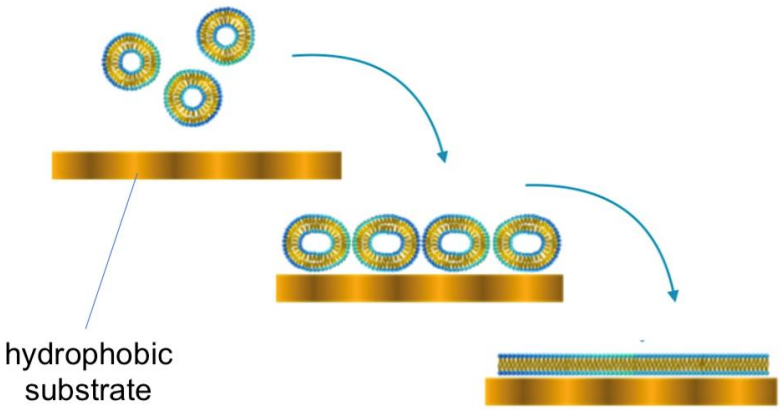

Figure 3-6 Illustration of liposome adsorption and fusion onto a hydrophobic substrate.

Incubation of the Model Membrane with α-Synuclein

After the incubation at 60°C for 15 minutes, the sample was cooled until reaching the room temperature. Then, a solution of α-syn oligomers is added to the lipid solution, in order to obtain the chosen final oligomer concentration.

I investigated two different concentration values: 200nM and 20 nM.

The mixed solution was incubated overnight and rinsed with Milli-Q® water after incubation, following the same procedure described above to obtain the SLB.

This method allows the interaction between the membrane lipids and the pathological oligomers without changing the incubation time and without alterations of the SLB state with the addition of the oligomeric solution after the incubation.

3.3 Results

Morphological Characterization

For each sample analyzed, the morphology was first examined using AFM in QI mode, keeping the force setpoint at a value much lower than F_b in order to minimize perturbation of the sample and reduce the risk of damaging the microscope tip. For the

force spectroscopy measurements, only membranes with a homogeneous surface and free of unfused liposomes were selected.

AFM analysis also allows the thickness of the lipid bilayer to be evaluated. To this end, membranes intentionally containing holes were prepared (obtained by thoroughly rinsing the sample), so that the bilayer thickness could be determined by measuring the depth of these holes from the analysis of the image cross-section.

Morphological Characterization of the Biomimetic membrane

The composition of this lipid mixture, DOPC:SM:GM1:Chol 63:31:5:1, is the most complex among those analyzed, as it contains not only a sphingophospholipid with a high T_m(SM) and a glycerophospholipid with a low T_m(DOPC), but also the ganglioside (GM1), which is a characteristic component of the outer leaflet of neuronal membranes.

The lateral organization of the lipids in the mixture results in an $L_d - S_0$ phase separation. Sphingomyelin (SM) and GM1 segregate to form ordered domains, which are surrounded by the fluid phase composed of DOPC. Cholesterol is distributed into both the phases.

From the AFM images, the height difference between the two phases can be measured. The height histogram shows two peaks: the left peak corresponds to the disordered phase, which is lower, while the right peak corresponds to the ordered phase, which is higher.

From the difference in the positions of the two peaks, the height difference between the two phases can be calculated, which turns out to be equal to (2.1 ± 0.6) nm (Mean ± SD).

While, from the cross-section analysis of the images with holes the thickness obtained is (5.8 ± 0.4) nm (*figure 3-7*).

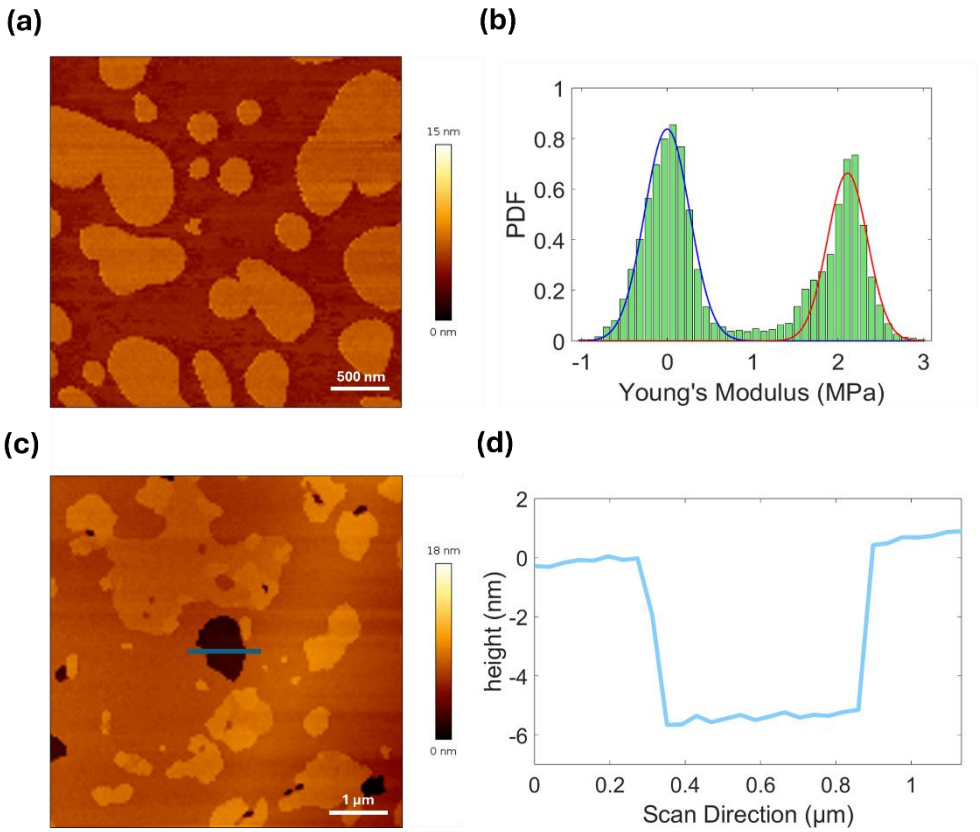

Figure 3-7: (a) AFM image of the biomimetic membrane.(b) Histogram of the height distribution of the biomimetic membrane.(c) Biomimetic membrane with a hole used to measure the Ld phase thickness. (d) Cross-section of the hole region of the membrane.

Morphological Characterization of the Biomimetic membrane incubated with alpha-syn

The QI investigation of the morphological variations induced by pathological α-synuclein oligomers followed the same experimental procedure used for the biomimetic membrane. At an oligomer concentration of 200 nM, the experimental results show the presence of defects in the membrane-particularly within the $L_d$phase, as illustrated in the *figure 3-8a*. At 20 nM (*figure 3-8b*), no significant morphological changes are visible in the QI images. These observations are in accordance with previous morphological investigations [45].

Nevertheless, the aim of this study is to assess the mechanical stability of the biomimetic membrane interacting with a more physiological low-concentraton of oligomer solution using the FCS method. For this reason, the FCS study of the SLB incubated with oligomers was made only at the concentration of 20nM.

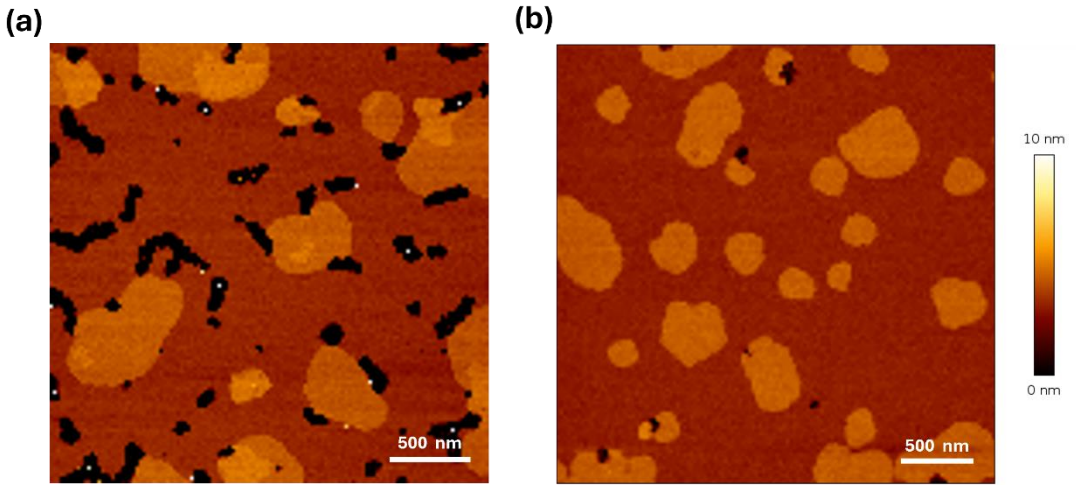

Figure 3-8: ***(a)*** *Biomimetic lipid bilayer incubated overnight with a 200 nM solution of α-synuclein oligomers.* ***(b)*** *Biomimetic lipid bilayer incubated overnight with a 20 nM solution of α-synuclein oligomers.*

FCS analysis

FCS analysis was performed on three membranes incubated with α-syn oligomers and on six control membranes, acquiring approximately 120 curves for each of four applied force values in every membrane phase.

To apply the Force Clamp method, a preliminary estimation of the breakthrough force F_b is required in order to select clamp forces lower than F_b, ensuring that the bilayer does not rupture before the applied force stabilizes at the chosen clamp value. However, an accurate determination of F_b is not necessary, since this quantity does not enter the equations used to calculate ΔE_0 and Δx.

Based on this consideration, and given that prolonged use of the AFM tip can compromise its performance, it was decided to acquire -for each sample- only a limited number of force ramps, still sufficient to estimate F_b and identify the range of forces to be used during the subsequent Force Clamp analysis.

Whenever possible, replacing the tip during the analysis of a single sample was also avoided in order to prevent measurement errors arising from changes in the tip's terminal radius (a parameter that can vary within the same batch of tips) and to avoid perturbing the sample during the disassembly and reassembly of the setup.

As noted above, F_b represents the maximum force that can be applied to the membrane during Force Clamp measurements. An experimental lower limit is also identified, since applying a force that is too small results in no detectable rupture event, even after several tens of seconds. This observation is consistent with reports in the literature [46].

For each force value, approximately 200 clamp curves were acquired. During the analysis, curves in which no membrane rupture event could be identified, as well as those exhibiting multiple rupture signals separated in time, were discarded. This procedure yielded, on average, about 100 curves per force value that satisfied the required criteria.

Once the clamp curves for each force value were acquired, they were analyzed using the custom software described above, in order to determine, for each curve, the time at which the rupture event occurred and the corresponding penetration depth.

The resulting data were plotted in a histogram, and an exponential fit of the distribution was performed, as predicted by the model described in the introductory chapters (*figure 3-8a*). From the fit, the mean of the distribution was obtained, corresponding to the average membrane rupture time at a given force value.

Finally, using equation:

$$\ln\ \alpha = \ln\ \alpha_0 + \frac{\Delta x F_c}{k_B T},\ \alpha_0 = A\, e^{\frac{\Delta E_0}{k_B T}}$$

to determine ΔE_0 and Δx, the rupture rate was plotted in a semi-logarithmic scale as a function of the clamp force. These data follow a linear trend, from whose linear fit the quantities of interest can be extracted, as shown in the *figure 3-8b*.

The analysis of the mechanical properties using the Force Clamp technique was performed on both the Ld and So phases.

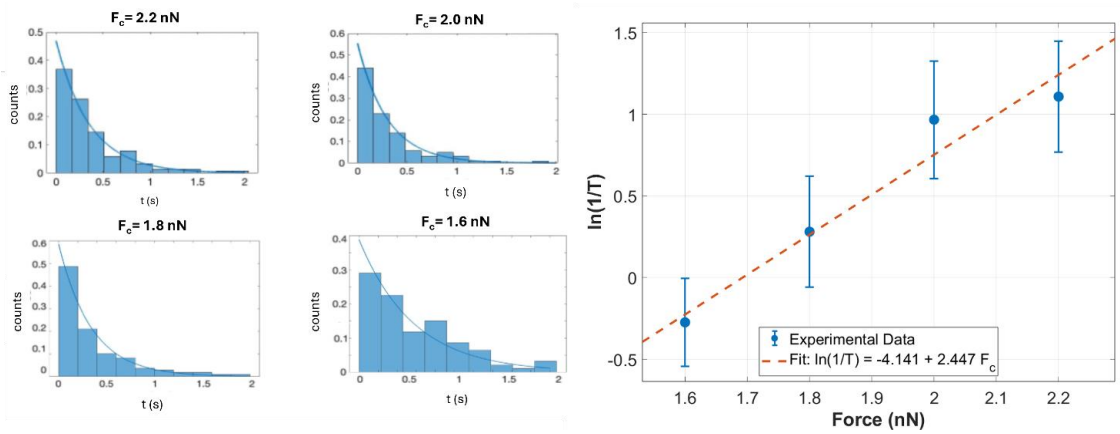

Figure 3-9: (a) Istograms of the time of rupture varying the forces of clamp fitted using the exponential fit. (b) of semi-log graph of the exponential fit results, fitted

For each measurement series, an image of the sample surface was first acquired, and a set of points on the phase of interest was selected, on which Force Clamp curves were subsequently recorded in rapid succession.

Efforts were made to minimize the time interval between image acquisition and the execution of the curves in order to prevent possible drift of the lipid phases.

Study of the mechanical properties of the fluid phase:

The overnight incubation with α-syn induces an unexpected effect. The range of forces accessible before reaching F_b increases significantly, suggesting an enhancement of the membrane's mechanical stability. The FCS analysis confirms this observation, showing an average interaction energy ΔE_0 that is markedly higher: in the control samples the mean value of the energy of (2.5 ± 1.4) k_BT, while the samples incubated with α-syn show a mean value of (6.8 ± 0.9) k_BT (Mean ± SD), as shown in figure *figure 3-10*.

Many experimental observations and simulation already show an increase of membrane rigidity and changes of curvature after the interaction with α-syn oligomers.

However, previous investigations showed a “detergent effect” of amyloid oligomers at high concentrations that is caused by a loss of mechanical stability.

The remodeling of lipid bending seems to have different effect depending on the concentration.

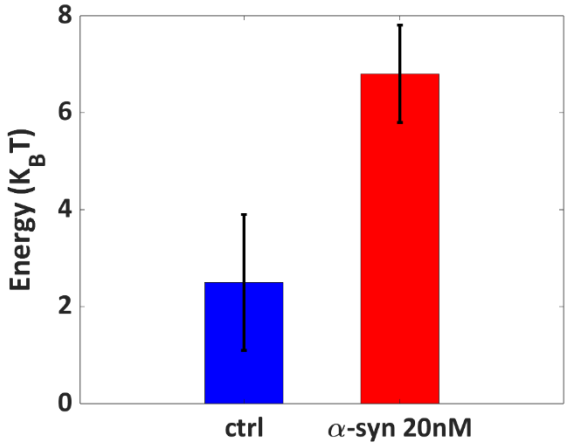

Figure 3-10: Histogram of the FCS results obtained by analyzing the biomimetic membrane incubated with a 20 nM solution of α-synuclein oligomers.

α-synuclein does not span the membrane like a typical transmembrane protein, but it behaves as an interfacial amphipathic molecule: part of its structure associates with the hydrophobic lipid core, while the other part remains exposed to water. This amphipathic arrangement underlies its ability to bind preferentially to curved or compositionally soft membranes and to modulate membrane mechanics. Its N-terminal region adopts an amphipathic α-helical conformation upon binding to lipid membranes. This helix displays a hydrophobic face, which inserts superficially into the outer leaflet of the bilayer, and a hydrophilic face, which remains exposed to the aqueous environment. The tendency to move in aqueous environment of the hydrophobic region of the single protein molecules at higher protein concentration generates a cooperative force that is able to damage membrane integrity, that so called detergent effect.

Study of the Mechanical Properties of the Gel Phase:

The analysis of the gel phase of this membrane proved to be rather challenging, both through force ramp measurements and Force Clamp experiments. In several samples, the rupture event was observed only in a limited number of curves, making it impossible to collect enough data to obtain statistically significant results.

Only for three of the analyzed samples was it possible to acquire a sufficient number of rupture events.

The difficulty in observing the events of interest in the S_o phase can be attributed to the different behavior of the gel phase upon interaction with the AFM tip. It was observed that, after performing the force curves, a subsequent image acquisition *figure 3-11a* revealed the appearance of holes in the membrane precisely at the points where the curves had been recorded.

This phenomenon is not observed in the Ld phase or in the Lo-phase membranes previously analyzed, indicating that the gel phase exhibits a plastic behavior following tip penetration.

The tip induces a progressive plastic deformation in the membrane, which does not involve the sudden rupture event typically recorded in all other cases. This explains why, in most of the curves, a rupture event similar to those observed in other phases is not detected.

The plastic behavior of the gel phase is further confirmed by the analysis of the dynamic force curves. As shown in *figure 3-11b*, the force curves exhibit a hysteresis between the approach and retraction branches, a characteristic feature in indentation measurements of samples displaying plastic deformation. The area enclosed between the two curves provides an estimate of the energy dissipated by the system as a result of deformation.

In *figure 3-11c and figure 3-11d*, a comparison is made between a typical step-like signal observed on the gel phase and that recorded on the fluid phase. In the case of the fluid phase , a regular step signal is observed, with only a minimal relaxation near the end of the upper plateau, which is mostly absorbed by noise. Conversely, examining the curve on the gel phase, the step is often preceded by an extended, gradually descending region with a smaller slope.

This significant deformation preceding rupture confirms that the process in this lipid phase follows a different dynamic.

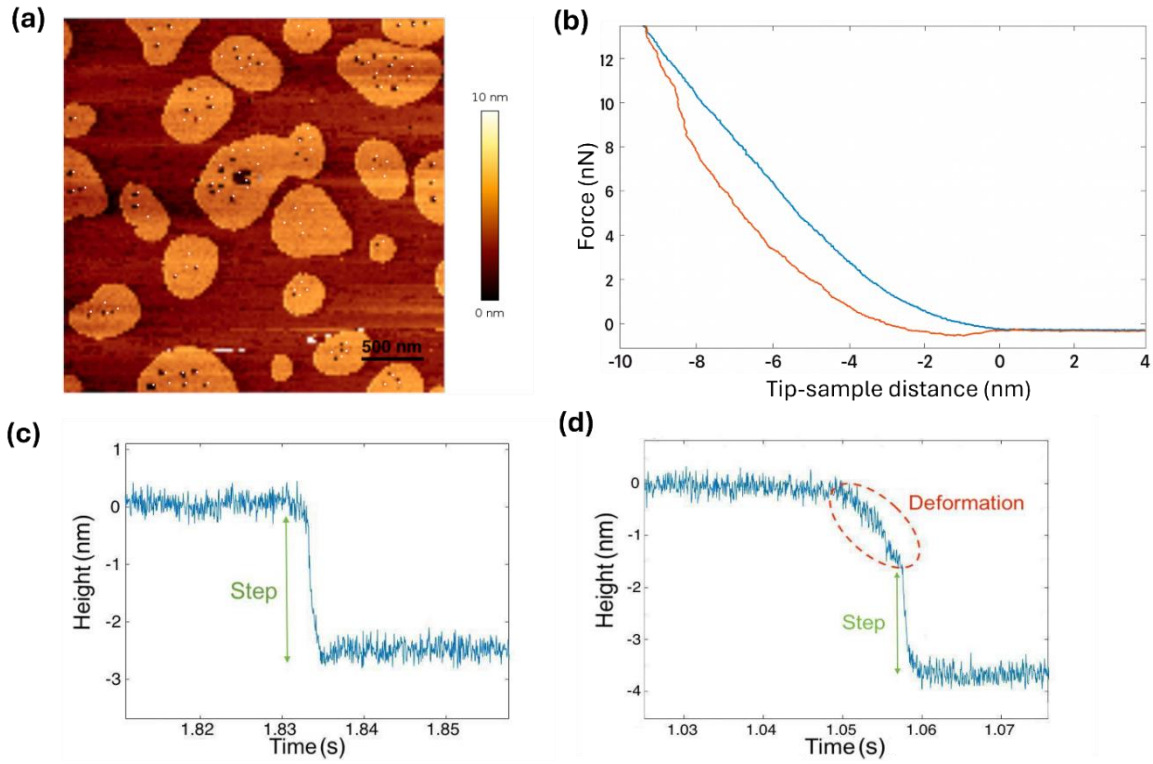

Figure 3-11: (a) AFM image after force-clamp measurements on the rafts. The white dots indicate the points selected for measurement in the JPK software interface. (b) Force-distance curve showing the characteristic hysteresis of plastic behavior. (c) Force-clamp curve typical of the fluid phase. (d) Force-clamp curve typical of the solid phase."

The observations regarding the plastic behavior of the gel phase, combined with the fact that the clamp force range and the average interaction energy are not considerably higher than those found in the other analyzed phases, lead to several possible hypotheses.

The first is that, since the process dynamics differ from those observed in the other phases, the model used may not accurately describe the mechanical properties of this phase.

The second hypothesis is that the model is valid, and the difficulty in observing rupture events is not due to a particularly high interaction energy, but rather to the specific chemical composition of the lipids constituting the S_o phase. Indeed, the polar head of the ganglioside, which is both large and chemically complex, could be responsible for the distinct rupture dynamics observed.

It is also possible that both hypotheses coexist: the model may be inadequate to fully describe the rupture dynamics in this case -thus preventing an accurate estimation of the interaction energy- while, at the same time, the presence of GM1 could be the underlying cause of this different mechanical behavior.

The overnight incubation with α-syn at 20nM of concentration does not produce detectable mechanical effects on the membrane gel-phase. The high rigidity of the SLB does not allow a reproducible FCS curve, so a quantitative analysis of the Energy interaction is not possible.

However, a qualitative analysis does not show differences in terms plasticity and high rigidity of the membrane.

3.4 Conclusions

In this chapter, the mechanical properties of biomimetic lipid membranes were investigated by means of Force Clamp Spectroscopy (FCS), with the aim of elucidating how the interaction with α-synuclein oligomers modulates membrane stability and rupture dynamics across different lipid phases. The analysis was carried out on both control membranes and membranes incubated overnight with α-syn oligomers, focusing on the liquid-disordered (L_d) and solid-ordered (S_o) phases.

For the fluid L_d phase, the morphological investigation was consistent with previously reported results, revealing a progressive loss of mechanical stability and the formation of holes in the membrane as a function of oligomer concentration. In contrast, the morphology of the S_o phase did not show detectable alterations after incubation when compared to control samples, in agreement with earlier studies. The difficulty in observing breakthrough events in this phase prevented a full mechanical characterization. Nevertheless, the analysis of force clamp curves revealed a pronounced plastic behavior, which likely underlies the limitations encountered when applying this technique to this type of lipid phase.

In the fluid L_d phase, force clamp analysis revealed an unexpected behavior. The extracted interaction energy values indicate an enhancement of the mechanical stability of the bilayer following incubation with α-syn oligomers. This observation suggests that the interaction with pathological oligomers induces concentration-dependent modifications of membrane mechanical stability: at low oligomer concentrations, an increase in stability is observed, whereas at higher concentrations the detergent-like effect becomes dominant, ultimately leading to disruption of the fluid phase.

A deeper understanding of this phenomenon will represent the next step of this project, by investigating a broader range of oligomer concentrations and incubation protocols, and by integrating complementary experimental techniques capable of probing the molecular mechanisms underlying this interaction. For instance, correlative super-resolution fluorescence microscopy combined with AFM could be employed to directly

correlate protein distribution on the membrane with local mechanical properties. Alternatively, scattering techniques such as Small-Angle Neutron Scattering (SANS) or Small-Angle X-ray Scattering (SAXS) could provide insight into changes in bilayer curvature and structural rearrangements induced by protein–membrane interactions at the molecular level.

3.5 Bibliography

[1] Grossmann, Guido, et al. "Plasma membrane microdomains regulate turnover of transport proteins in yeast." *The Journal of cell biology* 183.6 (2008): 1075-1088.

[2] S Jonathan Singer and Garth L Nicolson. The fluid mosaic model of the structure of cell membranes: Cell membranes are viewed as twodimensional solutions of oriented globular proteins and lipids. *Science*,175(4023):720–731, 1972.

[3] Garth L Nicolson. The fluid—mosaic model of membrane structure: Still relevant to understanding the structure, function and dynamics of biological membranes after more than 40 years. *Biochimica et Biophysica Acta (BBA)-Biomembranes*, 1838(6):1451–1466, 2014.

[4] Michael Edidin. Lipids on the frontier: a century of cell-membrane bilayers. *Nature Reviews Molecular Cell Biology*, 4(5):414–418, 2003.

[5] Gerrit Van Meer, Dennis R Voelker, and Gerald W Feigenson. Membranelipids: where they are and how they behave. *Nature reviews Molecularcell biology*, 9(2):112–124, 2008.

[6] Ulrich Schmidt, Gernot Guigas, and Matthias Weiss. Cluster formationof transmembrane proteins due to hydrophobic mismatching. *Physicalreview letters*, 101(12):128104, 2008.

[7] Linda J Pike. Rafts defined: a report on the keystone symposium on lipidrafts and cell function. *Journal of lipid research*, 47(7):1597–1598, 2006.

[8] Simons Kai and Ikonen Elina. Functional rafts in cell membranes. *Nature*,387(6633):569–572, 1997.

[9] DA Brown and E London. Functions of lipid rafts in biological membranes.
Annual review of cell and developmental biology, 14(1):111–136, 1998.

[10] Van Meer, Gerrit, Dennis R. Voelker, and Gerald W. Feigenson. "Membrane lipids: where they are and how they behave." *Nature reviews Molecular cell biology* 9.2 (2008): 112-124.

[11] Van Meer, Gerrit, and Anton IPM de Kroon. "Lipid map of the mammalian cell." *Journal of cell science* 124.1 (2011): 5-8.

[12] Harayama, Takeshi, and Howard Riezman. "Understanding the diversity of membrane lipid composition." *Nature reviews Molecular cell biology* 19.5 (2018): 281-296.

[13] Huang, Juyang, and Gerald W. Feigenson. "A microscopic interaction model of maximum solubility of cholesterol in lipid bilayers." *Biophysical journal* 76.4 (1999): 2142-2157.

[14] Daleke, David L. "Regulation of transbilayer plasma membrane phospholipid asymmetry." *Journal of lipid research* 44.2 (2003): 233-242.

[15] Singer, S_J. "The molecular organization of membranes." *Annual review of biochemistry* 43.1 (1974): 805-833.

[16] Van Meer, Gerrit, Dennis R. Voelker, and Gerald W. Feigenson. "Membrane lipids: where they are and how they behave." *Nature reviews Molecular cell biology* 9.2 (2008): 112-124.

[17] Juyang Huang and Gerald W Feigenson. A microscopic interaction model of maximum solubility of cholesterol in lipid bilayers. *Biophysical journal*, 76(4):2142–2157, 1999.

[18] Harayama, Takeshi, and Howard Riezman. "Understanding the diversity of membrane lipid composition." *Nature reviews Molecular cell biology* 19.5 (2018): 281-296.

[21] PM Chaikin and TC Lubensky. *Principles of Condensed Matter Physics*. Cambridge Univ. Press, Cambridge, 1995.

[22] Tamm, L.K., McConnell, H.M. (1985). Supported phospholipid bilayers. Biophysical Journal, 47(1),105–113.

[23] Tanaka, M., Sackmann, E. (2005). Polymer-supported membranes as models of the cell surface.Nature, 437(7059), 656–663.

[24] Simons, K., Ikonen, E. (1997). Functional rafts in cell membranes. Nature, 387(6633), 569 –572.

[25] Veatch, S.L., Keller, S.L. (2005). Seeing spots: complex phase behavior in simple membranes.Biochimica et Biophysica Acta (BBA) - Molecular Cell Research, 1746(3), 172–185.

[26] Lingwood, D., Simons, K. (2010). Lipid rafts as a membrane -organizing principle. Science,327(5961), 46–50.

[27] Seghezza, Silvia, et al. "Cholesterol drives Aβ (1–42) interaction with lipid rafts in model membranes." *Langmuir* 30.46 (2014): 13934-13941.

[28] Reimhult, Erik, Fredrik Höök, and Bengt Kasemo. "Intact vesicle adsorption and supported biomembrane formation from vesicles in solution: influence of surface chemistry, vesicle size, temperature, and osmotic pressure." *Langmuir* 19.5 (2003): 1681-1691.

[29]Richter, Brian D., et al. "A collaborative and adaptive process for developing environmental flow recommendations." *River research and applications* 22.3 (2006): 297-318.

[30] Seghezza, Silvia, et al. "High resolution nanomechanical characterization of multi-domain model membranes by fast force volume." *Journal of Molecular Recognition* 28.12 (2015): 742-750.

[31] Butt, Hans-Jürgen, and Volker Franz. "Rupture of molecular thin films observed in atomic force microscopy. I. Theory." *Physical Review E* 66.3 (2002): 031601.

[32] Redondo-Morata, Lorena, Gerard Oncins, and Fausto Sanz. "Force spectroscopy reveals the effect of different ions in the nanomechanical behavior of phospholipid model membranes: the case of potassium cation." *Biophysical Journal* 102.1 (2012): 66-74.

[33] Relat-Goberna, Josep, Amy EM Beedle, and Sergi Garcia-Manyes. "The nanomechanics of lipid multibilayer stacks exhibits complex dynamics." *small* 13.24 (2017): 1700147.

[34] Zemła, Joanna, et al. "Atomic force microscopy as a tool for assessing the cellular elasticity and adhesiveness to identify cancer cells and tissues." *Seminars in cell & developmental biology*. Vol. 73. Academic Press, 2018.

[35] Evan Evans. Probing the relation between force—lifetime—and chemistry in single molecular bonds. *Annual review of biophysics and biomolecular structure*, 30(1):105–128, 2001.

[36] Sergi Garcia-Manyes, Lorena Redondo-Morata, Gerard Oncins, and FaustoSanz. Nanomechanics of lipid bilayers: heads or tails? *Journal of theAmerican Chemical Society*, 132(37):12874–12886, 2010.

[37] Sergi Garcia-Manyes, Gerard Oncins, and Fausto Sanz. Effect of temperature on the nanomechanics of lipid bilayers studied by force spectroscopy. *Biophysical journal*, 89(6):4261–4274, 2005.

[38] Sergi Garcia-Manyes, Gerard Oncins, and Fausto Sanz. Effect of ph and ionic strength on phospholipid nanomechanics and on deposition process onto hydrophilic surfaces measured by afm. *Electrochimica Acta*,51(24):5029–5036, 2006.

[39] Izhar D Medalsy and Daniel J Muller. Nanomechanical properties of proteins and membranes depend on loading rate and electrostaticinteractions. *ACS nano*, 7(3):2642–2650, 2013.

[40] Chamaree de Silva Arnith Eechampati. Utilization of optical tweezer nanotechnology in membrane interaction studies. *Aplied Nano*, 3(1):43–53, 2022.

[41] Giovanna Coceano, MS Yousafzai, W Ma, F Ndoye, Leonardo Venturelli, I Hussain, Serena Bonin, J Niemela, G Scoles, D Cojoc, et al. Investigation into local cell mechanics by atomic force microscopy mapping and optical

tweezer vertical indentation. *Nanotechnology*, 27(6):065102, 2015.

[42] Andres F Oberhauser, Paul K Hansma, Mariano Carrion-Vazquez, andJulio M Fernandez. Stepwise unfolding of titin under force-clamp atomicforce microscopy. *Proceedings of the National Academy of Sciences*,98(2):468–472, 2001.

[43] Josep Relat-Goberna, Amy EM Beedle, and Sergi Garcia-Manyes. The nanomechanics of lipid multibilayer stacks exhibits complex dynamics. *small*, 13(24):1700147, 2017.

[44] Lorena Redondo-Morata, Marina I Giannotti, and Fausto Sanz. Afmbasedforce-clamp monitors lipid bilayer failure kinetics. *Langmuir*, 28(15):6403–6410, 2012.

[45] Jadavi, Samira, et al. "α-synuclein interacts differently with membranes mimicking the inner and outer leaflets of neuronal membranes." *Biochimica et Biophysica Acta (BBA)-Biomembranes* 1864.1 (2022): 183814.

[46] Redondo-Morata, Lorena, Marina I. Giannotti, and Fausto Sanz. "Influence of cholesterol on the phase transition of lipid bilayers: a temperature-controlled force spectroscopy study." *Langmuir* 28.35 (2012): 12851-12860.

[47] Kulkarni, Chandrashekhar V. "Lipid crystallization: from self-assembly to hierarchical and biological ordering." *Nanoscale* 4.19 (2012): 5779-5791.

[48] Sampaio, Julio Lopes. "The Role of Lipids in Cellular Architecture and Function." (2011).

4

Mechanotransduction in Amiloydoses

4.1 Introduction

The cell system is continuously exposed to internal and external physical forces[1-2]. The ability to recognize and respond to mechanical stimuli is essential for the development and proper function of a multitude of cell types and tissues. Cells sense the mechanical forces through cell-cell interactions, cell organelles embedded into the cytoskeleton, and cell-substrate interactions.

The biological process of force sensation is articulated in three different steps:

The mechanosensation is the recording ability of the mechanical input sensed by the cell, that can be any force applied to the cell itself, such as stretching or straining the cell membrane and unloading or overloading the cells through changes in extracellular mechanical environment.

The mechanotransduction is a process where cells translate the mechanical input into biochemical signals. The cell signaling pathways are composed of a cascade of multiple potential cytosolic mediators that will transmit the biochemical signal from the cell surface to the effector endpoint.

The mechano-adaptation is the effective metabolic response of the cell to the mechanical input through a cytoskeleton organization, changes in gene and protein expression profiles, regulating proliferation, differentiation, migration and other processes.

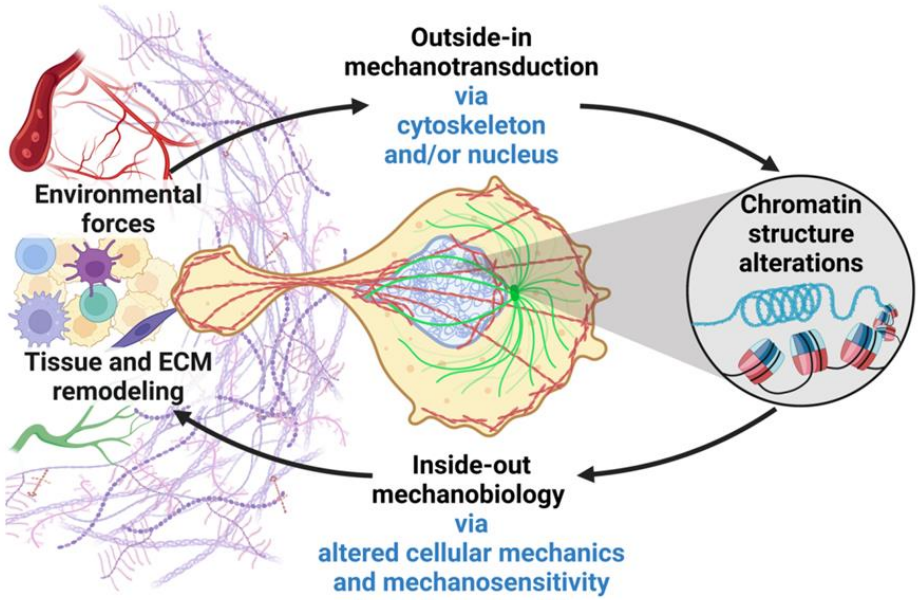

Figure 4-1: Schematic of the mechanotransduction process, which can occur via an outside-in or inside-out mechanism, with a feedback system regulating cell mechanics in response to changes in the extracellular environment or nuclear reorganization [3].

Overall, these three steps define a hierarchical and highly integrated framework through which cells interact with their physical environment. Mechanosensation enables cells to detect mechanical cues, mechanotransduction converts these cues into biochemical signals, and mechano-adaptation allows cells to implement long-term structural and functional responses. In this context, mechanotransduction can proceed through outside-in mechanisms, in which extracellular forces are transmitted across the membrane to the cytoskeleton and the nucleus, or through inside-out mechanisms, whereby intracellular rearrangements, including cytoskeletal or nuclear reorganization, modify cell–matrix and cell–cell interactions. These pathways are embedded within feedback systems that dynamically regulate cell mechanics, allowing cells to continuously adapt to changes in the extracellular environment or to internal structural remodeling.

4.2 Mechanotransduction Channels

The sensing of the mechanical stimuli is based on force-induced conformational changes in mechanosensitive proteins that detect an alteration in the cellular structure, in particular mechanosensitive ionic channels, comprising a broad group of proteins that sense mechanical extracellular and intracellular changes, translating them into cation influx.

The Epithelial Sodium Channel/Degenerin Superfamily

This class of ion channels is present in animals with specialized organ systems and shows different functions according to its tissue distribution. These channels are located on the apical membrane of epithelial cells in various organs, including the kidney, lung, salivary glands, skin, placenta, and colon, where they contribute to Na^+ absorption, water-salt balance, and the regulation of blood pressure.

Transient Receptor Potential Channel Family

Transient receptor potential (TRP) channels are nonselective cation channels and are sensors for a variety of cellular and environmental signals: light, touch or mechanical pain [4]. leading to membrane depolarization through Ca^{2+} influx.

TRP channels are widely distributed in various tissues, including the cardiovascular system, skeletal muscles, lung, kidneys, salivary glands, reproductive system, immune system, and nervous system. The expression of this channel has been described in several cell types, such as sensory neurons, epithelial cells, melanocytes and keratinocytes, and it can be activated not only by mechanical cues but also by pH changes, thermal changes and different ligands, such as cholesterol or nicotine.

Two-Pore-Domain Potassium Channel Family

The two-pore-domain potassium channels (K2P) are a diverse family of K^+ selective channels [5]. These channels perform essential roles in neuronal function, generating a background leak type potassium currents that act to regulate resting membrane potential and levels of cellular excitability. They are regulated by mechanical cues as well as other stimuli such as anesthetics and antidepressant agents, neurotransmitters, post translational modifications or temperature [6]. The subfamily TREK, in particular, is directly regulated by plasma membrane tension, and other mechanical factors such as protein–protein interactions and cytoskeletal modulation.

Piezo Channel Family

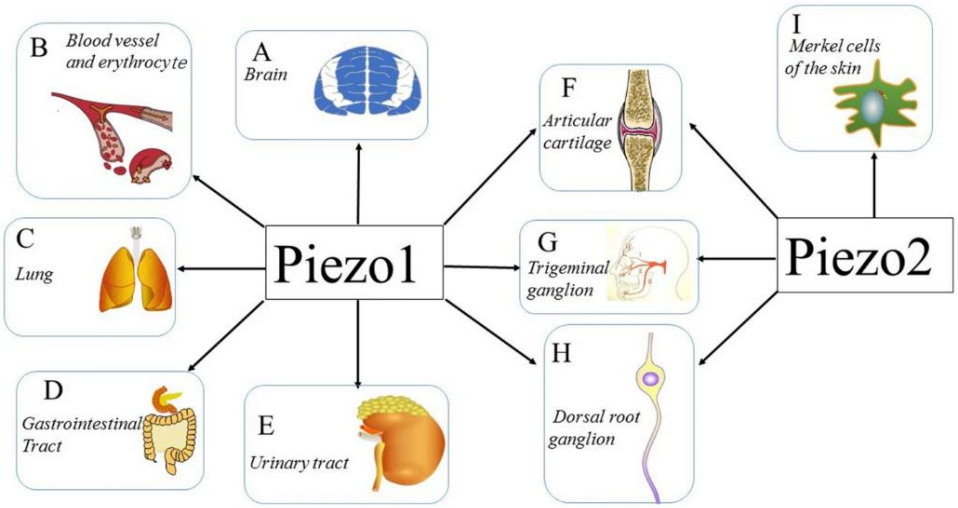

Figure 4-2 Schematic illustration of the expression of Piezo1 and Piezo2 in the different human tissues: Piezo1 channel has a vital role in the CNS, blood vessels, erythrocytes, lungs, gastrointestinal tract and urinary tract. Both channels are employed in articular cartilage, trigeminal ganglia, and dorsal root ganglia. While Piezo2 channel is expressed in Merkel cells, which are involved in sensing light touch.

The Piezo family comprises mechanoreceptors Piezo1 and Piezo2.

Piezo1 was first identified and characterized in a mouse neuroblastoma cell line by Coste and colleagues [7] and they later identified Piezo2 by sequence homology.

Piezo channels are wildly expressed by a multitude of cell types and tissues (*figure 4-2* [8]).

Piezo1 is broadly expressed in many tissues, including the central nervous system, blood vessels, erythrocytes, lungs, gastrointestinal tract, and urinary tract. In contrast, Piezo2 is more tissue-specific and is predominantly found in tissues involved in touch and light-touch sensation. For example, it is expressed in the trigeminal and dorsal root ganglia, as well as in Merkel cells [7].

It is important to note that, while most of the mechanosensitive channels described above exhibit multiple activation mechanisms, the only channels that are principally activated by mechanical stimuli are the Piezo channels. The core function of the Piezo1 channel lies in its ability to directly convert mechanical stimuli into cation influx, thereby initiating downstream signaling cascades. When cells are subjected to mechanical stimuli such as shear stress, membrane stretching, or compression, the Piezo1 channel opens within milliseconds, mediating rapid calcium ions (Ca^{2+}) influx [9], [10]. This process does not rely on second messenger systems, making Piezo1 a true “mechano-chemo transducer.”

Since their discovery, tremendous effort has been made to reveal the structures and biological functions of Piezo 1 and 2. The partial molecular structure of a Piezo channel was determined by cryo-electron microscopy (cryo-EM) [11], [12].

These proteins have an unusually large size compared to other ion channels, with an overall size of over 2500 amino acids, with a large number of transmembrane regions [7].

In this thesis I will focus on Piezo1 activity in nervous system cells in physiological and pathological conditions.

Piezo1 Structure

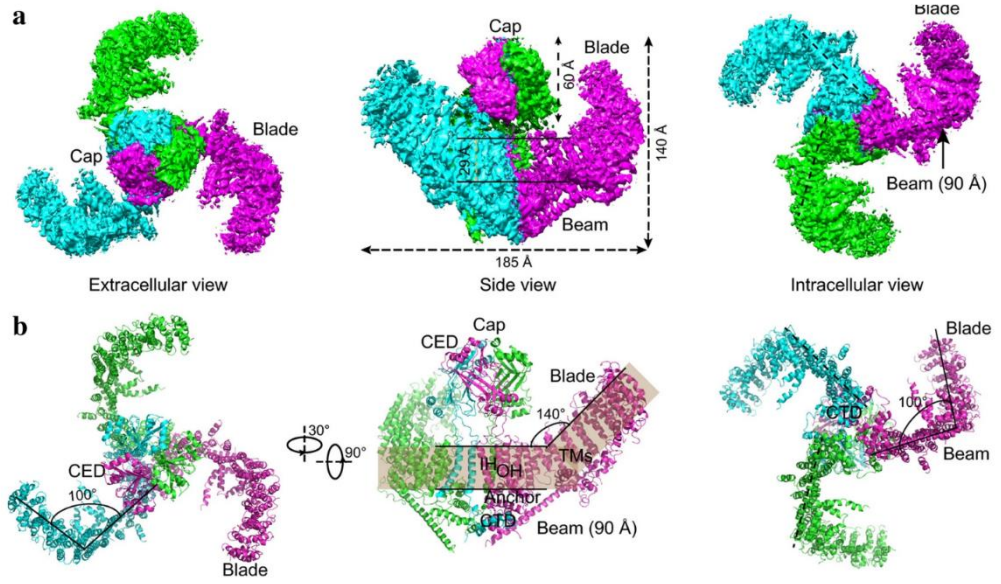

Figure 4-3: Multiple views of the sharpened density map of the trimeric channel with the major domains labeled; the three subunits are colored red, green, and blue. (b) Cartoon representation of the trimeric channel, with the three subunits shown in red, green, and blue. In the central panel, the front subunit has been removed to allow a clearer visualization of the curvature of the transmembrane (TM) region.

Piezo1 exhibits a three-bladed, propeller-shaped homotrimeric structure that includes a central cap, three peripheral blade-like structures on the extracellular side, with nine repetitive folds containing 4 trans-membrane (TM) regions each, named transmembrane helical units (THUs), three long beams on the intracellular side that bridge the blades to the cap, and a TM region between these features[13] (*figure 4-3* [6]).

Piezo2 channel and Piezo1 channel share approximately only 42% sequence homology [7].

Recent studies[14] have shown that the overall structure of the Piezo2 channel is very similar to that of Piezo1 in that it forms a three-bladed, propeller-like homotrimeric

structure comprising a central ion-conducting pore module and three peripheral blades with 38 TMs.

In the Piezo2 channel, the charged residues at the interface between the beam and the CTD are required to ensure the normal mechanosensitivity of the channel [15].

Mechanotransduction Mechanism of Piezo Channels

The curved blades composed of THUs can act as a mechanosensor, while the beam structure, acting as a pivot, can act as a lever-like apparatus. Coupling the distal blades and central pore through the lever-like apparatus converts mechanical force into a force used for cation conduction.

Because the pivot of the lever is positioned closer to the central pore than to the distal blades, the input force is effectively amplified through the lever-like apparatus. Additionally, a large conformational change in the distal blades is converted into a relatively slight opening of the central pore, allowing cation-selective permeation.

Moreover, Piezo proteins have the ability to locally deform lipid membranes into a dome-like shape[14] experimentally proved to explain the activation mechanisms of Piezo channels [16]. Lateral membrane tension flattens the Piezo dome, which increases the energy of the membrane-channel system in proportion to the expansion of the projected area of the dome. Piezo channels then open due to the relative energy difference. This mechanism can account for the highly sensitive mechanical gating of Piezo channels with a cation-selective pore.

The Piezo channels exhibit three distinct states, namely closed, open, and inactivated.

Piezo proteins are characterized also by their inactivation different kinetics, both are fast at negative membrane potentials and slow at positive membrane potentials, but Piezo1 channel inactivation is relatively slow compared with Piezo2 channel inactivation[7].

Studies have proposed that the Piezo1 channel is gated directly by bilayer tension that can be modified by cytoskeletal proteins and linkages to the extracellular matrix (ECM) (*figure 4-4a [16]*).

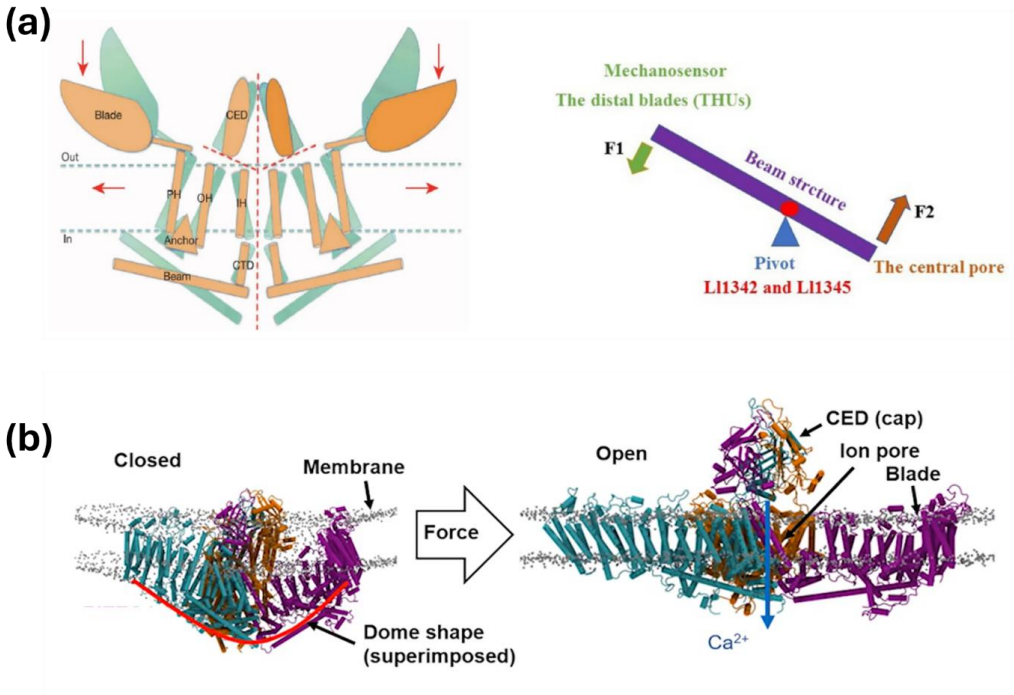

Figure 4-4: On the left, a schematic illustration of the Piezo channel conformational changes. On the right scheme of the peripheral lever-like apparatus consisting of the blades and a beam to gate the central ion-conducting pore model that e (b) Model of open mechanism of Piezo protein gaiting based on changes in membrane curvature into a dome-like shape after a force stimulus.

Various modulators, such as pH, temperature, ion concentrations and membrane lipid composition have also been reported to regulate the Piezo channel kinetics, however today there are few knowledges about the relationship between the Piezo kinetics and its molecular structure.

During the active state of the channel, a unidirectional flux of Ca^{++} ions from the extracellular environment to the intracellular region is generated, inducing an increase of the intracellular calcium concentration.

Calcium plays a crucial role in the translation of physical forces to cellular signals through a mechanism involving changes in its cytosolic concentration.

Depending on the calcium signal, responses can range from short term effects such as gene transcription, signal transduction, contraction and secretion to longer term regulation of migration, proliferation, differentiation [17] and apoptosis [18].

Moreover, calcium signals regulate the microtubule and actin polymerization [19], the formation of stress fibres [20], modifying the cytoskeleton structure.

Not all responses are positive for cell survival, as calcium can be highly toxic when its normal concentration is exceeded. A continuous increase in calcium concentration

could lead to cellular damage by the activation of proteases and the augmented production of reactive oxygen species.

Pharmacological modulators of Piezo channels

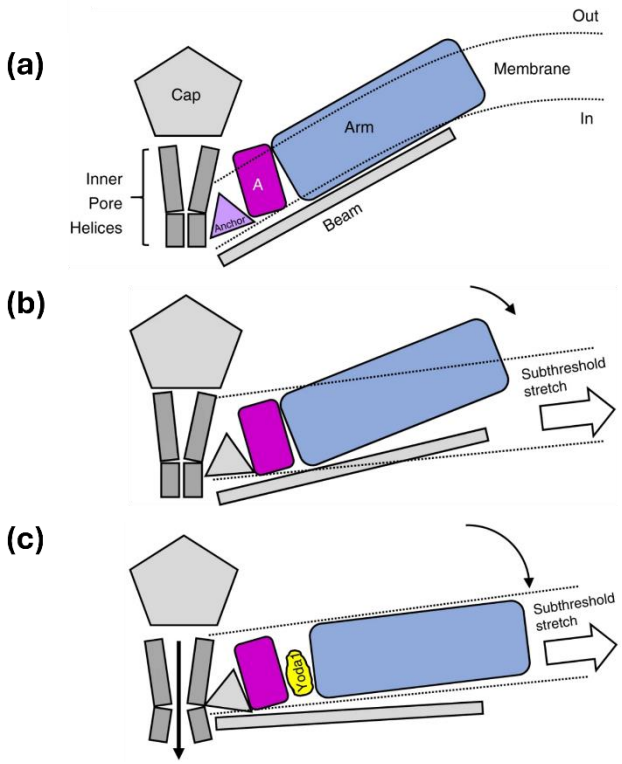

Figure 4-5: Molecular wedge mechanism underlying Yoda1-mediated Piezo1 activation. (a) In the absence of membrane tension, the Piezo1 arm (blue) adopts a flexed conformation (one arm shown for clarity). (b) Under sub-threshold mechanical stimulation, partial membrane flattening induces limited arm extension, insufficient to open the pore. (c) Yoda1 binds between Repeat A (magenta) and the N-terminal region of the arm, acting as a molecular wedge that enhances tension-induced arm extension, thereby promoting channel opening under sub-threshold stimuli. The downstream mechanism linking lever motion to pore opening remains unknown.

The gating behaviour of Piezo channels is not only dependent on mechanical stimuli form the extracellular environment or modifications of the cytoskeleton but is also regulated by pharmacological agents.

Yoda1 is the first selective agonist for the Piezo1 channel, which functions by binding to the channel and facilitating force-induced protein motions through a wedge-like mechanism. This agonist stabilizes the open conformation of the channel, thereby reducing its mechanical threshold for activation Yoda1 binds allosterically to A pocket about 40 A from the central pore and acts as a molecular wedge to facilitate force-induced conformational changes by lowering the mechanical activation threshold of the channel [21] (*figure 4-5*).

Jedi1/2 are others hydrophilic Piezo1 chemical activator. The structural dissimilarity between Jedi1/2 and Yoda1 suggests a variance in their respective activation mechanisms.
Specifically, Yoda1 acts at the downstream beam as a molecular wedge, while Jedi1/2 acts through the peripheral blades and utilizes a peripheral lever-like apparatus consisting of the blades and a beam to gate the central ion-conducting pore [13].

In the work I used Yoda as specific Piezo1 channel activator to test the experimental setup and the effectiveness of Piezo1 overexpression.
The most commonly used inhibitors of the Piezo1 channel are grammostola spatulata mechanotoxin 4 (GsMTx4), gadolinium (Gd^{3+}) and ruthenium red (RR).
GsMTx4 is a sideropeptide containing six lysine residues, that has the ability to inhibit mechanosensitive ionic channels and can block the Piezo1 channel, acting via modulating local membrane tension near the channel[22].
While RR and Gd^{3+} are small molecules that can block Piezo channels in a non-specific manner.

Piezo1 in Nervous System:
Recent studies have shown that mechanical forces determined neural development and function [23]. Mechanical signals encountered during development include changes in tissue stiffness, fluid shear flow, and hydrostatic forces in the cerebrospinal fluid from the developing ventricles, all of which can affect the expression of Piezo1 channels.
Piezo1 channel has a fundamental role also in modulating the activity of the Central Nervous system (CNS).
The CNS is comprised of a multitude of cell populations that are highly interconnected yet functionally diverse, including, neurons, oligodendrocites (OLs), microglia and astrocytes.
These cells demonstrate a significant degree of mechanosensitivity, whereby mechanical stress can activate or inhibit intracellular signaling pathways by modulating the activity of the Piezo1 channel located in the cell membrane.
The link between the Piezo1 channel and the nervous system was first recognized because Piezo1 is positioned with a punctate distribution along the axons and growth cones of *Xenopus* retinal ganglion cells (RGCs), a part of the CNS [24].

The Piezo1 channel is expressed by human neural stem cells and plays an important role in directing the lineage choice of neural stem cells towards a neuronal or astrocytic phenotype [25].

Infact, neural stem cells are self-renewing cells with the capacity to differentiate into neurons, astrocytes, and oligodendrocytes. This process is extremely sensitive to the mechanical properties of the cellular environment [26].

Piezo1 proteins and neurodegenerative diseases

Because this channel plays a key role in neuronal mechanotransduction, understanding Piezo's involvement in neurodegenerative diseases has become an area of growing scientific interest.

The brain is softer and more sensitive than other tissues in the body, and its soft tissues are very sensitive to mechanical stimulation. Several studies highlight the effects of amyloidosis like AD and PD on the brain tissue mechanics Amyloid plaques can produce stiff mechanical stimulation of the brain tissue, which activates the immune function of astrocytes and microglia, leading to the engulfment of glial cells [27] [28].

Stiff amyloid plaques may upregulate Piezo1 channels in microglial cells and affect their immune activity; however, the underlying mechanism remains unknown. Studies on AD have shown that the stiffness of Aβ plaque-associated tissues is increased, and the mechanosensitive ion channel Piezo1 is selectively upregulated in Aβ plaque-associated microglia. Piezo1 further sensory stiffness stimulates Aβ fibrils, which subsequently induces Ca2+ influx and promotes microglia aggregation, phagocytosis, and Aβ plaque compaction [29]. How these changes are related to the specific pattern of Piezo1 activity remains unclear.

For the Piezo1 channel, several studies have demonstrated that Aβ affects its activity and function, but different forms have been shown to have different effects. In vitro, even femtomolar to picomolar concentrations of Aβ monomers can inhibit fluid shear stress-stimulated Piezo1 channel activity, while the more aggregated forms of the peptide (oligomers) were less potent. Further research found that the inhibition of Piezo1 activity by Aβ and the resulting block in Ca^{2+} influx was accompanied by a significant increase in F-actin tension, suggesting that the effect of Aβ on Piezo1 activity may be related to cytoskeletal reorganization [30]. In addition, some authors believe that the interaction of Aβ with the lipid membrane affects the activity of the Piezo1 channel [27]. The expression and activity of Piezo in PD is today not really investigated.

As shown in the previous chapter of this thesis, I analysed the mechanical destabilization of a biomimetic lipid bilayer interacting with α-syn oligomers. The SLB model system makes it possible to isolate only a few variables of a real biological environment - specifically, the lipid components of the membrane and the pathological peptide of interest- and to obtain quantitative results.

However, achieving a comprehensive understanding of the problem requires exploring different systems and scales of complexity.

The activity of Piezo channels is tightly linked to the mechanical properties of the cytoplasmic membrane, and calcium homeostasis -also regulated by these channels- is an intriguing parameter to monitor in relation to the presence of amyloidosis. The lack of knowledge regarding the relationship between Piezo activity and Parkinson's disease motivated me to investigate this aspect in greater depth.

In order to investigate the activity of mechanosensitive channels—particularly Piezo1—under both physiological and Parkinson's-disease-related pathological conditions, I employed a single-cell system using a neuron-derived cell line (A1) that overexpresses Piezo1 (A1-OV). This strategy enables an amplification of the Piezo-dependent signal, making the contribution of other channels negligible.

I developed a correlative experimental setup combining an AFM with an epifluorescence microscope. This configuration allows the application of a controlled, nanometrically precise mechanical stimulus to the cell while simultaneously monitoring the calcium fluxes induced by the activation of mechanosensitive channels.

The experimental setup

To investigate the Piezo1 channel activity, I adapted a Fluorescence Microscopy (FM) – Atomic Force Microscopy (AFM) correlative setup, to detect the inner cell calcium level during a live process of mechanical destabilization induced by amyloid oligomers [31].

The design of the experiment is to stain the cell sample with a calcium-sensitive dye, capturing fluorescence images over time, during a process that induces the activation of Piezo1 channels through mechanical or chemical stimuli.

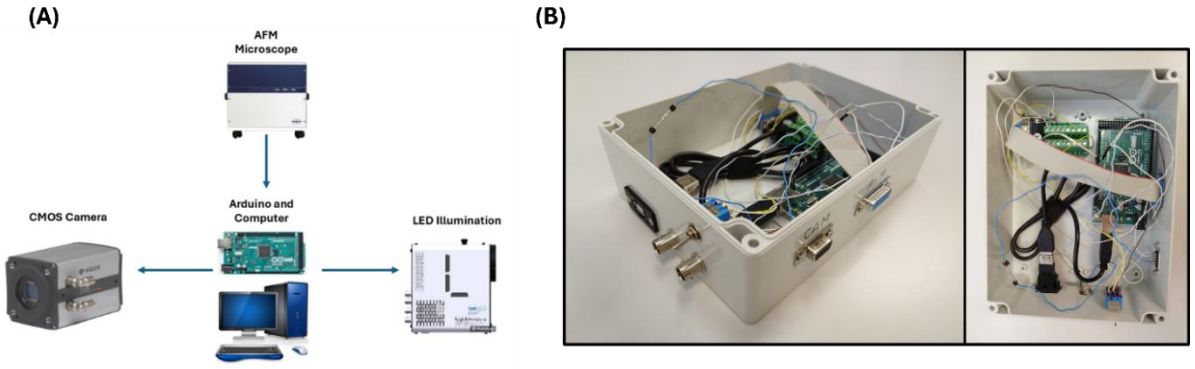

Figure 4-6: (A) Cartoon of the experimental setup, involving the AFM microscope, whose action triggers Arduino and the Labview program to start the acquisition. (B) Photos of the custom controller box, containing Arduino, the instrument's connectors and a switcher to pass from the AFM synchronized mode to the fluorescence-only mode.

The experimental setup (*figure 4-6*) integrates an inverted epifluorescence microscope (DMI8, Leica), a high-speed scientific CMOS camera (Zyla sCMOS 4.2, Andor), an LED illumination system (pE-340fura, CoolLED) for fluorescence excitation, and an atomic force microscope (JPK Nanowizard IV, Bruker) used to apply a precisely controlled mechanical stimulus. This hybrid configuration enables the simultaneous acquisition of high-resolution calcium signals and the delivery of localized mechanical perturbations at the nanoscale.To coordinate all components, I developed a custom LabVIEW software environment capable of synchronizing, with sub-millisecond precision, the camera acquisition, the LED illumination timing, and the AFM stimulus. Communication among the devices was managed through an Arduino-based electronic interface (Arduino MEGA 2560, Arduino), which was used to generate and route TTL pulses.

The control architecture was designed to minimize latency and ensure reproducibility of the temporal sequence of events—an essential requirement when probing the fast kinetics of calcium influx mediated by Piezo1.

Because calcium imaging can be performed using different categories of fluorescent indicators, I implemented two versions of the LabVIEW program to accommodate both single-wavelength (SW) intensity-based dyes and dual-wavelength ratiometric (WR) dyes. These two classes differ in their operational principles: SW dyes modulate fluorescence intensity upon binding calcium, whereas WR dyes rely on a shift in their

excitation spectrum, allowing ratiometric quantification that compensates for dye concentration, photobleaching, and focal drift.

In this work, Oregon Green BAPTA-1 and Fura-2 were selected as representative SW and WR dyes, respectively, due to their high sensitivity and compatibility with live-cell imaging.

The software interface allows full control of key imaging parameters—including the number of acquired frames, exposure time, frame rate, camera bit-depth, and illumination power—providing flexibility for experiments involving different dyes, cell types, and stimulation protocols. To limit photobleaching and reduce cytotoxicity associated with prolonged LED exposure, illumination was restricted to the exact time window during which the camera sensor is in acquisition mode. This was achieved by triggering the LED driver using a TTL pulse derived from the camera's "sensor-gating" output.

Similarly, the initiation of the AFM mechanical stimulation was synchronized to the camera acquisition using a dedicated TTL signal, ensuring a well-defined temporal relation between the mechanical perturbation and the observed calcium response.

This integrated and fully synchronized opto-mechanical platform enables precise time-resolved measurements of mechanosensitive channel activity, while minimizing artefacts arising from illumination, mechanical delays, or asynchronous acquisition.

4.3 Materials and Methods

Cell culture

The A1 cell line was generated by retroviral infection of mouse embryonic mesencephalic neurons with the immortalizing c-myc gene. Cells were cultured in DMEM/F12 medium (Euroclone) supplemented with 10% fetal bovine serum (FBS) (Gibco). Differentiation of A1 cells was induced at 50% confluence following the protocol described by Colucci et al. [52], using serum-free medium supplemented with 1 mM N6,2'-O-dibutyryladenosine 3',5'-cyclic monophosphate sodium salt (cAMP) (Sigma) and N-2 Supplement (100×) (Gibco, diluted 1:100), for up to six days.

Cells were then transfected with a human PIEZO1-GFP plasmid (kindly provided by the Victor Chang Cardiac Research Institute, Sydney) using Lipofectamine (Invitrogen) and subjected to antibiotic selection. The resulting positive colonies (A1-OV) were isolated and characterized.

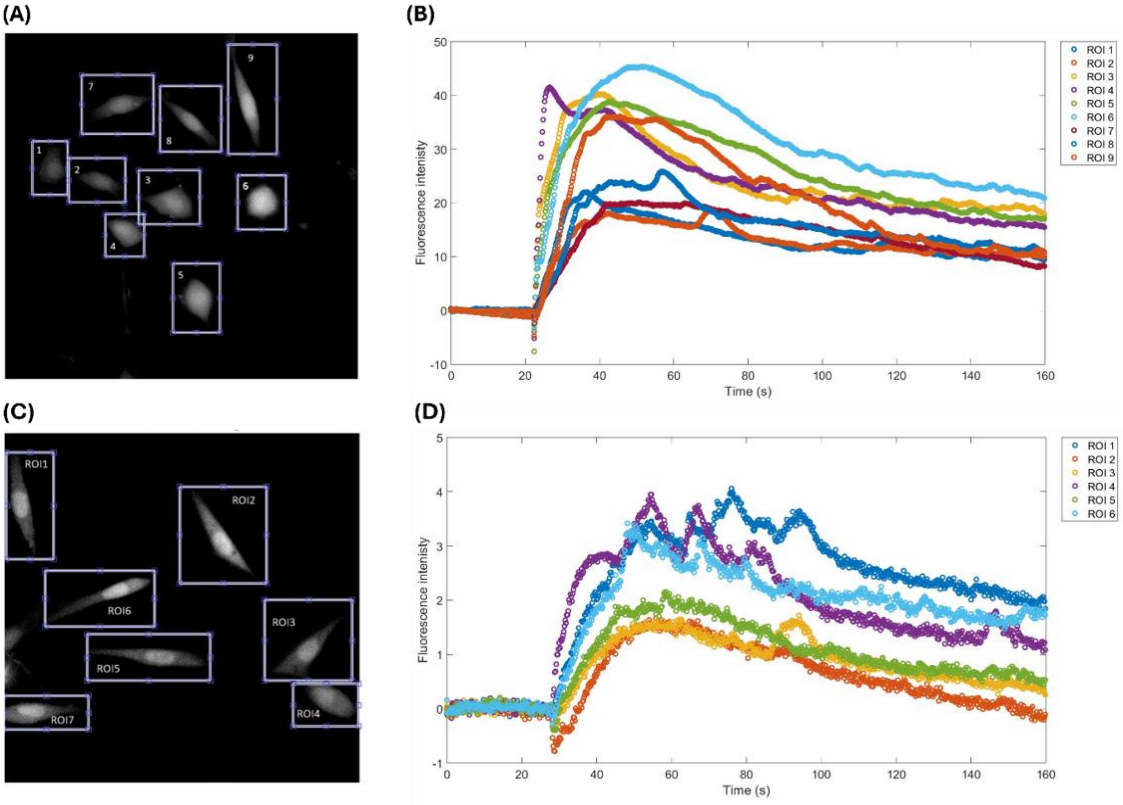

Figure 4-7: (A-B) Calcium Image of A1-OV cells and relative graph of the fluorescence intensity during the time (proportional to the calcium concentration). After 20 seconds circa, we can see the signal increase due to the Yoda perfusion. (C-D) Calcium Image of A1 wild type and relative graph of fluorescence intensity during the time, here we observe Yoda perfusion starts at 30 seconds circa.

Chemical Stimulation of Piezo1 Channel

To quantitatively assess the degree of signal amplification mediated by Piezo1 in overexpressing cells, a chemical stimulation was performed using the selective agonist Yoda1 at a fixed concentration of 2 µM [21]. The goal was to compare the calcium influx dynamics between Piezo1-OV cells and their wild-type counterparts, thereby determining the functional impact of channel overexpression. For monitoring intracellular calcium, cells were incubated with the SW fluorescent indicator Oregon Green BAPTA-1 at a concentration of 5 µM, chosen for its high sensitivity to Ca^{2+} fluctuations and its fast-binding kinetics.

After recording the basal fluorescence signal for approximately 20 seconds, the cells were perfused with the Yoda1-containing solution. Application of the agonist triggered a rapid and pronounced increase in fluorescence intensity, indicative of a substantial Ca^{2+} influx through activated Piezo1 channels (*figure 4-8*). The peak of the response was typically reached 15–20 seconds after the onset of perfusion, consistent with activation kinetics reported in the literature. Following the peak, the signal gradually declined, returning to baseline approximately 200 seconds after stimulation, suggesting efficient intracellular Ca^{2+} buffering and clearance mechanisms.

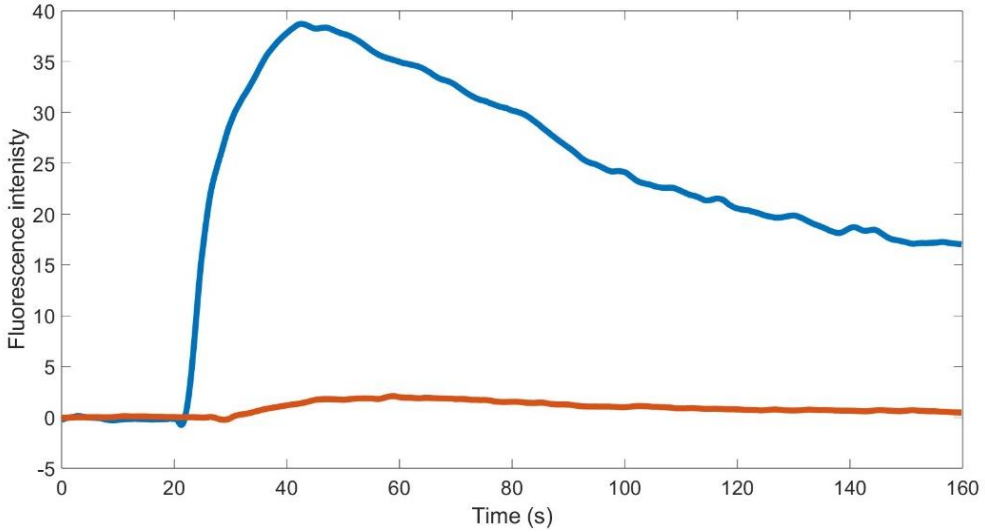

Figure 4-8: Fluorescence signal associated with intracellular calcium concentration following cell perfusion with Yoda1. The blue trace corresponds to the average signal from A1-OV cells, while the orange trace represents the average signal from A1 wild-type cells.

As shown in the *figure 4-7*, which reports the averaged calcium-response traces for both conditions, overexpression of Piezo1 leads to a strongly amplified cellular response. Specifically, the amplitude of the signal in Piezo1-OV cells is roughly 40-fold higher than that observed in wild-type cells. This result indicates that increased Piezo1 expression not only raises the number of available channels but also markedly enhances the cell's ability to generate a calcium influx upon Yoda1 stimulation.

Mechanical stimulation of Piezo1 Channel in Pathological Conditions

In order to investigate the influence of α-syn amyloid oligomers on Piezo1 activity, I used the correlative AFM–fluorescence setup described previously, which enables the simultaneous application of a controlled mechanical stimulus and the real-time acquisition of intracellular calcium variations. For this study, only the Piezo1-OV glia-

model cells were used, since the overexpression of Piezo1 ensures a stronger and more easily detectable mechanosensitive calcium response, while minimizing the contribution of endogenous channels.

The α-syn oligomer solution was added to the culture medium at a final concentration of 1 μM and incubated overnight at 37 °C in a 5% CO_2 atmosphere.
The same cell system and the same setup were used also to investigate the interaction of the Aβ oligomers - related to the Alzheimer's disease as exposed in the previous chapter of introduction- and the effects on the Pezo1 activity.
Following the same protocol for α-syn, the Aβ oligomers solution was added to the cell culture medium at the concentration of 2 μM.
This incubation step allows the oligomers to stably interact with the plasma membrane and possibly alter its mechanical properties before the mechanical stimulation experiments. Following incubation, the cells were gently washed twice with PBS to remove free oligomers and avoid non-specific effects.

To monitor intracellular calcium, the cells were then stained with Oregon Green BAPTA-1 at a concentration of 5 μM and incubated for 45 minutes in PBS. The choice of this dye was motivated by its high brightness and fast kinetics, which make it particularly suitable for resolving the rapid calcium transients associated with Piezo1 activation. Furthermore, its excitation wavelength in the visible range minimizes phototoxicity compared to UV-excitable ratiometric dyes such as Fura-2, reducing light-induced stress that could interfere with the experiment.
Mechanical stimulation was applied using an AFM JPK Nanowizard IV (Bruker, USA) and a colloidal probe consisting of a tipless cantilever with a nominal elastic constant of 2 N/m functionalized with a polystyrene bead of 5 μm radius (Polysciences, USA).

The probe was prepared by dispersing the microbeads in ethanol through ultrasonication to avoid aggregation. A glass slide was thoroughly cleaned in a detergent solution (Hellmanex, Hellma, Germany), rinsed, and dried under nitrogen. A droplet of the bead suspension was placed on one side of the slide, while a thin layer of UV-curable glue was deposited on the opposite side. The tipless cantilever was first dipped into the glue and then brought into gentle contact with a single bead. After maintaining contact for approximately 30 seconds, the UV LED of the microscope illumination system was activated to initiate a partial curing of the adhesive, ensuring the stable attachment of the bead to the cantilever without excessive glue spreading (figure 4-9).

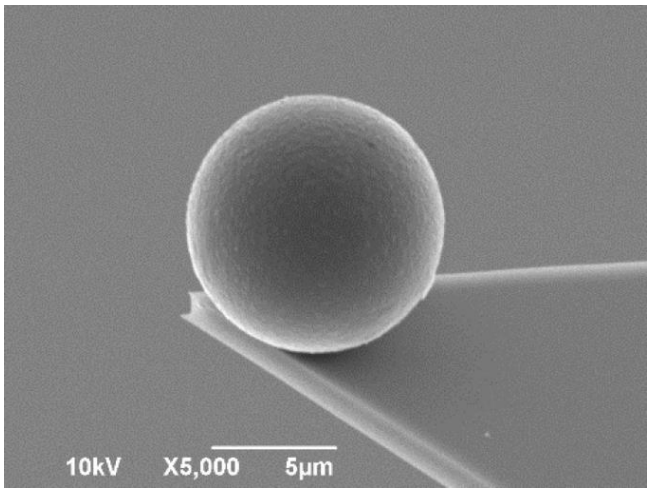

Figure 4-9: SEM images of the micro-bead attached to the cantilever.

The mechanical protocol was configured with a force setpoint of 400 nN applied for 1.0 seconds and an approach velocity of 30 µm/s. These parameters were selected to reliably an consistent deformation of the membrane that induces the activate Piezo1, avoiding irreversible damage to the cell. The AFM stimulation was synchronized with the fluorescence acquisition through a custom LabVIEW program interfaced with an Arduino MEGA 2560, which managed the triggering of the LED illumination and the camera sensor. This synchronization ensured precise temporal alignment between the onset of mechanical stimulation and the detection of the Ca^{2+} signal, allowing a direct correlation between force application and channel activation.

The image parameters have been chosen in order to optimize the acquisition of the fluorescent signal with a good signal-to-noise ratio, minimize the photobleaching and maintain a rate of acquisition enough to resolve the phenomenon.

To increase both the detected signal and the achievable frame rate, a 2×2 binning was applied during image acquisition. Binning is a procedure used in digital imaging detectors

in which the signal from multiple adjacent pixels is combined into a single “super-pixel.” During acquisition, instead of reading the intensity of each pixel individually, the detector sums (or averages) the charge accumulated in a group of neighbouring pixels. This process enhances the effective signal and reduces readout noise, thereby allowing faster acquisition rates, although at the cost of decreased spatial resolution.
With these settings, it was possible to maintain the LED illumination at 20% power while using an exposure time of 80 ms and achieving a frame rate of 10 images per second.

During the measurements, the sample was kept at 37 °C using a PetriDish Heater (Bruker), ensuring stable physiological conditions throughout the experiment (*figure 4-10*). After each mechanical stimulation, a new cell was selected for analysis in order to avoid artefacts related to desensitization of mechanosensitive channels. Moreover, to preserve cell viability and prevent temperature- or phototoxicity-induced alterations in calcium signalling, the total duration of the experiments performed on a single Petri dish

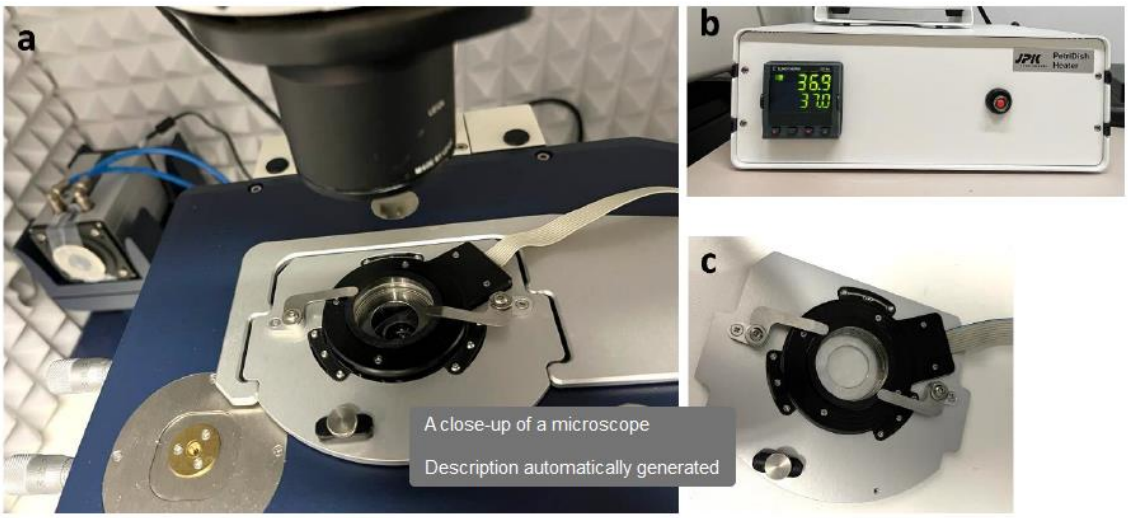

Figure 4-10: (a) the AFM stage and the sample with an objective under the position of sample (b) the Petri dish heater (c) the PetriDish chamber that connects to the heater.

did not exceed two hours.

Software for Data Analysis

The acquired images were analyzed using a custom Matlab program. First, the background signal is subtracted from the images, and then specific regions of interest (ROIs) corresponding to each cell are identified in the image. The software calculates the fluorescence increase for each cell, that is the sum of the fluorescence intensity values

in all the pixels of the ROI, subtracted by the average fluorescence before the perfusion with Yoda. The fluorescence value is normalized to the cell size (the number of non-null pixels in a ROI). The formula used to calculate the normalized fluorescence value in a ROI is:

$$I_{norm}(t) = \frac{I(t) - < I(t) >_{20s}}{\sum_{ROI} Pixels_{\neq 0}}$$

where I(t) is the intensity of fluorescence, $< I(t) >_{20s}$ is the average fluorescence intensity of the first 20 seconds of measurement and $\sum_{ROI} Pixels_{\neq 0}$ is the number of non-null pixels, that corresponds to the cell in a ROI.

The analysis was made considering the difference between the basal level of calcium and the curve peak.

4.4 Results

The calcium imaging measurements were acquired on 55 cells incubated with α-syn oligomers, 61 cells incubated with Aβ oligomers and 68 CTL cells.

The calcium peak intensity measured after the mechanical stimulation were considered as representative parameter of the calcium exchange with the extracellular environment.

The experimental results show no significant difference in the calcium peaks recorded upon mechanical stimulation of control cells compared to cells incubated with α-syn oligomers.

An example of experimental calcium curve and experimental data distribution is reported in the boxplot in *Figure 4-11*.

This observation stands in contrast with the behaviour previously identified in the biomimetic membrane system, where α-syn oligomers induced a clear mechanical

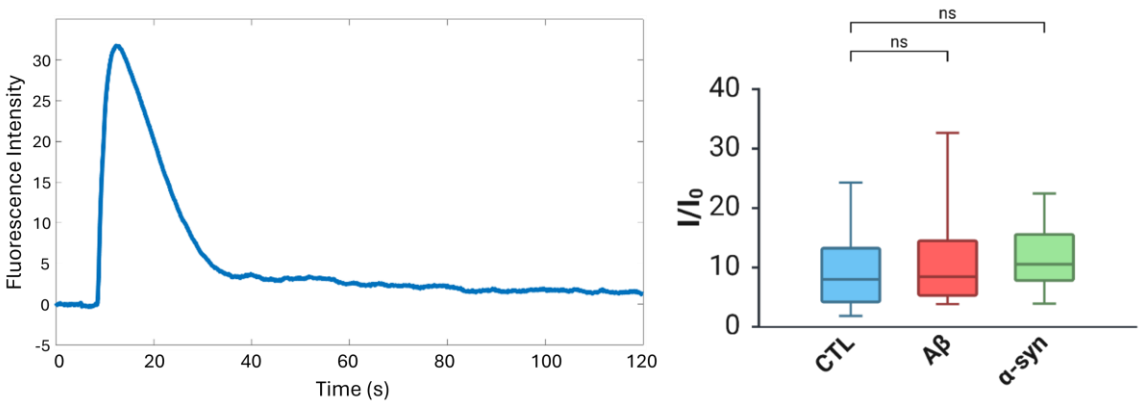

Figure 4-11:(a) Experimental curve showing intracellular calcium levels after mechanical stimulation using the AFM. (b) Boxplot of calcium peak amplitudes obtained upon mechanical stimulation of control A1-OV cells and of the same cell type after incubation with Aβ and α-syn oligomers. Statistical analysis was performed using a one-way ANOVA.

destabilization of the lipid bilayer. Given that Piezo1 channel gating is strongly sensitive to variations in membrane tension, curvature and lateral stress, a comparable alteration in the mechanical response of the cellular membrane was expected to manifest as a measurable modification in channel activation. However, the cellular system appears to respond in a fundamentally different manner.

The absence of detectable variations in calcium homeostasis suggests that additional regulatory mechanisms are operating within the complex environment of a living cell that are absent in simplified model membranes. Unlike supported lipid bilayers, cellular membranes are tightly coupled to the underlying cytoskeleton, which plays a crucial role in distributing and buffering mechanical forces. This anchorage may counterbalance the mechanical perturbations induced by α-syn oligomers, effectively masking their direct effects on the lipid component alone. Furthermore, mechanosensitive signalling in cells arises from the integrated activity of multiple ion channels and regulatory pathways. The activation of compensatory channels or the action of homeostatic mechanisms regulating calcium efflux, buffering or sequestration could contribute to maintaining calcium levels within physiological limits, even in the presence of potentially destabilizing agents.

Another important factor to consider is the role of membrane trafficking and lipid turnover. Living cells continuously remodel their membrane composition through endocytosis, exocytosis and lipid recycling, potentially diluting or reorganizing the interaction between oligomers and the membrane. Additionally, α-syn oligomers may undergo different internalization or degradation pathways in a cellular environment, resulting in a reduced effective concentration at the plasma membrane compared to the controlled conditions of a model system.

4.5 Conclusions

The calcium imaging experiments performed on A1-OV cells revealed results that differ from those obtained in the FCS analysis discussed in the previous chapter. While incubation with pathological oligomers did not induce appreciable effects on cellular mechanotransduction, the same amyloid oligomers produced pronounced changes in the mechanical stability of the supported lipid bilayer (SLB) model membrane system. These observations indicate that the cellular response to α-synuclein oligomers is governed by a combination of structural, biochemical, and regulatory mechanisms that can buffer or compensate for local alterations in membrane mechanics. This discrepancy highlights the importance of complementing studies on simplified model membranes with experiments on living cells in order to fully capture the complexity of mechanotransduction under physiological and pathological conditions.

The investigation of the effects of Aβ oligomers on Piezo1 activity in the A1-OV single-cell system yielded results comparable to those obtained for α-synuclein oligomers. No significant differences in calcium peak amplitudes were detected between cells exposed to Aβ oligomers and control conditions. Also in this case, the absence of detectable effects suggests that, in intact cells, additional regulatory mechanisms may compensate for or mask the mechanical perturbations induced by Aβ oligomers.

Another possible explanation concerns the aggregation state of the oligomers. Aβ oligomers are highly heterogeneous, and their biological activity strongly depends on size, conformation, and stability. Different aggregation states exhibit distinct membrane affinities, insertion capabilities, and toxic potentials. It is therefore possible that the oligomeric species present during the experiments—due to the preparation protocol, incubation time, or spontaneous evolution of the aggregates—were not in a conformation capable of significantly perturbing membrane mechanics or effectively modulating Piezo1 activity.

Finally, it is important to note that, due to time constraints, the effects of these pathological aggregates were not investigated on simplified model systems such as biomimetic supported lipid bilayers. Such an approach would be essential to isolate membrane-specific contributions and to disentangle them from the compensatory mechanisms inherent to living cells.

4.6 Bibliography

[1] D. E. Ingber, «Mechanobiology and diseases of mechanotransduction», *Annals of Medicine*, vol. 35, fasc. 8, pp. 564–577, 2003.

[2] D. E. Jaalouk e J. Lammerding, «Mechanotransduction gone awry», *Nature Reviews Molecular Cell Biology*, vol. 10, fasc. 1, pp. 63–73, 2009.

[3] C.-R. Hsia, D. P. Melters, e Y. Dalal, «The Force is Strong with This Epigenome: Chromatin Structure and Mechanobiology», *Journal of Molecular Biology*, vol. 435, fasc. 11, p. 168019, giu. 2023, doi: 10.1016/j.jmb.2023.168019.

[4] N. Eijkelkamp, K. Quick, e J. N. Wood, «Transient receptor potential channels and mechanosensation», *Annual Review of Neuroscience*, vol. 36, pp. 519–546, 2013.

[5] S. Feliciangeli, F. C. Chatelain, D. Bichet, e F. Lesage, «The family of K2P channels: salient structural and functional properties», *Journal of Physiology*, vol. 593, fasc. 12, pp. 2587–2603, 2015.

[6] E. R. Schneider, E. O. Anderson, E. O. Gracheva, e S. N. Bagriantsev, «Temperature sensitivity of two-pore (K2P) potassium channels», *Current Topics in Membranes*, vol. 74, pp. 113–133, 2014.

[7] B. Coste, J. Mathur, M. Schmidt, T. J. Earley, S. Ranade, e M. J. Petrus, «Piezo1 and Piezo2 are essential components of distinct mechanically activated cation channels», *Science*, vol. 330, fasc. 6000, pp. 55–60, 2010.

[8] X.-Z. Fang *et al.*, «Structure, kinetic properties and biological function of mechanosensitive Piezo channels», *Cell Biosci*, vol. 11, fasc. 1, p. 13, gen. 2021, doi: 10.1186/s13578-020-00522-z.

[9] K. Saotome, S. E. Murthy, J. M. Kefauver, T. Whitwam, A. Patapoutian, e A. B. Ward, «Structure of the mechanically activated ion channel Piezo1», *Nature*, vol. 554, fasc. 7693, pp. 481–486, 2018.

[10] R. Z. Hill, M. C. Loud, A. E. Dubin, B. Peet, e A. Patapoutian, «PIEZO1 transduces mechanical itch in mice», *Nature*, vol. 607, fasc. 7917, pp. 104–110, 2022.

[11] J. Ge, W. Li, Q. Zhao, N. Li, M. Chen, e P. Zhi, «Architecture of the mammalian mechanosensitive Piezo1 channel», *Nature*, vol. 527, fasc. 7576, pp. 64–69, 2015.

[12] Y. R. Guo e R. MacKinnon, «Structure-based membrane dome mechanism for Piezo mechanosensitivity», *eLife*, vol. 6:e33660, 2017.

[13] Y. Wang, S. Chi, H. Guo, G. Li, L. Wang, e Q. Zhao, «A lever-like transduction pathway for long-distance chemical- and mechano-gating of the mechanosensitive Piezo1 channel», *Nature Communications*, vol. 9, fasc. 1, 2018.

[14] L. Wang, H. Zhou, M. Zhang, W. Liu, T. Deng, e Q. Zhao, «Structure and mechanogating of the mammalian tactile channel PIEZO2», *Nature*, vol. 573, fasc. 7773, pp. 225–229, 2019.

[15] F. J. Taberner, V. Prato, I. Schaefer, K. Schrenk-Siemens, P. A. Heppenstall, e S. G. Lechner, «Structure-guided examination of the mechanogating mechanism of Piezo2», *Proc Natl Acad Sci U S A*, vol. 116, fasc. 28, pp. 14260–9, 2019.

[16] Y. C. Lin, Y. R. Guo, A. Miyagi, J. Levring, R. MacKinnon, e S. Scheuring, «Force-induced conformational changes in PIEZO1», *Nature*, vol. 573, fasc. 7773, pp. 230–234, 2019.

[17] R. R. Resende, L. M. Andrade, A. G. Oliveira, E. S. Guimarães, S. Guatimosim, e M. F. Leite, «Nucleoplasmic calcium signaling and cell proliferation», *Cell Communication and Signaling*, vol. 11, fasc. 14, 2013.

[18] R. J. Gasperini, M. Pavez, A. C. Thompson, C. B. Mitchell, H. Hardy, e K. M. Young, «How does calcium interact with the cytoskeleton to regulate growth cone motility during axon pathfinding?», *Molecular and Cellular Neuroscience*, vol. 84, pp. 29–35, 2017.

[19] K. L. Lankford e P. C. Letourneau, «Evidence that calcium may control neurite outgrowth by regulating the stability of actin filaments», *Journal of Cell Biology*, vol. 109, fasc. 3, pp. 1229–1243, 1989.
[20] E. Robles, A. Huttenlocher, e T. M. Gomez, «Filopodial calcium transients regulate growth cone motility and guidance through local activation of calpain», *Neuron*, vol. 38, fasc. 4, pp. 597–609, 2003.
[21] W. M. Botello-Smith, W. Jiang, H. Zhang, A. D. Ozkan, Y. C. Lin, e C. N. Pham, «A mechanism for the activation of the mechanosensitive Piezo1 channel by the small molecule Yoda1», *Nature Communications*, vol. 10, fasc. 4503, 2019.
[22] R. Gnanasambandam, C. Ghatak, A. Yasmann, K. Nishizawa, F. Sachs, e A. S. Ladokhin, «GsMTx4: mechanism of inhibiting mechanosensitive ion channels», *Biophysical Journal*, vol. 112, fasc. 1, pp. 31–45, 2017.
[23] H. Abuwarda e M. M. Pathak, «Mechanobiology of neural development», *Current Opinion in Cell Biology*, vol. 66, pp. 104–111, 2020.
[24] D. E. Koser, A. J. Thompson, S. K. Foster, A. Dwivedy, E. K. Pillai, e G. K. Sheridan, «Mechanosensing is critical for axon growth in the developing brain», *Nature Neuroscience*, vol. 19, fasc. 12, pp. 1592–1598, 2016.
[25] M. M. Pathak, J. L. Nourse, T. Tran, J. Hwe, J. Arulmoli, e D. T. Le, «Stretch-activated ion channel Piezo1 directs lineage choice in human neural stem cells», *Proceedings of the National Academy of Sciences USA*, vol. 111, fasc. 45, pp. 16148–16153, 2014.
[26] F. M. Watt e W. T. S. Huck, «Role of the extracellular matrix in regulating stem cell fate», *Nature Reviews Molecular Cell Biology*, vol. 14, fasc. 8, pp. 467–473, 2013.
[27] S. Ivkovic, T. Major, M. Mitic, N. Loncarevic-Vasiljkovic, M. Jovic, e M. Adzic, «Fatty acids as biomodulators of Piezo1-mediated glial mechanosensitivity in Alzheimer's disease», *Life Sciences*, vol. 297, fasc. 120470, 2022.
[28] M. Velasco-Estevez, N. Koch, I. Klejbor, F. Caratis, e A. Rutkowska, «Mechanoreceptor Piezo1 is downregulated in multiple sclerosis brain and is involved in the maturation and migration of oligodendrocytes in vitro», *Frontiers in Cellular Neuroscience*, vol. 16, fasc. 914985, 2022.
[29] J. Hu, Q. Chen, H. Zhu, L. Hou, W. Liu, e Q. Yang, «Microglial Piezo1 senses Aβ fibril stiffness to restrict Alzheimer's disease», *Neuron*, vol. 111, fasc. 1, pp. 15–29, 2023.
[30] M. M. Maneshi, B. Maki, R. Gnanasambandam, S. Belin, G. K. Popescu, e F. Sachs, «Enantiomeric Aβ peptides inhibit the fluid shear stress response of PIEZO1», *Scientific Reports*, vol. 8, fasc. 14267, 2018.
[31] M. P. Lambert *et al.*, «Vaccination with soluble Aβ oligomers generates toxicity-neutralizing antibodies», *Journal of Neurochemistry*, vol. 79, fasc. 3, pp. 595–605, nov. 2001, doi: 10.1046/j.1471-4159.2001.00592.x.

5

Poroelasticity

5.1 Introduction

The field of cell mechanics and mechanobiology has seen immense growth over the last three decades and still is growing at an amazing pace.

The growing recognition of the role of physics in determining cellular responses has made it necessary to revise the classical biochemical paradigm of cell signaling, which traditionally describes a molecule binding to a receptor and initiating a downstream signaling cascade that leads to specific cellular outcomes. Today, it is also essential to consider how mechanical forces influence and modulate these pathways. This updated perspective can be described as the "mechanochemical paradigm", in which cells integrate both chemical and mechanical cues to regulate their behavior. A prominent example of this concept is stem cell differentiation, where the outcome is governed not only by biochemical differentiation factors but also by the mechanical properties of the extracellular environment [1].

The main mechanisms for cellular force generation are polymerization of cytoskeletal filaments: actin filaments, intermediate filaments and microtubules [2].

The cytoskeleton, a network of filamentous polymers, confers structural integrity to cells and regulates essential biological function in the cells' mechanically dynamic environment, e.g., motility, "growing into" the environment, and lineage commitment (*figure 5-1*).

Each element of the cytoskeletal network performs unique mechanical roles which coordinate to enable integrative cellular function. Forces associated to microtubules are mainly invested in splitting the genome during cell division. Conversely, the forces associated to the actin cytoskeleton are mostly used for matrix remodelling and morphological changes of the cell, especially during cell migration. Various actuators are critical in force generation by the actin cytoskeleton, particularly actin polymerization and myosin II-based contraction.

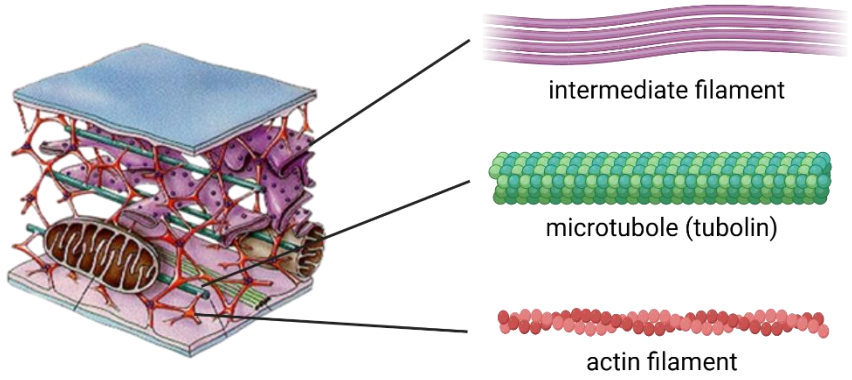

Figure 5-1: Schematics of the cytosolic structure and the principal components of the cytoskeleton: actin filaments, microtubules, and intermediate filaments. Modified from https://rsscience.com/cytoskeleton/

Of all cytoskeletal filaments, only actin and microtubules are polar, i.e., they polymerize at one end and depolymerize at the other, which imparts directionality (necessary for vector function in a physics context) to their behaviour. Combined with this polarity, the changing length of actin provides contractility and tension-sensing capacity to cells [3].
There are different ways to gauge the cell mechanical properties and their variation after an extracellular stimulus.
If we consider a cell as a soft material, to characterize its mechanics we can investigate its elasticity, that is regulated by a cytoskeleton remodelling [2].
The elasticity of the cell is generally characterised by its elastic modulus, which is the stress (force per unit area) necessary to induce a given strain (deformation).
Cells exhibit a range of elastic modulus on the order of 0.1–20 kPa, depending on their source (e.g., cancer cell lines, which are softer), cytoskeletal characteristics [4] and alteration due to pathologies. For instance, different studies have reported that cancer cells show a softer mechanical phenotype in comparison to healthy ones and that actin filaments are the major determinant of cell mechanical properties [5-6].

We can adopt a more refined approach by applying a viscoelastic model that takes into account both the elastic and the viscous components.
Unlike purely elastic solid materials, cells exhibit diverse mechanical behaviours with properties of both solids and liquids [7-8]. Solid elastic materials deform instantly when subjected to a force and maintain a constant deformation as long as the force is applied, exhibiting time-independent behaviour. In contrast, liquid viscous materials undergo continuous and irreversible deformation when subjected to a force. Viscoelastic materials exhibit a response that lies between these two extremes. As viscoelastic materials, biological tissues initially respond elastically to a force and then undergo continuous viscous deformation. In particular we have these two time-dependent behaviours:

Stress relaxation: refers to the response of a viscoelastic material to a constant strain in which the internal stress of the material gradually decreases over time at a constant environmental temperature. During this process the molecular chains tend to move in the direction of deformation force to diminish or quench the internal stress.

Creep: is defined as the time-dependent response to a constant mechanical stress.
A viscoelastic material tends to undergo slow deformation when subjected to a small and persistent stress under a constant temperature. The time scale of creep is dependent on the magnitude of the force. This property of cells and tissues allows them to adjust their deformation under prolonged load.

However, viscoelastic models have limitations in fully explaining cellular responses, as they do not account for the movement of fluid within the cell.

In terms of weight and volume, water is indisputably the major component of soft biological tissues. The mechanical property most commonly associated with the presence of water is near volume constancy, i.e., incompressibility, based on the fact that the compression modulus of water is orders of magnitude larger than the distortional

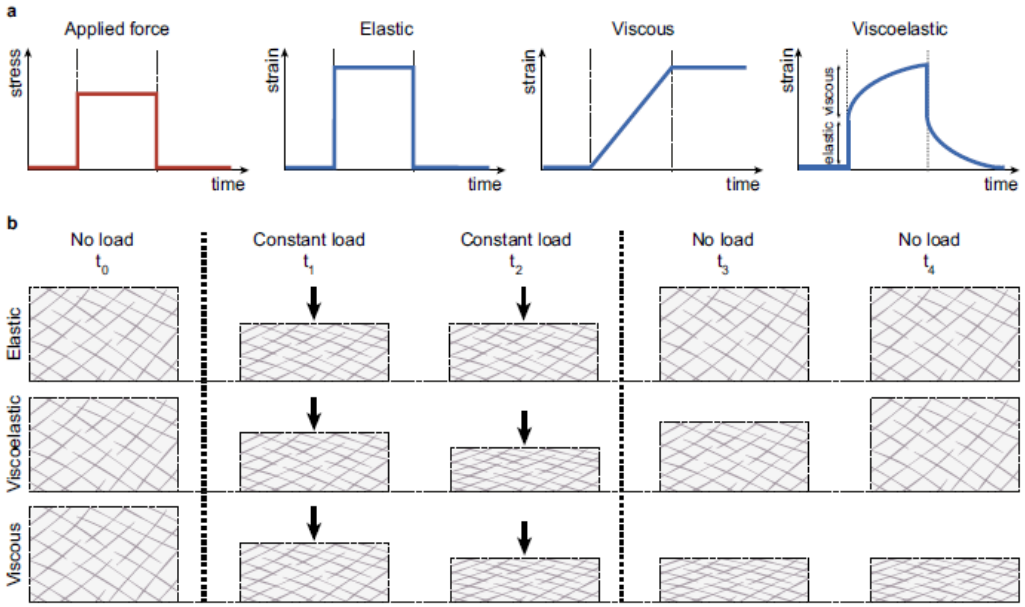

Figure 5-2: (a) The strain response to a stress stimulus by three different ideal materials. Under a constant applied force, purely elastic materials deform instantaneously and maintain this deformation until the load is removed, at which point they immediately return to their original shape. In contrast, purely viscous materials undergo continuous deformation over time. Viscoelastic materials exhibit an initial instantaneous response to the applied force (elastic component), followed by a time-dependent increase in deformation associated with the viscous component.
(b) Under a constant applied force (black arrows), the deformation of a purely elastic matrix is time-independent: the matrix deforms instantaneously and returns to its initial shape when the force is applied and removed, respectively (top). In contrast, the response of viscoelastic matrices is time-dependent: under a constant load, deformation increases over time, and the material does not immediately return to its original shape once the load is removed (middle). Purely viscous matrices undergo continuous deformation under the applied force and retain their deformed shape after the force is removed (bottom) [8].

stiffness of tissues [7]. The vast majority of biomechanical studies on soft collagenous tissues is based on this assumption [8], typically without experimental verification of its validity. While this assumption implies that all the interstitial fluid is immobile and bound to the tissue, other biomechanical analyses build, vice-versa, on the mobility of the liquid phase in a porous matrix, driven by spatial pressure gradients. The role of water in such biphasic or porous media representations thus lies in that it furnishes the tissue with time-dependent characteristics governed by the chemical and physical properties of fluid and solid phase [9] (*figure 5-2*).

Poroelasticity is an alternative approach to model the cell system that take in account the movement of a viscous fluid within a solid and porous an elastic matrix.

The Poroelastic Theory

Maurice Biot is considered the father of poroelasticity. He first introduced the theory in 1941 to describe the mechanical behaviour of fluid-saturated porous materials[10]). Biot's theory integrated classical elasticity with fluid flow dynamics, to address how fluids interact with the solid matrix in materials like soil and rock. By the late 20th century, advancements in computational modelling enabled its application to a broader range of materials, including biological tissues. Today, the poroelastic model plays a crucial role in understanding the mechanical behaviour of soft biological tissues, such as cartilage and brain tissue, and is widely applied in tissue engineering, particularly in studying the deformation, diffusion, and mechanical properties of cells, including stem cells used in regenerative medicine.

In this thesis the rheological properties of cell and its variation due to alterations of its cytoskeletal organization is studied applying the poroelastic model as principal method of investigation.

This model conceptualizes the cytoplasm as a biphasic material (*figure 5-3*), composed of a porous elastic solid meshwork (primarily the cytoskeleton, organelles, and large macromolecules) that is immersed in an interstitial fluid (the cytosol). This biphasic nature reflects the dual roles of the cytoskeleton, which provides structural integrity and mechanical stiffness, and the cytosol, which allows for fluid flow and redistribution of forces.

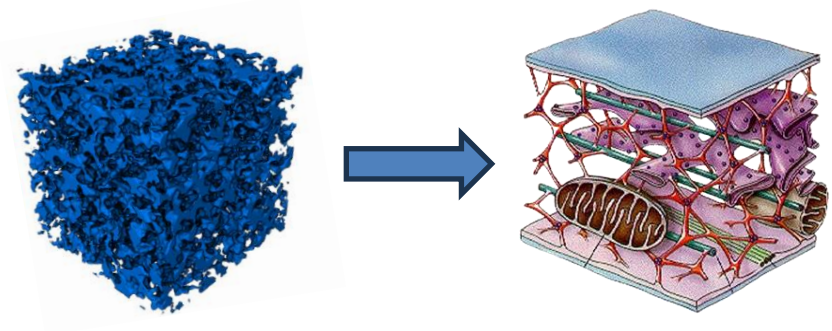

Figure 5-3: Schematic illustration of a poroelastic mesh model mimicking the cellular structure Modified from https://rsscience.com/cytoskeleton/.

According to the poroelastic model, the deformation of the cell in response to mechanical forces is governed by the poroelastic diffusion constant D_p. By assuming the cell to be a linear and isotropic material it is possible to obtain an analytic expression of the constant as follows:

$$D_p = \left(\frac{(1-\nu_s)}{(1+\nu_s)(1-2\nu_s)}\frac{\varphi}{4\kappa}\right)\frac{E\xi^2}{\mu}$$

With ϕ the porosity, ξ the average radius of pores, μ the viscosity of the fluid, ν Poisson's ratio and κ a constant taking into account irregularity, interconnectivity and tortuosity of pores [11] (*Figure 5-4 [11]*). If we can consider the term between the parentheses as a constant then we obtain the following simple scaling law:

$$D_p = \alpha\frac{E\xi^2}{\mu}$$

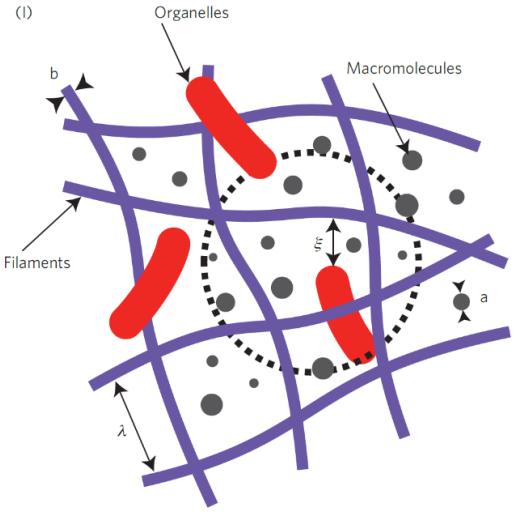

Figure 5-4: Schematic representation of the cytoplasm. (I) The cytoskeleton and macromolecular crowding participate in setting the hydraulic pore size through which water and solutes can diffuse. The length scales involved in setting cellular rheology are the average filament diameter b, the size a of particles in the cytosol, the hydraulic pore size ξ, and the entanglement length λ of the cytoskeleton.

This law shows that the larger the value of the poroelastic diffusion constant, the more rapidly the cell can dissipate mechanical stresses, leading to faster shape changes and stress relaxation [11].

The maximal rate at which the cytoplasm can deform, therefore, is determined by the redistribution time of intercellular water within the cytoplasm. As water moves through the porous cytoskeletal mesh, it redistributes internal pressures and facilitates deformation [12].

This model also explains how cells internally manage their mechanical environment, thus by studying these properties through the lens of poroelasticity, we gain valuable insights into how cells interpret and adapt to mechanical stimuli from their environment [13].
This approach is consistent with experimental observations of cellular rheology. For instance, it has been shown that when cells experience localized deformation, such as being indented by an AFM tip, the internal pressure within the cell equilibrates through the redistribution of intracellular fluid. And this is exactly the phenomenon that has been observed for the estimation of the poroelastic diffusion constant.

AFM-Based Stress Relaxation and Poroelasticity

Most methods to investigate cell mechanics rely on sample deformation via the application of stress in direct contact [14]. These include the use of optical and magnetic tweezers, magnetic twisting cytometry, micropipette aspiration, parallel plate rheometry, and atomic force microscopy (AFM). Noncontact methods include particle tracking microrheology, optical stretching, microfluidic deformability cytometry and Brillouin Microscopy.

Atomic force microscopy is the most often used technique, as it enables measurements of both local and global cell mechanics, in combination with other microscopic techniques and chemical modifications. The position of the cantilever is tightly controlled by a feedback circuit that enables to apply a mechanical stress with control on the nanometer, piconewton, and millisecond scale.
Amongst all AFM-based methods, the most common one consists in acquiring force-distance curves (FDCs), either on a single point of the sample surface or on a whole surface by performing spatially resolved mapping (*i.e*. force volume). These curves are constructed by recording the force when the tip moves towards the sample surface (approach curve) and withdrawing from the surface (retraction curve). AFM cantilevers

with cylindrical, conical (or pyramidal) and parabolic (or spherical) probes are commonly used to perform such force spectroscopy experiments that can directly be carried out on fully hydrated hydrogels or living cells in biological buffers. Another approach is using colloidal probes to vary the geometry and chemico-physical properties of the indenter.

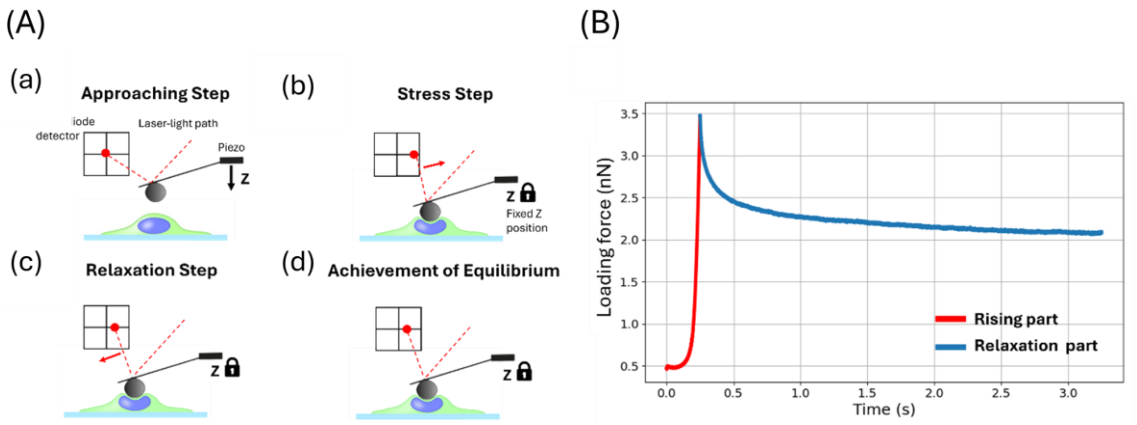

Figure 5-5: (A) Cartoon of the AFM-based stress relaxation curve. After the first phase of approaching (a), the AFM tip -functionalized with a colloidal probe of radius 10 um- indent the sample until reaching the force setpoint (b). The piezo position is fixed in order to follow the tip deflection minimization, that is characteristic of the relaxation process (c). After few seconds the system reaches an equilibrium state corresponding to the plateau of the force-time curve (d). (B) Example of an experimental stress-relaxation curve, where we distinguish the rising part in red and the relaxation part in blu.

In order to investigate the cell time-dependent response to the stress, we can apply a constant stress (a creep curve) or a constant strain (a stress relaxation curve).

In this thesis we consider especially the AFM-based stress relaxation curves (*Figure 5-5*). At smaller time-scales (10^{-3}-10^{-1} s) [11-15] the strain induces a redistribution of the cytosol into the inner compartments of the cell highlighting the poroelastic behaviour of the cell or biomaterial, while at larger time-scales the viscoelastic properties of the sample drive the response of the sample.

Considering the stress-relaxation curve acquired through the AFM, we can fit the initial relaxation part to get information about the rheology of the cell using the poroelastic model.

5.2 Mechanical Characterization of ADLD Pathology

In the introduction, Laminopathies and ADLD were described as rare neurodegenerative disorders characterized by profound alterations in the organization of the nuclear lamina. Although their genetic bases are increasingly well understood, the consequences of these pathologies on nuclear and cellular mechanics remain only partially explored as the link between mechanical alteration and the progression of disease.

Previous studies investigated the mechanical properties of nuclei extracted from ADLD cells using atomic force microscopy (AFM), revealing a slight, although significant, increase in isolated nuclei stiffness compared to healthy controls [16-17] (*figure 5-6*). While these findings suggest that the disease directly affects the mechanical integrity of the nucleus, interpreting such results is not straightforward.

Measuring nuclear mechanics is intrinsically challenging because the nucleus in living cells is embedded within the cytoplasm and mechanically coupled to the cytoskeleton through the LINC complex and various nucleoskeletal elements. These interactions play a crucial

role in determining both the passive mechanical response of the nucleus and its ability to adapt dynamically to mechanical stimuli.

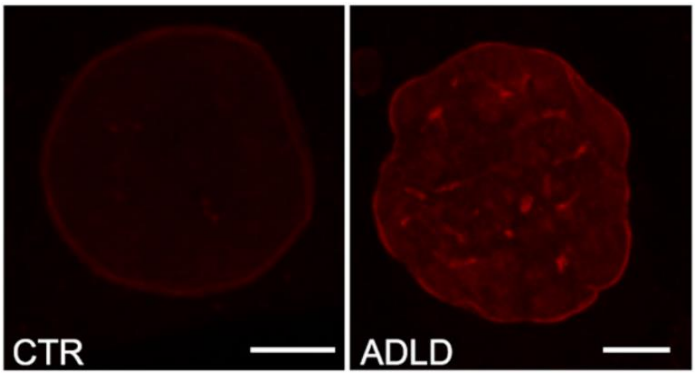

Figure 5-6: Confocal images of nuclear lamin B1 in a control cell and an ADLD cell [1]. Scale bar: 5 µm.

Isolating the nucleus through extraction protocols provides a way to probe its mechanical properties although a series of alterations can arise such as the lack of interaction with nucleoskeletal elements, the drastic alteration of the nuclear microenvironment through the loss of colloid osmotic balance and the exposure to chemical agents. It is reasonable to think that these deviations from the physiological environment would induce changes in nuclear mechanical properties that do not fully reflect the in vivo situation. Consequently, some of the mechanical differences attributed to the pathology could be partially modulated or amplified/suppressed by the extraction process itself.

For these reasons, studying nuclear mechanics in intact, living cells is essential to obtain a more physiologically relevant picture of how laminopathic mutations influence the mechanical behaviour of the nucleus.

Traditionally, cellular mechanics have been assessed by measuring the Young's modulus, often considered the primary descriptor of the cell's elastic response. Although this approach is well established, the intrinsic complexity of the cellular environment makes both the estimation of the Young's modulus and the choice of an appropriate mechanical model far from trivial. The heterogeneous composition of the cell combined with its active and viscoelastic nature, leads to substantial variability in this parameter.

In this project, I therefore shifted the focus toward a different dimension of cell mechanics: cell rheology. By analysing how cells respond to time-dependent mechanical perturbations, modelling the cell as a poroelastic material. The goal of this approach is to identify an additional, more robust mechanical biomarker that may better reflect the alterations induced by laminopathic mutations and contribute to a deeper understanding of this pathology. Furthermore, as a complementary approach, Brillouin micro-elastography, introduced in the methodological chapter, was employed to determine the elastic properties of the cells.

This work was carried out in collaboration with the biophysics groups of IOM-CNR and the University of Perugia, led by Dr. Silvia Caponi and Prof. Maurizio Mattarelli, with the valuable contribution of Alessandra Passeri for the BLS measurements, and with the medical research group led by Prof. Stefano Ratti at the Department of Neurology, University of Bologna.

Together, we integrated AFM and BS as primary and complementary investigative techniques. The combination of these two methods provides a multimodal mechanical readout: AFM probes the poroelastic response at the nanoscale through contact mechanics, while Brillouin Spectroscopy enables label-free, all-optical mapping of intracellular mechanical properties. This multimethod approach offers a more complete and physiologically relevant characterization of nuclear mechanics in living cells.

Moreover, the mechanotransduction properties of pathological cells were investigated using the custom-made setup for the detection of intracellular calcium level variation under mechanical stress conditions described in the previous section.

5.3 Materials and Methods

Cell culture

Human dermal fibroblasts (HDFa, ThermoFisher, C0135C) were cultured in flasks using Dulbecco's Modified Eagle Medium (DMEM, Sigma-Aldrich, USA) supplemented with 10% fetal bovine serum (FBS), 2 mM glutamine, and 100 IU/mL penicillin–streptomycin (Sigma-Aldrich, St. Louis, MO, USA). Cells were maintained at 37 °C in a standard incubator under 5% CO_2. Upon reaching confluency, cultures were split and expanded into new flasks, ensuring that no more than 16 passages were performed.

For mechanical measurements, cells were seeded at low density onto poly-L-lysine–coated (20 µg/mL) Petri dishes (TPP Techno Plastic Products, Switzerland) to prevent overlap between cells. Before AFM experiments, the samples were washed twice with Dulbecco's Phosphate-Buffered Saline (DPBS, Sigma-Aldrich, USA) supplemented with calcium and magnesium (Sigma-Aldrich D8662).

AFM-Based Relaxation Measurement

AFM experiments were conducted in PBS buffer, with the sample temperature maintained at 37 °C using a Petri dish heater. To minimize potential biases associated with prolonged exposure of the cells to ambient conditions, the total experimental duration for each dish was kept below two hours.

To verify the independence of D_p by the presence of the nucleus in the region where the stress-relaxation curves were done, I made six curves for each cell analyzed, three curves on the nucleus, and six curves on the cytoplasm as show in *figure 5-7*.

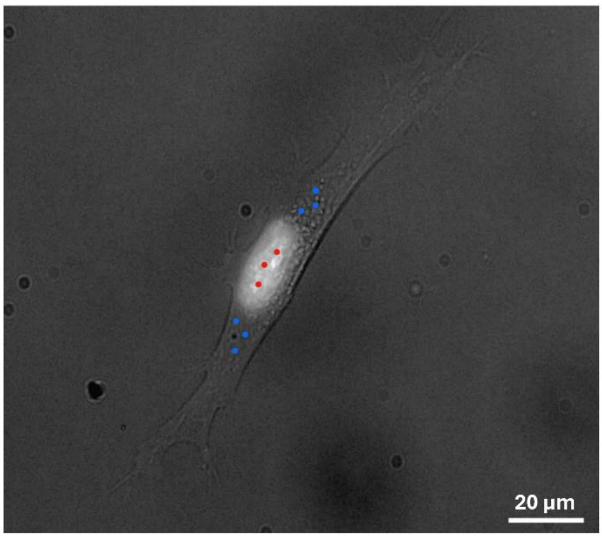

Figure 5-7: Bright-field image of an ADLD cell during AFM measurements. The cell nucleus was stained with Hoechst to identify the nuclear region. The points selected for acquiring stress–relaxation curves are highlighted.

The stress relaxation experiment was performed using an atomic force microscope JPK Nanowizard IV from Bruker, coupled with a DMi8 inverted optical microscope from Leica. The JPK software allows for optical calibration of the AFM region of interest. This enables us to obtain an optical image of the cell and then choose the point at which to make the measurement, with sufficient precision to distinguish the region above the nucleus from areas where it is absent.

We used an AFM probe (DNP-10, Bruker) with elastic constant k = 0.06 N/m attaching a latex bead of radius R = 5 μm at the end of the cantilever.

To detect the relaxation process due to water redistribution, the force setpoint must be reached in a time shorter than the characteristic timescale of the process. Given that D_p is in the range of 1-100 $\mu m^2/s$ and the scale of the deformation could be considered $L^2 \approx R\delta$, the characteristic time of fluid redistribution is $t_p \approx 0.2$-20 s. Therefore, we chose a rise time of 30 ms.

The duration of the force-distance curve was selected to ensure that the final plateau in the force-time curves is reached.

Varying the applied force, we obtained indentation close to 1 μm. We avoid larger indentation to avoid undesired effects due to the interaction with the rigid substrate.

We analyzed the stress-relaxation curves, fitting the data using the approximate solution obtained by the finite-element simulations [11]:

$$\frac{F(t) - F_f}{F_i - F_f} = 0.491e^{-0.908\sqrt{\tau}} - 0.509e^{-1.679\tau}, \qquad \tau = D_p t/R\delta$$

The initial 0.5 seconds of the relaxation phase were fitted, during which the relaxation process is more accurately described by the poroelastic model [18].

An example of an analysed curve is shown in *figure 5-8*.

From this fit, the poroelastic diffusion coefficient (Dp) was extracted, serving as the key quantitative parameter describing the poroelastic behaviour of the cell.

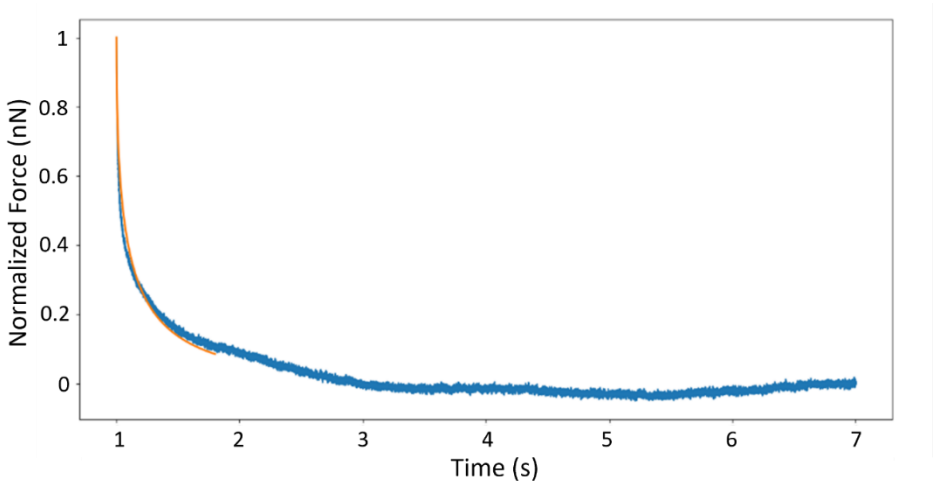

Figure 5-8: Relaxation phase of a stress–relaxation curve fitted with the poroelastic model within the selected time window.

BLS Measurements

In the adopted configuration, the excitation source is a diode-pumped solid-state green laser (Spectra-Physics Excelsior, 532 nm). The beam first passes through a temperature-controlled etalon (TCF-1, JRS Scientific Instruments Tablestable Ltd., Mettmenstetten, Switzerland), specifically designed to suppress unwanted secondary laser modes within the spectral region relevant for Brillouin spectroscopy. After mode filtering, the beam is directed into a confocal optical path (JRS Scientific Instruments) before reaching a corner-cube beam splitter.

The beam splitter sends a fraction of the light to the reference input of the TFP-2 Brillouin interferometer, enabling self-tuning and long-term spectral stability. This reference channel is essential in backscattering configurations, where the strong elastic peak could otherwise saturate or damage the photon-counting detector. During the acquisition of the inelastic Brillouin peaks, the elastic component is therefore blocked using a shutter system integrated into the control electronics, while the reference beam maintains interferometer stabilization.

The remaining portion of the beam is delivered to the sample through a confocal microscope equipped with a water-immersion objective (NA = 1.2). The sample itself is mounted on a high-voltage piezoelectric translation stage with a 100 µm travel range per axis and nanometric (≈1 nm) positioning resolution. After interacting with the sample, the backscattered light is collected by the same objective and routed to a wavelength-selection module.

A tunable ultra-steep short-pass filter (TEF, Semrock SP01-561RU) separates the frequency components of the scattered light, directing the quasi-elastic Brillouin signal toward the tandem Fabry–Perot interferometer (TFP-2 HC, JRS Scientific Instruments).

Calcium Imaging Measurement

To investigate calcium signalling induced by mechanical stimulation, the same correlative AFM–fluorescence setup described in the previous section was used. ADLD and CLT cells were plated onto 35-mm glass-bottom Petri dishes (WPI, Worcester, MA, USA), which provide optimal optical transparency and are well suited for high-resolution fluorescence imaging. After two days of incubation, the cells were stained with the calcium-sensitive dye Oregon Green BAPTA-1 5 µM (Invitrogen, Thermo Fisher Scientific) and incubated for 45 minutes in PBS.

A cantilever with a nominal elastic constant of 2 N/m functionalized with a polystyrene bead of 5 µm radius (Polysciences, USA) was used to apply mechanical stimuli to the cell. The probe preparation protocol is described in the previous chapter.

The mechanical stimulation was configured with a force setpoint of 400 nN applied for 1.0 seconds and an approach velocity of 30 µm/s.

5.4 Results

In the phase-contrast images in *figure 5-9*, the morphology of ADLD and CTL cells is shown, along with the cell density at the time of AFM measurements. A confluence of approximately 70% was selected as an optimal condition to analyse single-cell

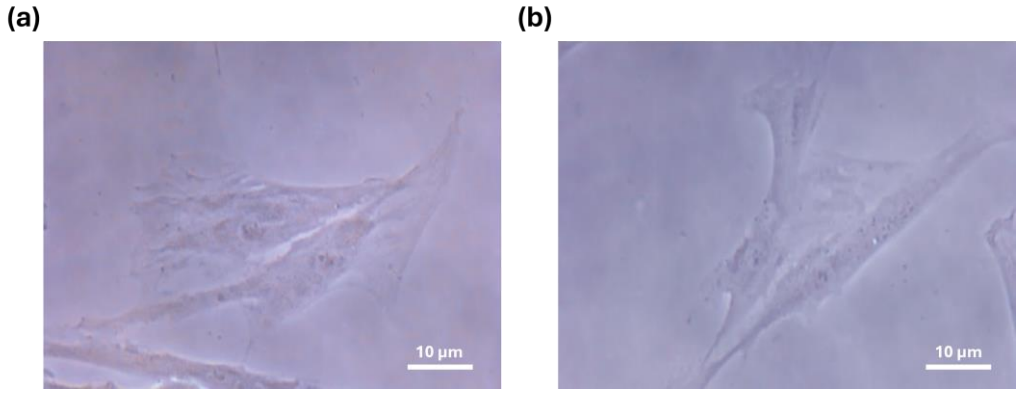

Figure 5-9:Bright-field image of (a) Control cells and (b) ADLD cells during the Brillouin measurements.

mechanical properties, ensuring sufficient cell adhesion and normal morphology while avoiding artefacts associated with overly sparse or overly confluent cultures.

Evaluation of D_p in ADLD and healthy control cells

To obtain a robust estimate of D_p, six independent stress–relaxation curves were acquired over the cytoplasmic region and three additional curves over the nuclear region of each cell. Analysing the datasets corresponding to the cytoplasm and the nucleus separately allows one to resolve and compare differences in their respective rheological behaviours.

Stress-relaxation measurements were conducted on 90 ADLD cells, evaluating both the nuclear and cytoplasmic compartments, and on 50 CTL cells, spanning four different cell passages. The resulting values of the poroelastic diffusion coefficient D_p are reported in the boxplot shown in *figure 5-10*.

The comparative analysis of the results obtained reveals a significant increase in D_p in ADLD cells in both the nuclear and cytoplasmic regions. For CTL cells, the recorded mean D_p value in the cytoplasmic and nuclear compartments was (23 ± 8) $\mu m^2/s$ and (20 ± 6) $\mu m^2/s$, respectively. In contrast, ADLD cells exhibited markedly higher values, with (43 ± 13) $\mu m^2/s$ in the cytoplasmic region and (39 ± 10) $\mu m^2/s$ in the nuclear region (Mean ± SD). The data distributions corresponding to the stress–relaxation curves acquired in the cytoplasmic and nuclear compartments of the same cell group do not show significant differences. This indicates that the cytosol redistribution dynamics are not confined to a specific subcellular region but instead represent a global mechanical property of the entire cell system. This observation is consistent with previous findings reported for HeLa and MDCK cell lines [11], where similar poroelastic responses were observed across different cellular regions, reinforcing the notion that poroelasticity emerges as a whole-cell mechanical phenotype rather than a compartment-specific characteristic.

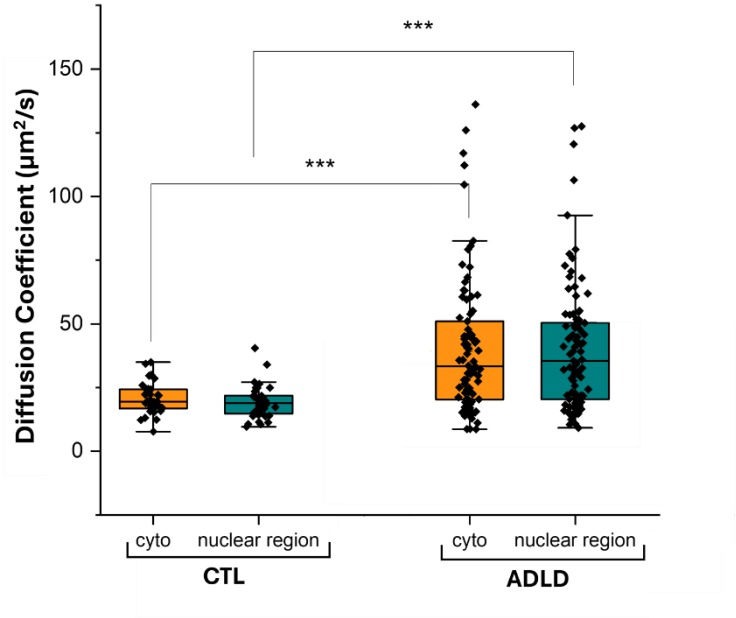

Figure 5-10: Boxplot of the AFM-based stress–relaxation results comparing the curves acquired in the nuclear and cytoplasmic compartments of control and ADLD cells. Welch's one-way ANOVA was performed to assess statistical significance between the distributions.

BLS Results

The Brillouin measurements were performed on 40 cells, separating the nuclear and the cytoplasmatic region.

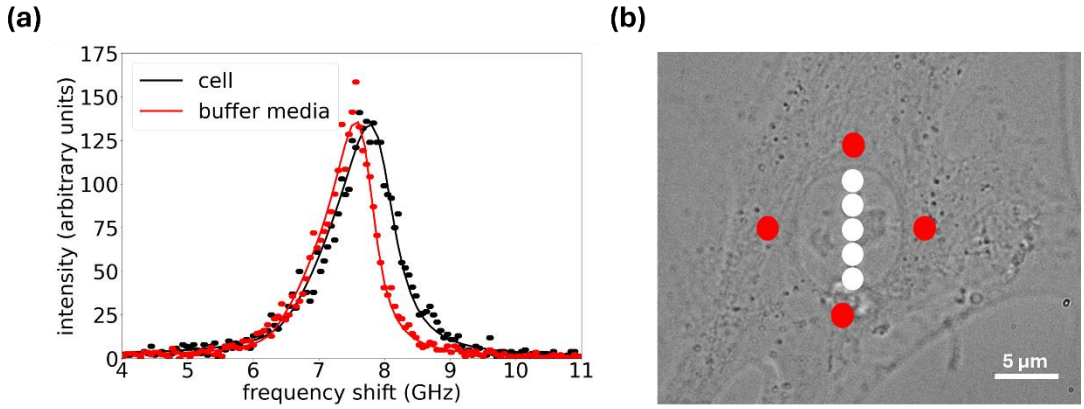

Figure 5-11: (a) Brillouin peak in the buffer medium overlaid with the peak acquired in the cell region. (b) Bright-field image of a cell during the BLS experiment, with the measurement spots highlighted.

The Brillouin spectrum was first acquired in the buffer medium. The laser beam was then focused at a z-position corresponding to the mid-height of the cell, and an x–y field of view including both the nuclear region and the surrounding cytoplasmic area was

selected. Four points within each compartment -the nucleus and the cytoplasm- were chosen for Brillouin spectrum acquisition. The spectra were subsequently analysed and compared with the Brillouin peak measured in the medium to extract the values of ω_B and Γ_B, as shown in *figure 5-11*.

Brillouin maps were then acquired, in which each pixel corresponds to a single Brillouin spectrum. For every pixel, ω_B and Γ_B were extracted through spectral fitting, and the resulting parameter maps were reconstructed (*figure 5-12*).

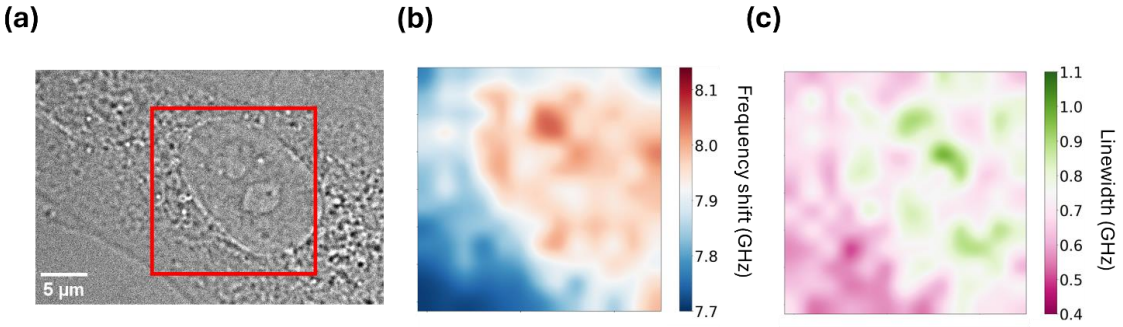

Figure 5-12: (a) Bright-field image of a cell during the BLS experiments, with the region corresponding to the BLS map highlighted. (b–c) Frequency-shift and linewidth maps, respectively, acquired in the highlighted region.

To obtain compartment-specific mechanical descriptors, the average values of ω_B and Γ_B within the nuclear and cytoplasmic regions -excluding boundary interfaces and perinuclear

transition zones- were computed. These average quantities were used as representative Brillouin parameters for each cellular compartment.

Considering the cytoplasmic compartment, BLS measurements reveal a consistent decrease in both frequency shift and linewidth in ADLD cells compared to controls, whereas the values obtained from the nuclear compartment do not exhibit significant differences between the two groups. As outlined in the previous methodological chapter, the Brillouin frequency shift is directly related to the longitudinal elastic modulus of the material; therefore, a lower shift in ADLD cells indicates a reduction in intracellular stiffness. Likewise, the Brillouin linewidth reflects the dissipative modulus and viscous response of the probed region, and its decrease in ADLD cells points to a reduction in cytoplasmic viscosity.

The corresponding results are reported in *figure 5-13*.

The observation that both the elastic and viscous components are reduced in ADLD cells compared to controls, as revealed by Brillouin measurements, can be interpreted as evidence of a global softening of the intracellular environment. A simultaneous decrease

in frequency shift and linewidth indicates that the cytoplasm of ADLD cells is not only less stiff but also less internally damped, suggesting alterations in the structural and dynamical organisation of the cytosol.

The absence of significative variations in the nuclear compartment was unexpected given the strict connection between ADLD pathology and changes in nuclear protein

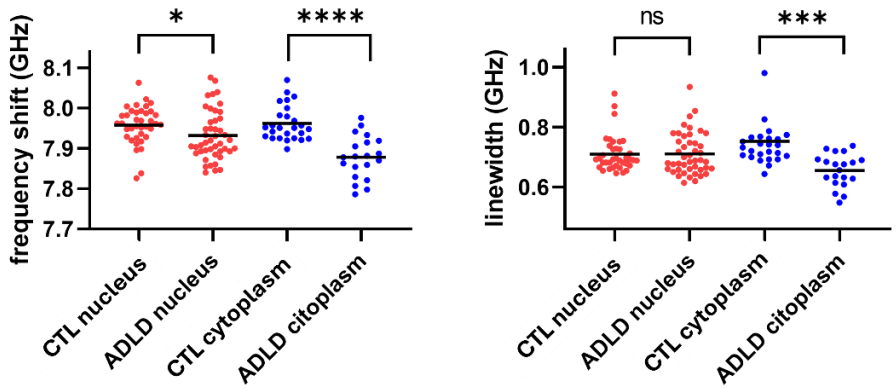

Figure 5-13: Results obtained on CTL and ADLD cells, separated into nuclear and cytoplasmic compartments: (a) ω_B values and (b) Γ_B values.

expression.

Calcium Imaging Results

Calcium imaging experiments were performed on 53 ADLD cells and 43 control cells. Fluorescence intensity was recorded following AFM-induced mechanical stimulation, and the intensity peak preceding the recovery phase was analysed to assess intracellular calcium dynamics. A significant increase in calcium levels was observed in ADLD cells compared to controls (*figure 5-14a*), indicating that the pathological cytoskeletal remodeling directly affects calcium handling.

Quantitatively, the relative increase in calcium levels -considering the peak amplitude- reached an average value of 3.5 ± 2.0 in control cells, compared with 6.0 ± 3.3 (Mean ± SD) in ADLD cells. This nearly two-fold enhancement in peak calcium response suggests an amplified calcium flux in pathological cells, likely reflecting both altered mechanotransduction and modified cytoplasmic organization.

The distribution of the experimental data is illustrated in the boxplot (*figure 5-14b*), highlighting the variability within each group and the consistent trend toward higher calcium peaks in ADLD cells.

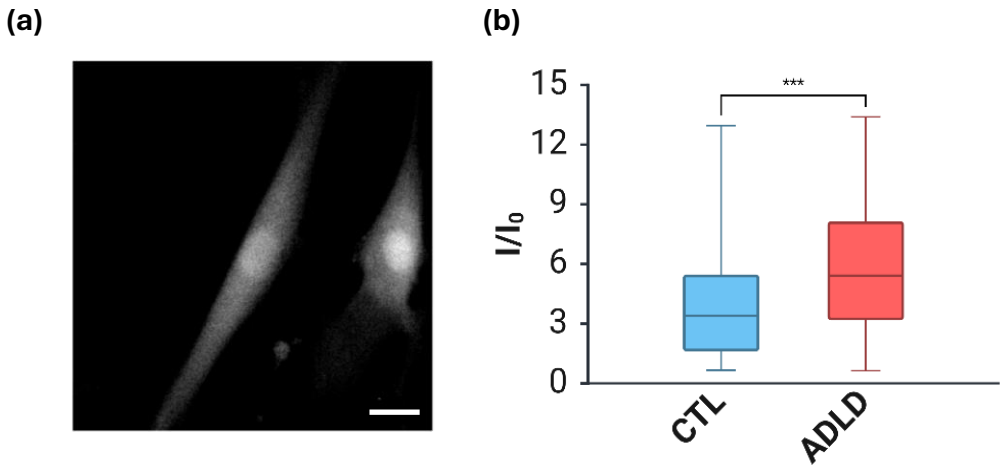

Figure 5-14: (a) Fluorescence image of a cell obtained during calcium imaging experiments, stained with Oregon Green BAPTA-1. (b) Boxplot of the calcium peak distributions acquired in CTL and ADLD cells.

5.5 Conclusions

AFM experiments revealed a global alteration in the rheological properties of ADLD cells compared to healthy controls.

D_p evaluation in ADLD and control (CTL) cells did not reveal any difference when the cell was deformed above the nucleus or in the cytosolic region. Two hypotheses may explain the absence of any nuclear influence on D_p. First, the applied cell deformation might not have been large enough to induce a significant deformation of the nucleus, restricting the analysis to the cytoplasmic region overlying it. Second, the large nuclear pore complexes may permit free water movement across the nuclear membrane, thereby preventing any detectable difference in D_p between the nuclear and cytosolic regions [19].

Upon mechanical stimulation, water redistribution through the cytoplasmic porous network occurred more rapidly in pathological cells. Notably, the increase in the poroelastic diffusion coefficient indicates an enlargement of the effective pore size within the cytoplasmic meshwork, facilitating a higher water flux per unit time and reflecting a more compliant cytoplasmic environment (*figure 5-15a*).

The results obtained through BLS confirm and reinforce this interpretation, showing a reduction in viscoelastic properties consistent with a decrease in cytoskeletal density.

Moreover, BLS experiments further highlighted a compartment-specific mechanical response. While the cytoplasmic compartment exhibited significant variations in

viscoelastic properties, the nuclear compartment remained largely unchanged. This observation suggests that the mechanical alterations associated with ADLD are predominantly localized within the cytoplasm rather than the nucleus.

Taken together, these findings point to cytoskeletal remodeling as a principal mechanical consequence of ADLD. One possible pathway through which Lamin B1 overexpression may influence cytoplasmic organization involves its close functional and structural connection with the LINC (Linker of Nucleoskeleton and Cytoskeleton) complex. The LINC complex provides a physical bridge between the nuclear lamina and the cytoskeletal networks, enabling the transmission of forces and mechanical cues across

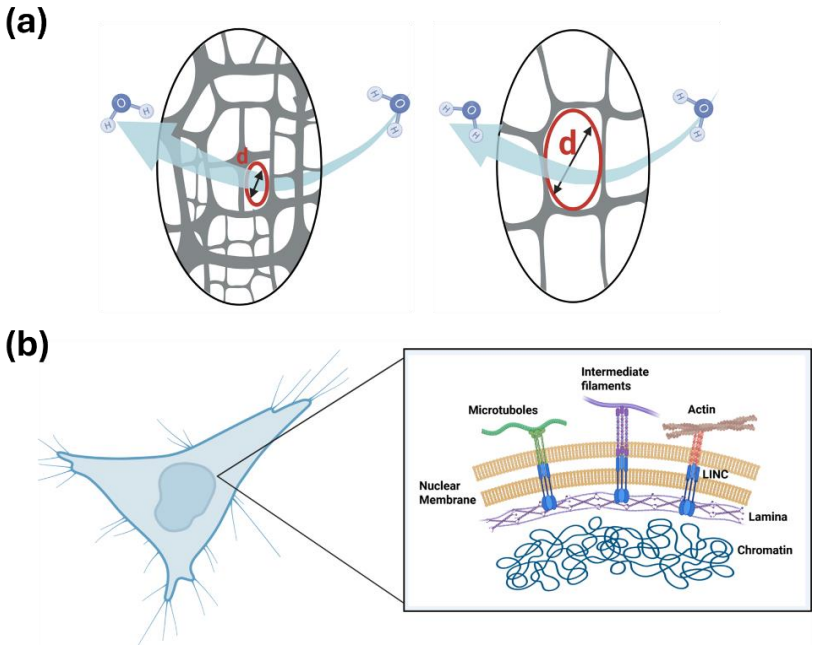

Figure 5-15: (a) Schematic illustrating variations in pore size within the poroelastic matrix and their effect on fluid diffusion. Larger average pore diameters allow faster fluid movement through the material. (b) Schematic showing the connection between the nuclear lamina and the cytoskeleton mediated by the LINC complex.

the nuclear envelope.

Dysregulation of Lamin B1 could therefore alter the mechanical properties and tension at the nuclear envelope, leading to aberrant force transmission through the LINC complex and propagating mechanical imbalances throughout the cell (*figure 5-15b*).

Such perturbations may affect cytoskeletal architecture, cytoplasmic porosity, and intracellular water mobility, ultimately modifying the global mechanical behavior of the cell. This mechanotransductive cascade provides a plausible explanation for the cytoplasmic softening, increased poroelastic diffusion, and altered rheological response observed in ADLD cells.

Calcium imaging experiments provide an additional layer of evidence by linking this mechanical dysregulation to alterations in calcium homeostasis, a process strongly modulated by mechanotransduction. The increased intensity of calcium peaks observed in ADLD cells suggests that cytoskeletal disorganization directly impacts calcium handling, revealing an enhanced calcium exchange under pathological conditions. This convergence of mechanical and metabolic alterations highlights the central role of cytoskeletal integrity in coordinating both mechanotransductive and homeostatic responses and underscores the mechanobiological nature of ADLD pathology.

From a broader perspective, these findings highlight how nuclear alterations can propagate long-range effects across the cell, reinforcing the notion that nuclear–cytoskeletal coupling

is essential for maintaining cellular mechanics and homeostasis. In ADLD, the disruption of this delicate balance appears to impair mechanosensing, compromise intracellular transport, and increase the cell's vulnerability to mechanical stress(*figure 5-16* [20]). Altogether, this mechanobiological dysfunction provides a unifying framework for understanding how Lamin B1 overexpression contributes to the cellular pathology of ADLD.

5.6 Bibliography

[1] A. J. Engler, «Matrix elasticity directs stem cell lineage specification», *Cell*, vol. 126, fasc. 4, pp. 677–689, 2006.

[2] P. Melo, «Mechanical actuators in microglia dynamics and function», *European Journal of Cell Biology*, vol. 101, fasc. 3, p. 151247, 2022.

[3] G. W. Greene, «Force amplification response of actin filaments under confined compression», *Proceedings of the National Academy of Sciences*, vol. 106, fasc. 2, pp. 445–449, 2009.

[4] B. Cheng, «An integrated stochastic model of matrix-stiffness-dependent filopodial dynamics», *Biophysical journal*, vol. 111, fasc. 9, pp. 2051–2061, 2016.

[5] Y. M. Efremov, T. Okajima, e A. Raman, «Measuring viscoelasticity of soft biological samples using atomic force microscopy», *Soft Matter*, vol. 16, fasc. 1, pp. 64–81, 2019.

[6] S. Tavares, «Actin stress fiber organization promotes cell stiffening and proliferation of pre-invasive breast cancer cells», *Nature communications*, vol. 8, fasc. 1, p. 15237, 2017.

[7] R. N. Vaishnav e J. Vossoughi, «Estimation of residual strains in aortic segments», *Biomedical engineering II: recent developments*, pp. 330–333, 1983.

[8] G. Chagnon, M. Rebouah, e D. Favier, «Hyperelastic energy densities for soft biological tissues: a review», *Journal of Elasticity*, vol. 120, fasc. 2, pp. 129–160, 2015.
[9] V. C. Mow, M. H. Holmes, e W. M. Michael Lai, «Fluid transport and mechanical properties of articular cartilage: A review», *J. Biomech*, vol. 17, fasc. 377–394, p. 168019, 2023, doi: 10.1016/0021-9290(84)90031-9gy.
[10] M. A. Biot, «General theory of three-dimensional consolidation», *Journal of applied physics*, vol. 12, fasc. 2, pp. 155–164, 1941.
[11] E. Moeendarbary, «The cytoplasm of living cells behaves as a poroelastic material», *Nature materials*, vol. 12, fasc. 3, pp. 253–261, 2013.
[12] K. Mollaeian, «Atomic force microscopy study revealed velocity-dependence and nonlinearity of nanoscale poroelasticity of eukaryotic cells», *Journal of the mechanical behavior of biomedical materials*, vol. 78, pp. 65–73, 2018.
[13] H. Schillers, M. Wälte, K. Urbanova, e H. Oberleithner, «Real-Time Monitoring of Cell Elasticity Reveals Oscillating Myosin Activity», *Biophysical Journal*, vol. 99, fasc. 11, pp. 3639–3646, dic. 2010, doi: 10.1016/j.bpj.2010.09.048.
[14] P.-H. Wu, «A comparison of methods to assess cell mechanical properties», *Nature methods*, vol. 15, fasc. 7, pp. 491–498, 2018.
[15] S. Cuenot, «Poroelastic and viscoelastic properties of soft materials determined from AFM force relaxation and force-distance curves», *journal of the mechanical behavior of biomedical materials*, vol. 163, 2025, doi: 106865.
[16] D. Ferrera, C. Canale, e R. Marotta, «Lamin B1 overexpression increases nuclear rigidity in autosomal dominant leukodystrophy fibroblasts», *FASEB J*, vol. 28, fasc. 9, pp. 3906–3918, 2014, doi: 10.1096/fj.13-247635.
[17] S. Kerdegari, «Contact-free characterization of nuclear mechanics using correlative Brillouin-Raman Micro-Spectroscopy in living cells», *Acta Biomaterialia*, 2025.
[18] J. T. Cheung e M., «Zhang,7 - Mechanics of the human skin and underlying soft tissues, Woodhead».
[19] R. Kapon, «Permeating the nuclear pore complex», *Nucleus (Austin*, vol. Tex.) vol. 1,6, pp. 475–80, 2010, doi: 10.4161/nucl.1.6.13112.
[20] C.-R. Hsia, D. P. Melters, e Y. Dalal, «The force is strong with this epigenome: chromatin structure and mechanobiology», *Journal of molecular biology*, vol. 435, fasc. 11, p. 168019, 2023.

6

Mechanical Properties of Nanocarriers

6.1 Introduction

Extracellular vesicles (EVs) are a heterogeneous superfamily of lipid bilayer-enclosed nanoparticles released by all cell types and secreted into the extracellular space. They display a wide range of sizes, molecular cargos, and surface markers [1].

These vesicles have fundamental role of EVs as mediators of intercellular communication that today is well established. However, their precise biological functions remain incompletely understood due to their heterogeneity, diverse biogenetic pathways, and the complexity of their interactions in vivo.

Their ability to transport proteins, lipids, and nucleic acids between the parent and the target cell, has placed them at the center of intense scientific investigation [2-3]. Current research is driven by two major motivations. On one hand, EVs play a central role in mediating intercellular communication, influencing mechanisms such as immune modulation, tissue homeostasis, and tumor progression. For this reason, understanding the mechanisms that govern the production and activity of the different EV populations represents an important step toward elucidating fundamental biological processes [4]. On the other hand, their intrinsic biocompatibility, low immunogenicity, and natural homing capabilities have made them promising candidates for therapeutic applications, particularly in drug delivery [5-6].

In recent years, several drug delivery systems based on natural EVs have been developed. However, despite their promise, the clinical translation of these systems remains limited by challenges such as low production yield, labor-intensive purification processes,

heterogeneous populations, and difficulties in achieving consistent and efficient cargo loading [7].

These limitations have stimulated the development of bioinspired EV-mimetics designed to reproduce the natural vesicles functionality while enabling higher production efficiency and improved control over physicochemical properties. To address these challenges, a wide range of nanocarriers has been developed, which can be broadly classified into three main categories (*figure 6-1[22]*):

Natural EVs, which are vesicles directly isolated from cells, either in their native form or produced by genetically engineered cells designed to enhance specific functions such as targeting, cargo loading, or immune evasion. These vesicles retain the complex biochemical composition of their cell of origin, including membrane proteins and lipids that mediate natural homing abilities and biocompatibility.

Hybrid EVs, which are natural EVs that undergo post-isolation modification to improve their therapeutic performance. Such modifications may include the incorporation of drugs, nucleic acids, or imaging agents, as well as surface functionalization with targeting ligands, peptides, or antibodies. Hybrid EVs aim to combine the biological advantages of natural vesicles with the versatility of nanotechnological engineering [8].

EV-inspired liposomes, synthetic lipid-based nanoparticles designed to mimic the structural and functional features of extracellular vesicles. These systems offer high reproducibility, ease of large-scale production, and the possibility to fine-tune membrane composition, size, and mechanical properties. Although they may lack some of the biological complexity of natural EVs, EV-inspired liposomes can be engineered to approximate EV-like behaviour while offering improved stability and loading efficiency [9].

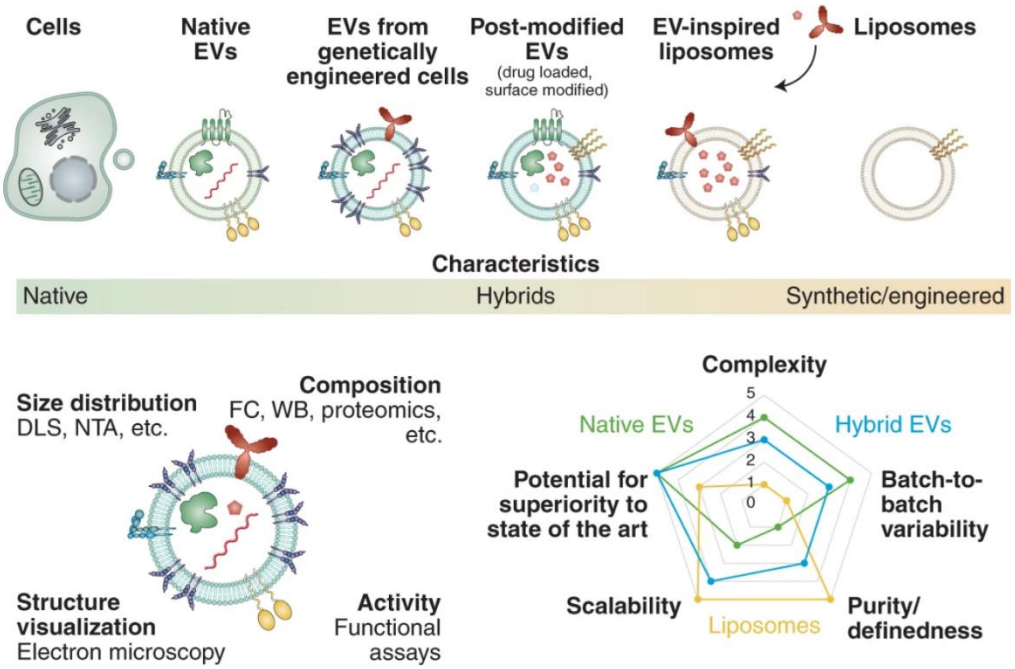

Figure 6-1: Illustration of the different types of vesicles used for drug delivery systems from the more nbiogenic to the more syntetic.

A strategy proposed in recent years to overcome the limitations of natural EVs and fully synthetic nanocarriers involves the exploitation of cell membrane–based engineering approaches [10]. These methods include the isolation of cell membranes to fabricate cell-mimicking vesicles or to coat synthetic nanoparticles, as well as the development of hybrid vesicles generated by fusing artificial liposomes with naturally derived EVs. Within the classification introduced above, these systems occupy an intermediate position between natural EVs, hybrid EVs, and EV-inspired liposomes.

Specifically, cell membrane–derived vesicles (CMVs) are produced by isolating the plasma membrane from a chosen cell type and restructuring it into nanoscale vesicles. Because they preserve the lipid composition and membrane protein repertoire of the parent cell, CMVs maintain essential biological features such as immunomodulatory behaviour, natural targeting ligands, and homing abilities [11]. At the same time, their production yields are significantly higher and more controllable than those of natural EVs, making them attractive for drug delivery applications.

Mechanical properties of EVs and nanocarrier systems

Mechanical properties are a crucial aspect for both fundamental understanding and therapeutic exploitation of EVs. Throughout their biological life cycle, nanoscale vesicles are exposed to a variety of mechanical forces, arising from extracellular transport, cellular uptake and release, membrane deformations, and interactions with biological interfaces.

Increasing evidence suggests that mechanical behaviour may influence vesicle stability, trafficking efficiency, and the internalization process into the target cells, thereby contributing to the regulation of intercellular communication [12, 13].

However, accurate and reproducible measurement of the mechanical properties of EVs remains challenging. Their nanometric dimensions, combined with the relative softness, demand high-resolution techniques and robust analytical protocols that are not yet standardized. As a result, the field still lacks universally accepted methodologies for determining parameters such as elastic modulus, membrane stiffness and bending modulus.

Several experimental approaches are employed to probe the mechanical properties of lipid nanovesicles, including AFM [14], microfluidic deformability cytometry [15], and electrodeformation [16]. However, reported results often show substantial variability, largely due to differences in the measurement techniques, experimental conditions, and vesicle preparation protocols.

The AFM-based investigation of EVs allows obtaining information about their morphology and mechanics with high spatial resolution (a few tens of nanometers in the x–y plane and on the order of one nanometer in the z direction) and a force resolution on the order of 10^2 pN. In particular, recent methodological advances now allow simultaneous acquisition of morphological and mechanical maps through quantitative imaging (QI) mode, where dense arrays of force–distance curves enable reconstruction of nanoscale multispectral maps, as described in the methodological chapter.

Thin Shell Theory of Indentation

The Thin Shell Theory (TST) provides a mechanical model for describing the indentation of extracellular vesicles (EVs) by an AFM probe [17]. In this framework, an EV is approximated as a hollow, thin-walled spherical shell of thickness *t* and characterized by a finite shear modulus. Unlike models that treat the vesicle as a homogeneous solid, the

TST explicitly accounts for the mechanical contribution of the membrane as an elastic shell, neglecting the presence of internal cargo.

According to this theory, the Young and the Bending modulus of the shell are described by a geometry-dependent expression:

$$E = \frac{kR_c\sqrt{3(1-\nu^2)}}{4\epsilon^2}, \qquad K_c = \frac{E\epsilon^3}{12(1-\nu^2)}$$

in which *E* denotes the Young's modulus of the shell material, *κ* is a proportionality factor determined by the specific shell geometry, R_c is the radius of curvature of the vesicle and ε is the thickness of the shell (*figure 6-2*). A key prediction of the TST is that, for indentation depths smaller than the shell thickness, the force response is expected to be linear. For EVs, this regime corresponds to indentation depths of few nanometers beyond the contact point between the probe and the vesicle surface.

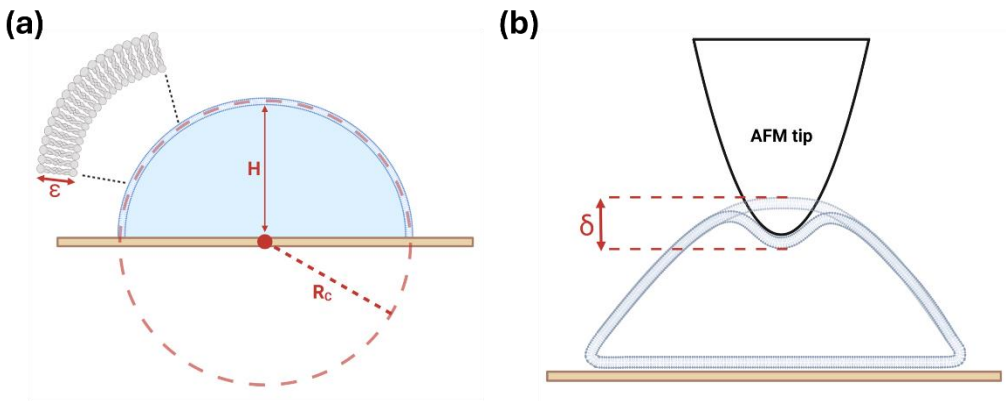

Figure 6-2: (a) Schematic representation of the theoretical hemispherical shell, characterized by its radius of curvature, thickness, and height. (b) Representation of the AFM tip indenting the vesicle.

Infact, as the indentation increases, the assumptions of the thin-shell regime progressively lose validity. When the deformation exceeds the characteristic thickness of the membrane, the mechanical response becomes increasingly dominated by the bulk-like behavior of the vesicle, and the superlinear force–indentation trend predicted by the Hertz model starts to prevail [18]. This transition reflects the progressive involvement of bending, stretching, and localized deformation modes not captured by the thin-shell approximation.

Overall, the Thin Shell Theory provides an essential conceptual and quantitative framework for interpreting AFM indentation experiments on EVs, especially in the initial,

small-deformation regime where membrane elasticity primarily governs the mechanical response.

6.2 Mechanical Characterization of Nanocarriers

In this context, the project that is going to be exposed focuses on the mechanical characterization of different vesicle systems developed within a collaborative project involving the Pharmacology and Medical Departments of the University of Genoa, leaded respectively by Professor Gabriele Caviglioli and Professor Tullio Florio.

The overarching objective of the project is the design of an innovative nanocarrier platform for Boron Neutron Capture Therapy (BNCT), a targeted radiotherapeutic strategy based on the selective internalization of B^{10}-containing compounds in cancer cells, followed by neutron irradiation leading to highly localized cytotoxic reactions. To address the limitations of natural EVs as delivery vehicles, we developed cell membrane–derived vesicles (CMVs) obtained from patient-derived glioblastoma multiforme (GBM) stem-like cells (*figure 6-3*).

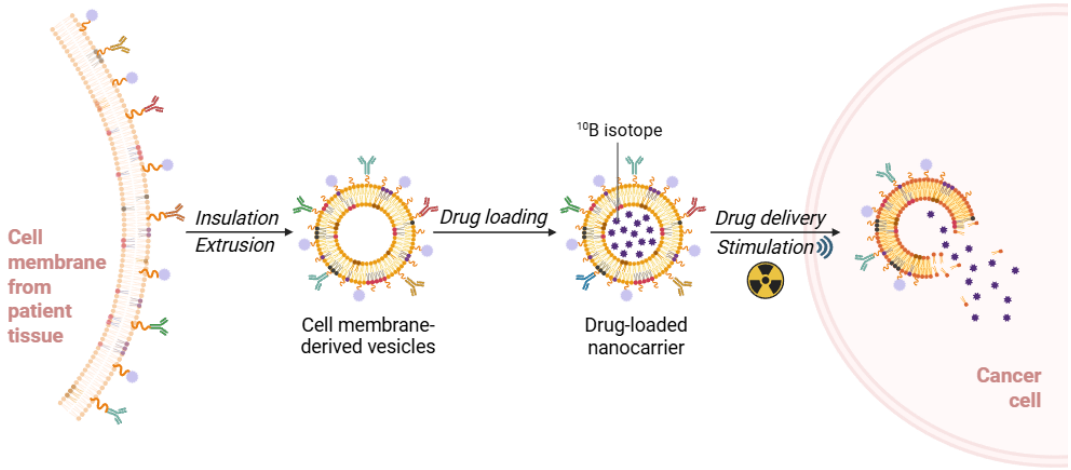

Figure 6-3: Schematic representation of the project, illustrating the development of CMVs, their loading with the 10-B isotope, and subsequent internalization into cancer cells, with the ultimate goal of eliminating the cancer cells via BNCT.

Moreover, CMV preparation methods make it possible to engineer the vesicle lipid composition by incorporating synthetic lipid species into the biogenic lipid mixture, thus creating hybrid biomimetic nanocarriers. These hybrid vesicles are designed to retain the intrinsic homing ability associated with their cellular origin, while offering improved yield, reproducibility, and loading capacity compared with conventional EVs.

The mechanical characterization of CMVs has a twofold purpose: on the one hand, to investigate the mechanics of biogenic vesicles and relate them to their internalization efficiency and to the mechanical properties of other lipid nanoparticles; on the other hand, to tune the mechanics of hybrid vesicles to achieve optimal cellular uptake while increasing production yield (*figure 6-4 [21]*).

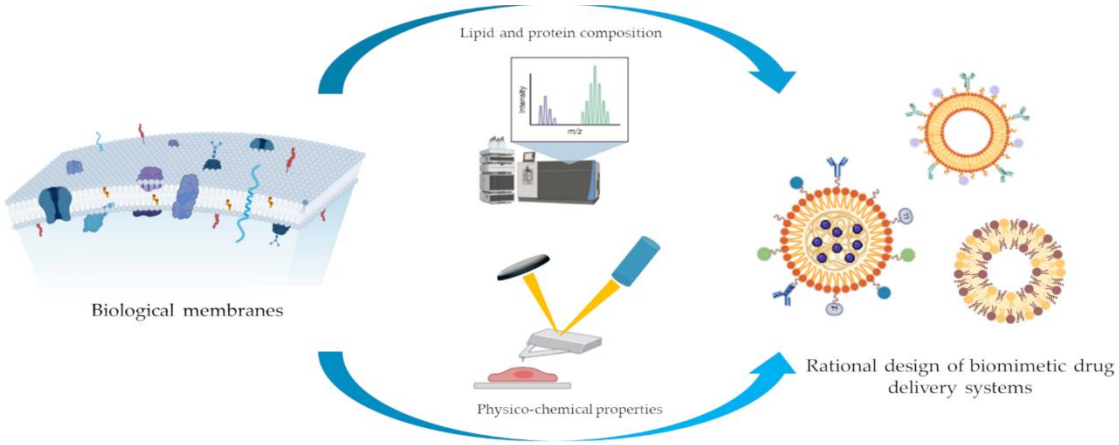

Figure 6-4: Schematic representation of the concept of tuning the physicochemical properties of the nanocarriers, following biophysical characterization, in order to optimize their drug delivery performance.

6.3 Materials and Methods

Cell Culture

Human glioblastoma cultures (GBM1 and GBM2) were derived from postsurgical specimens obtained at IRCCS Ospedale Policlinico San Martino (Genoa). Cells were maintained in serum-free 1:1 DMEM-F12/Neurobasal™ medium supplemented with B27™, 2 mM L-glutamine, 1% penicillin–streptomycin, 15 µg/mL insulin, and 2 µg/mL heparin. Human bFGF and EGF (20 ng/mL each) were added to enrich the stem-like population and preserve their biological features in vitro. Under these conditions, cells formed floating tumor spheres within two weeks; however, for reproducible experimental handling they were expanded as monolayers on growth factor-reduced Matrigel™, which supports the maintenance of stem-cell markers, spherogenic capacity, and tumorigenic potential. Tumor-initiating ability had been previously validated through orthotopic xenografts in immunodeficient mice. The human glial hybrid cell line M03.13 (Tebu-Bio), which exhibits characteristics of primary oligodendrocytes, was cultured in high-glucose

DMEM with 10% FBS, 1% penicillin/streptomycin, and 1% glutamine. Differentiation was induced using 100 nM phorbol 12-myristate 13-acetate (PMA) in 1% FBS medium for five days prior to CMV treatment.

Preparation of Liposomes

To prepare liposomes of composition of DSPC, cholesterol and DSPE-PEG 52:45:3 mol% and with an average diameter of 120 nm, the individual lipid stock solutions were mixed in a glass cuvette in proportions chosen to obtain the desired lipid composition. This lipid composition is commonly employed for vesicles designed for drug delivery applications. In fact, it closely resembles the formulation used for Doxil liposomes [20]. The solvent was then evaporated, first under a gentle nitrogen stream to accelerate the process and subsequently under vacuum for twelve hours to remove any residual traces of solvent. After this step, a homogeneous lipid film adhered to the walls of the cuvette.
The film was rehydrated in PBS buffer. After hydration, the suspension was incubated for 15 minutes, during which the lipids self-assembled into large multilamellar aggregates ranging in size from hundreds of nanometers to several micrometers. Then, multilamellar aggregates were extruded using a filter of 100 nm of diameter.

Preparation of CMVs and Hybrid Vesicles

Human glioblastoma cells (GBM1), cultured on Matrigel™ in 75 cm^2 flasks, were detached using TryPLE (Thermo Fisher Scientific). A total of 5×10^8 cells were homogenized on ice in pH 7.4 homogenization buffer using a Dounce homogenizer (100 strokes), disrupting the cells while preserving intact nuclei.
The resulting homogenate underwent differential centrifugation in 1.5 mL Beckman tubes at 4 °C: two consecutive spins at 800 g for 5 min, followed by centrifugation of the collected supernatant at 10,000 g for 20 min. The final supernatant was centrifuged at 25,000 g for 20 min; the pellet was then washed twice with homogenization buffer and twice with 0.9% NaCl, each time centrifuging at 25,000 g for 20 min.
The resulting membrane pellet was resuspended in 0.8 mL of Milli-Q water or PBS (pH 7.4) to obtain multilamellar CMVs, which were subsequently extruded through polycarbonate membranes of decreasing pore size (400, 200, and 100 nm; 20 passes

each) using an Avestin LiposoFast Basic extruder maintained at 37 °C and 4 bar (*figure 6-5*).

Hybrid vesicles were generated by mixing the CMV homogenate with the lipid formulation used for liposome preparation at a 1:1 ratio.

For fluorescence labeling, selected CMV and liposome batches were incubated with CM-DiI (2 pmol/µL in ethanol). The dye solution was added directly to the membrane pellet, which was vortexed and sonicated until fully suspended. Ethanol was then evaporated under a gentle nitrogen stream at room temperature, after which the pellet was resuspended in Milli-Q water or PBS (pH 7.4) and extruded as above to obtain red fluorescent CMVs.

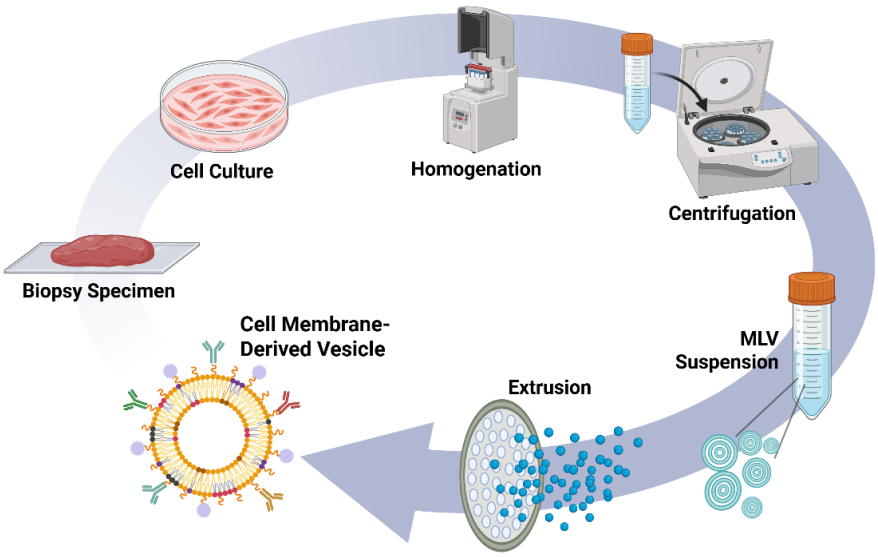

Figure 6-5: Schematic rappresentation of the steps of prodaction of CMVs.

Internalization Experiments

A Stellaris8 Falcon TauSTED (Leica Microsystems), operating as confocal microscope, was used for fluorescence measurements. The desired excitation wavelengths were chosen using a supercontinuum white light laser (λ_{ex} = 488 nm for CellMask™ and Alexa Fluor 488, and λ_{ex} = 561 nm for CM-DiI), setting a notch filter at 488 nm and 561 nm, respectively. Two HyDS detectors (Leica Microsystems) were used to measure CellMask™/Alexa Fluor 488 and CM-DiI fluorescence emissions, in the 500–540 nm and 570–720 nm ranges, respectively, observing the samples through a plan-apochromatic oil immersion objective 100X/1.40 NA.

For CMV internalization measurements, Z-stacks of images (1024 × 1024 × 16 bit) were obtained using a Z-step size of 0.7 µm and a scan speed of 600 Hz. The acquired Z-stacks were analyzed using Leica Application Suite X (LAS X) software, considering the maximal Z-projection. The time of measurement was kept below 2 h for each sample.

AFM Sample Preparation

The vesicle suspension was deposited onto a substrate that consists of a circular coverslip with a diameter of 35 mm on which a solution of poly-L-lysine (10 µg/mL) was deposited. The surface of the coverslip was covered with the solution and then incubated for 20 minutes. Subsequently, the solution was aspirated, and the sample was left to dry for 1 hour.

30 µL of CMV suspension were deposited onto the substrate. The sample was incubated for 5 minutes. Afterwards, 70 µL of PBS were added.

The same protocol was followed for the AFM measurement on CMVs, Liposomes and Hybrid Vesicles.

AFM-based Mechanical Characterization

Morphological and mechanical maps of CMVs were acquired using a JPK NanoWizard IV atomic force microscope (Bruker) operated in Quantitative Imaging (QI) mode. A Bruker DNP-10 cantilever with a nominal spring constant of 0.24 N/m was used. The conical tip had a nominal radius of 20 nm and a vertical length of 120 µm.

QI maps were collected at a resolution of 128 × 128 pixels with a scan size between 400 and 600 nm.

Data were processed using the JPK analysis software to generate stiffness maps and extract morphological parameters. In particular, vesicle curvature radius was determined by generating cross-section profiles and fitting them with a circular arc.

6.4 Results

Internalization Experiments

The CMV targeting ability was evaluated through internalization experiments performed on different types of cell cultures. Specifically, three cultures were tested: CMV–glioblastoma parent cells, glioblastoma cells derived from a different patient (to assess patient-specificity of CMV targeting), and oligodendrocytes. In addition, glioblastoma

cells were used to assess the internalization of artificial liposomes. Each combination of vesicle and cell type was evaluated at two incubation times, 15 and 30 minutes, to assess not only the extent but also the dynamics of internalization.

The qualitative outcomes of these experiments are reported in the *figure 6-6*.

CMVs exhibit a high level of internalization in glioblastoma cells, with no significant difference observed between parent and non-parent cell lines, indicating that their uptake is not strongly influenced by patient specificity. In contrast, the internalization of CMVs in oligodendrocytes is negligible, confirming a marked preference for tumor cells over healthy neural cells.

No significant differences were observed in the internalization rate when comparing the two incubation times, indicating that the uptake process reaches comparable levels within both time windows. However, an increase in the CMV fluorescence signal is evident at the longer incubation time.

Consistently, the internalization of artificial liposomes in glioblastoma cells is also very low, further highlighting the superior targeting and uptake efficiency of CMVs compared to synthetic nanocarriers.

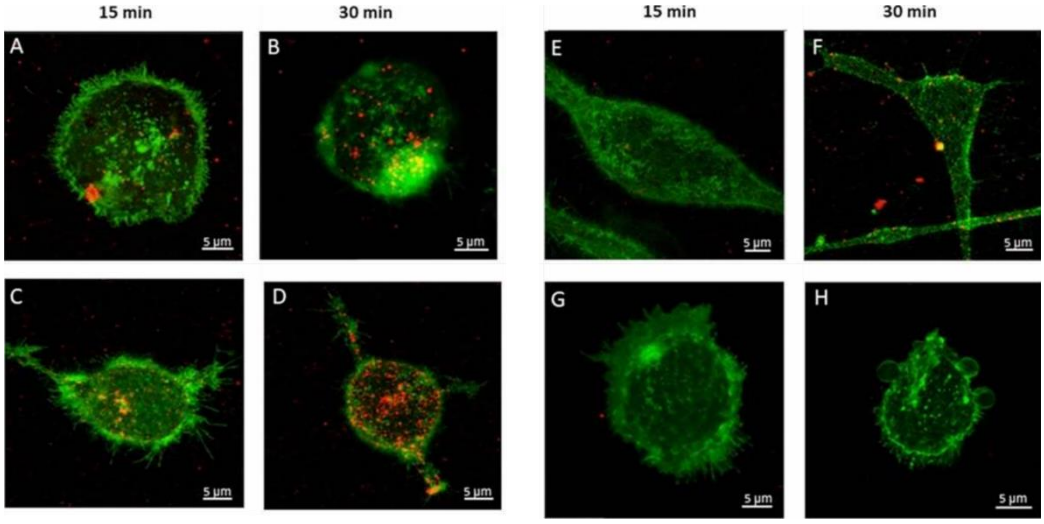

Figure 6-6: Confocal images of the internalization experiments showing: (A–B) CMVs in parent glioblastoma cells, (C–D) CMVs in glioblastoma cells from a different patient, (E–F) CMVs in oligodendrocytes, and (G–H) liposomes in glioblastoma cells.

Morphological Analysis of the lipid Vesicles

AFM analysis of individual vesicles was performed on 20 samples for each type: CMVs, Liposomes, and Hybrid Vesicles.

The vesicle morphology was examined using the QI map, specifically considering the cross-section passing through the apical region of each vesicle. This approach allowed a detailed assessment of vesicle shape and structural features at their most representative plane (*figure 6-7*).

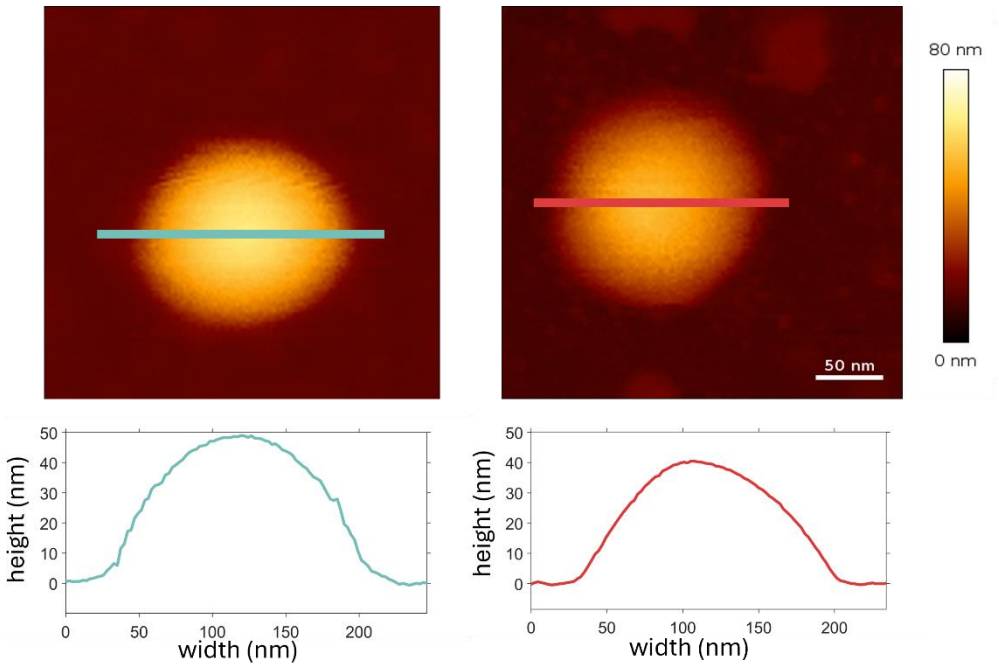

Figure 6-7: Height maps acquired with AFM QI mode for (a) a liposome and (b) a CMV, along with their respective cross-sections. The morphology of the two vesicles appears quite similar in terms of height and overall geometry.

It is important to note that the morphology observed in the AFM experiments results from the interaction between the vesicle and the substrate, in this case, glass coated with poly-lysine. Therefore, what we measure reflects the adsorption geometry of the vesicle, which depends not only on its intrinsic shape and mechanical properties but also on its affinity for the substrate. Achieving comparable adsorption geometries is a critical requirement for the meaningful comparison of different vesicle samples.

To quantitatively characterize the adsorption geometry, the ratio between the vesicle height and the radius of curvature was used as a parameter. A semi-spherical vesicle corresponds to a value of 1 for this parameter, while values lower than 1 indicate a flatter geometry.

This metric provides a standardized way to compare the extent of flattening or spreading of different vesicle types upon interaction with the substrate.

The geometry of absorption data have been reported in *figure 6-8*.

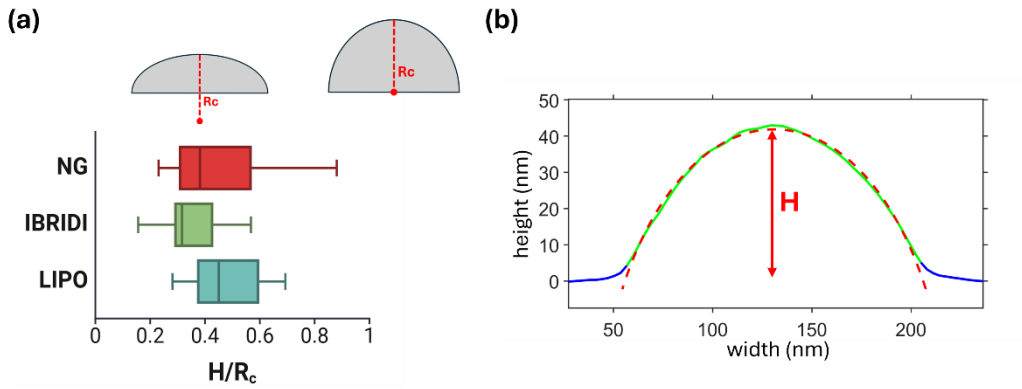

Figure 6-8: (a) Boxplot showing the distribution of data related to the absorption geometry. A value of 1 corresponds to a hemispherical geometry, while values less than 1 indicate a flatter geometry. The three distributions do not show significant differences according to ANOVA analysis. (b) Example of a vesicle cross-section fitted with a circular arc.

Mechanical Characterization of Vesicles

The morphological data extracted from the QI height maps were used to apply the TST model described above. Force–distance curves were acquired under the constraint that indentation remained below the vesicle membrane thickness, assumed to be 5 nm based on literature data and simulations [19] for lipid vesicles of similar composition. An example of force distance curve acquired on a vesicle is reported in *figure* 6-9.

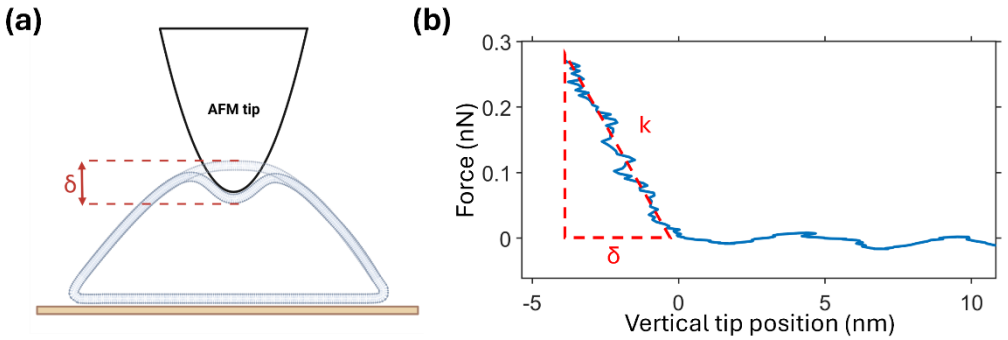

Figure 6-9: (a) Schematic representation of a vesicle deposited on a rigid substrate and indented by an AFM tip. (b) Force–distance curve acquired on a vesicle, showing an indentation constrained to less than 5 nm. By definition, the stiffness $k$corresponds to the slope of the curve.

The analysis of the stiffness maps of CMVs and liposomes, including cross-sectional profiles, revealed a radial stiffness gradient (*figure 6-10*). In liposomes, stiffness remained constant in the apical region and decreased sharply toward the periphery. CMVs displayed a softer radial profile, although a decrease toward the periphery was still observable.

A possible interpretation of this phenomenon is related to the interaction between the AFM tip and the lipid vesicle (*figure 6-11*).

In the apical region of the vesicle, the tip–sample interaction is approximately orthogonal, allowing accurate measurement of indentation and stiffness. Toward the periphery, however, the tip tends to slide along the curved surface, producing artifacts in the measured indentation and stiffness values. This effect is more pronounced for stiff, less deformable samples, where the tip sliding is maximized. In contrast, for softer vesicles,membrane deformation reduces the impact of this artifact, resulting in more reliable measurements at the edges.

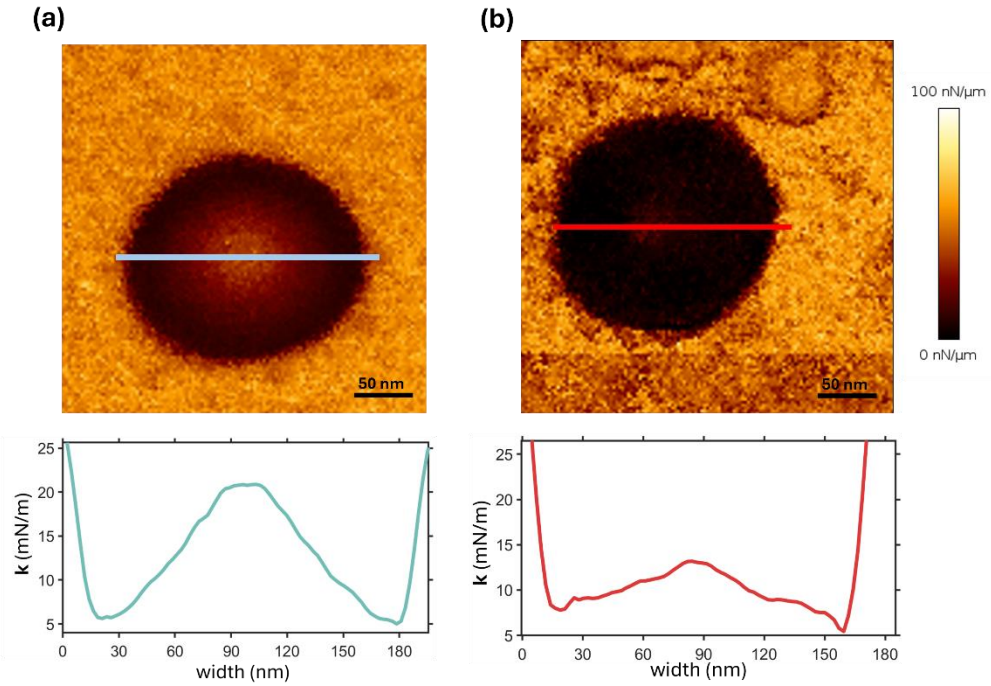

Figure 6-10: Stiffness maps acquired for (a) liposomes, showing a pronounced stiffness gradient, and (b) CMVs, where the stiffness gradient is less pronounced.

To avoid this artefact, the TST was applied by considering only the force–distance curves acquired within a 50 nm radius from the vesicle centre, where the tip–vesicle interaction is orthogonal.

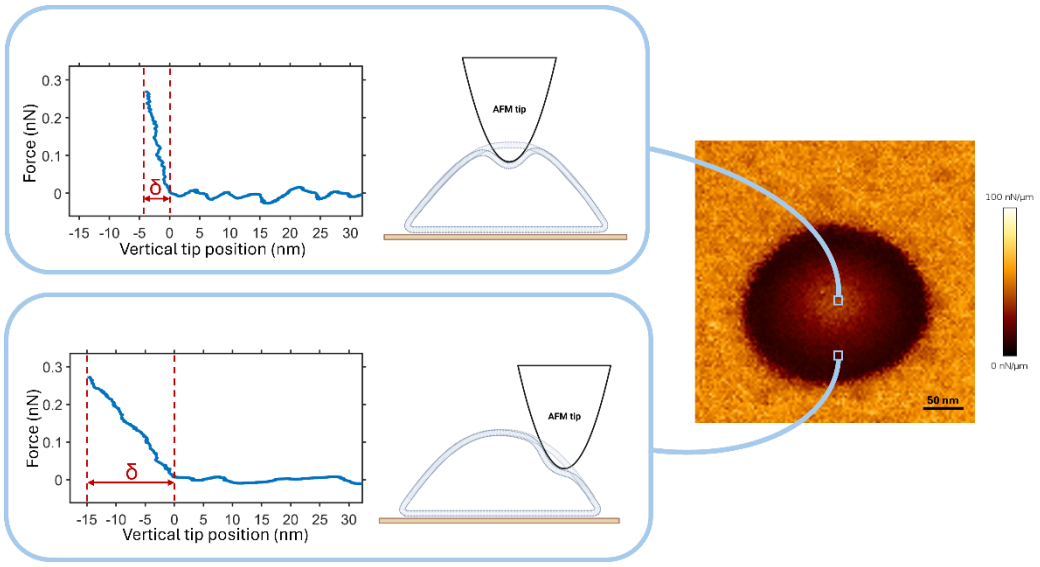

Figure 6-11: Schematic representation of the indentation variations observed in two force–distance curves acquired from different regions of the stiffness map: the apical region and the peripheral region.

Overall, these results provide a first qualitative understanding of the distinct mechanical features exhibited by the different vesicle types and align well with the values of Young's modulus and bending energy obtained through the TST model.

The data distributions are shown in the boxplot in *figure 6-12*. CMVs prove to be significantly softer than liposomes. For CMVs, the population-average values of Young's modulus and bending energy are (32 ± 9) MPa and (108 ± 30) k_BT (mean ± SD), respectively.In contrast, liposomes exhibit higher stiffness, with an average Young's modulus of (79 ± 31) MPa and a bending modulus of (265 ± 83) k_BT.

The hybrid vesicles show an intermediate behaviour, consistent with their composite nature—an integration of both CMV and liposomal components. Their mean Young's modulus is (46 ± 15) MPa, and the corresponding bending modulus is (153 ± 48) k_BT.

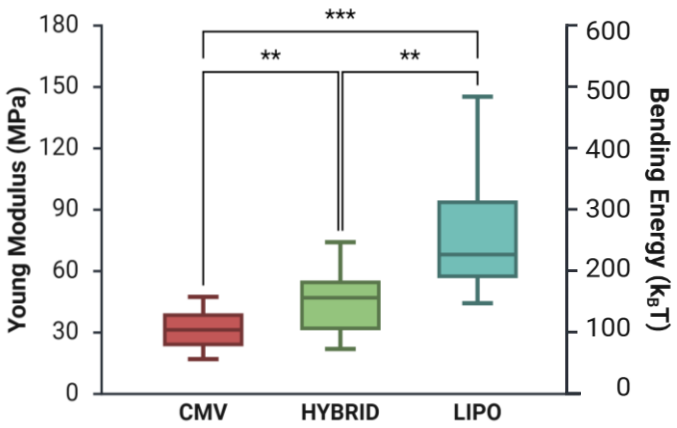

Figure 6-12: Boxplot of Young Modulus and Bending Modulus data distribution. Welch's one-way ANOVA was performed to assess statistical significance between the distributions.

6.5 Conclusions

The internalization experiments assessed the targeting ability of three different nanocarrier systems, confirming the strong potential of CMVs as an effective drug delivery technology. As expected, CMVs selectively internalize into the same cell type as the parent cells from which they originate, while not being limited to recognizing cells from the same individual donor. This highlights their intrinsic biological selectivity together with a broader applicability in heterogeneous patient contexts.

The results obtained through the AFM-based protocol and the application of the TST model further enabled the characterization of the distinct mechanical features of the three lipid vesicle types, providing quantitative and directly comparable measurements. This mechanical profiling offers a deeper understanding of how vesicle composition influences structural rigidity and deformability, parameters that are crucial for cellular uptake and biodistribution.

The ability to obtain mechanical feedback on the produced vesicles represents a valuable tool for hybrid engineering. By altering the synthetic lipid species included in the hybrid formulation and adjusting the ratio between biogenic and synthetic components, it becomes possible to fine-tune the mechanical properties of the vesicles while preserving their inherent homing capability.

The next steps of the project will involve testing the targeting ability of hybrids with varying synthetic compositions to identify the formulations that best preserve or enhance CMV-like selectivity. In parallel, the ^{10}B-loading strategy and the full BNCT protocol will be

developed and optimized using both CMVs and hybrid vesicles, aiming to establish a robust platform for future therapeutic applications.

6.6 Bibliography

[1] Serva A. *et al.* "Extracellular Vesicles as Cancer Biomarkers and Drug Delivery Strategies in Clinical Settings: Advances, Perspectives, and Challenges", *Clinics*, 2025

[2] Chang, W. H., Cerione, R. A. & Antonyak, M. A. Extracellular vesicles and their roles in cancer progression. *Methods Mol. Biol.* **2174**, 143–170 (2021).

[3] Xie, F. et al. Extracellular vesicles in cancer immune microenvironment and cancer immunotherapy. *Adv. Sci.* **6**, 1901779 (2019)

[4] Maacha, Selma et al. "Extracellular vesicles-mediated intercellular communication: roles in the tumor microenvironment and anti-cancer drug resistance." *Molecular cancer* vol. 18,1 55. 30 Mar. 2019, doi:10.1186/s12943-019-0965-7

[5] Mentkowski, Kyle I., et al. "Therapeutic potential of engineered extracellular vesicles." *The AAPS journal* 20.3 (2018): 50.

[6] Hanjani, Niloofar Asadi, et al. "Emerging role of exosomes as biomarkers in cancer treatment and diagnosis." *Critical reviews in oncology/hematology* 169 (2022): 103565.

[7] van de Schepop L, Stiemsma YL, Wichers LX, et al. Bottom-Up Synthesis and Purification of Extracellular Vesicle Mimetics. *J Extracell Vesicles*. 2025;14(11):e70190. doi:10.1002/jev2.70190

[8] Ducrot, Coline, et al. "Hybrid extracellular vesicles for drug delivery." *Cancer Letters* 558 (2023): 216107.

[9] López, R., Ben El Khyat, C., Chen, Y. *et al.* A synthetic model of bioinspired liposomes to study cancer-cell derived extracellular vesicles and their uptake by recipient cells. *Sci Rep* **15**, 8430 (2025). https://doi.org/10.1038/s41598-025-91873-5

[10] Toledano Furman, Naama E., et al. "Reconstructed stem cell nanoghosts: a natural tumor targeting platform." *Nano letters* 13.7 (2013): 3248-3255.

[11] Balboni, A., Ailuno, G., Baldassari, S. *et al.* Human glioblastoma-derived cell membrane nanovesicles: a novel, cell-specific strategy for boron neutron capture therapy of brain tumors. *Sci Rep* **14**, 19225 (2024)

[12] Lenzini S, Bargi R, Chung G, Shin JW. Matrix mechanics and water permeation regulate extracellular vesicle transport. *Nat Nanotechnol*. 2020;15(3):217-223. doi:10.1038/s41565-020-0636-2

[13] Vorselen D, MacKintosh FC, Roos WH, Wuite GJ. Competition between Bending and Internal Pressure Governs the Mechanics of Fluid Nanovesicles. *ACS Nano*. 2017;11(3):2628-2636. doi:10.1021/acsnano.6b07302

[14] Vorselen, Daan, et al. "Mechanical characterization of liposomes and extracellular vesicles, a protocol." *Frontiers in molecular biosciences* 7 (2020): 139

[15] Hu, Wei-Fan, et al. "Vesicle electrohydrodynamic simulations by coupling immersed boundary and immersed interface method." *Journal of Computational Physics* 317 (2016): 66-81.

[16] Morshed, Adnan, et al. "Electrodeformation of vesicles suspended in a liquid medium." *Physical review fluids* 3.10 (2018): 103702.

[17] Lytra, A., et al. "Modeling atomic force microscopy and shell mechanical properties estimation of coated microbubbles." *Soft Matter* 16.19 (2020): 4661-4681.

[18] A. Calò, D. Reguera, G. Oncins, M.-A. Persuy, G. Sanz, S. Lobasso, A. Corcelli, E. Pajot-Augy, G. Gomila, *Nanoscale* 2014, **6**, 2275.

[19] Carretta, Annalisa, et al. "The supramolecular processing of liposomal doxorubicin hinders its therapeutic efficacy in cells." *Molecular Therapy Oncology* 32.3 (2024).

[20] Drabik, Dominik, et al. "Mechanical properties determination of DMPC, DPPC, DSPC, and HSPC solid-ordered bilayers." *Langmuir* 36.14 (2020): 3826-3835.

[21] Donghia, Daniela, et al. "Insights on Natural Membrane Characterization for the Rational Design of Biomimetic Drug Delivery Systems." *Pharmaceutics* 17.7 (2025): 841.

[22] Herrmann, Inge Katrin, Matthew John Andrew Wood, and Gregor Fuhrmann. "Extracellular vesicles as a next-generation drug delivery platform." *Nature nanotechnology* 16.7 (2021): 748-759.

General Conclusions

This thesis develops and implements advanced **Atomic Force Microscopy (AFM)** methodologies that extend far beyond its conventional use as a high-resolution characterization tool. A central innovative aspect of this work lies in repositioning AFM as a multifunctional platform for quantitative rheology and as a core component of correlative experimental systems for mechanotransduction studies. Through this approach, AFM is established as a versatile and integrative technology for uncovering novel mechanobiological insights into neurodegenerative diseases.

The first part of the thesis addresses amyloidosis from a mechanical and energetic perspective. An original application of AFM-based Force Clamp Spectroscopy was developed to directly quantify the mechanical destabilization induced by pathological α-synuclein oligomers on biomimetic artificial membranes. The results reveal a clear concentration-dependent effect, with an increase in lipid interaction energy at low oligomer concentrations, while a disruptive, detergent-like behavior becomes predominant at higher concentrations. These findings provide a mechanistic and quantitative framework for interpreting early membrane toxicity in amyloid-related disorders.

A further major innovation is the development of a correlative AFM–calcium imaging platform designed to probe the mechanosensitive channel Piezo1 under controlled mechanical stimulation in the presence of α-synuclein and Aβ oligomers. This integrated setup allows direct coupling between nanoscale mechanical perturbation and real-time functional calcium readout. Interestingly, the results do not reveal significant alterations in channel activity, suggesting the existence of compensatory regulatory mechanisms that preserve plasma membrane mechanical stability in living cells. This finding opens new perspectives on the interplay between amyloid toxicity and cellular mechanotransduction.

The second part of the thesis applies an integrated mechanical framework to the study of a genetic laminopathy, Autosomal Dominant Leukodystrophy. The innovative contribution here lies in combining a poroelastic mechanical model with AFM-based rheological measurements and Brillouin spectroscopy, enabling multi-compartment mechanical characterization of both cytoplasmic and nuclear domains. The results reveal a predominant contribution of the cytoplasm to the overall mechanical response, demonstrating that nuclear defects can propagate mechanically beyond the nucleus and induce cytoskeletal reorganization. This work advances a systems-level view of cellular mechanics in laminopathies.

Finally, the thesis extends AFM applications into nanomedicine by establishing a protocol for the controlled tuning of nanocarrier mechanical properties for drug delivery applications. By correlating vesicle mechanics with targeting efficiency and cellular internalization, this work introduces mechanical properties as an active design parameter for optimizing therapeutic performance.

Overall, this thesis demonstrates how AFM can be reconceptualized as a cross-disciplinary platform bridging mechanics, cellular function, and pathology. The methodological innovations and integrative experimental strategies developed here provide new conceptual and technical tools for investigating neurodegenerative diseases and for engineering mechanically optimized therapeutic systems.